博士論文

Investigation of solution process of molybdenum disulfide for thin film transistor applications

金　胄男

指導教員　　徳光 永輔

北陸先端科学技術大学院大学

マテリアルサイエンス研究科

平成 29 年 3 月

Abstract

The chemical solution process of MoS_2 on high–k oxide films has been systematically investigated. The source solution used in this work is made of $(NH_4)_2MoS_4$ powder dissolved in N-methyl-2-pyrrolidone due to its solution stability and uniform wettability. The source solution was spin-coated on various kinds of dielectric oxide films for thin film transistor (TFT) applications and it is shown that the coating properties strongly depend on the kind of dielectric material using analysis of surface energy. Moreover, among many kinds of high-k dielectric materials for MoS_2, the ZrO_2 system is selected because of its thermal stability at 1000 ºC in sulfur atmosphere and chemical stability with MoS_2. To enhance a dielectric constant of ZrO_2, Nb-doped ZrO_2 were fabricated by chemical solution process. The 30 % Nb-doped ZrO_2 (NZO) annealed at 800 ºC and 1000 ºC in air atmosphere for 20 min, showed dielectric constant of 40 and 25, respectively. It is demonstrated that the MoS_2 film can be grown on NZO by the solution process with a two-step annealing process, where the first annealing is performed at 450 ºC in H_2/Ar (5:95) atmosphere for 20 min and the second annealing at 1000 ºC in Ar atmosphere with sulfur vapor for 20 min. In addition, conformal growth of a MoS_2 layered structure on the curved surface of the oxide film is confirmed by transmission electron microscope observations. A further conclusion is that the thickness of MoS_2 can be controlled by the concentration of a source solution and that two-layer MoS_2 is obtained when the concentration of source solution is 0.00625 mol/kg. The measured Hall mobility of the solution-derived MoS_2 film, annealed at 1000 ºC is approximately 25 cm^2/Vs. After research about MoS_2 film formation on high-k oxide film, the thin film transistor (TFT) was fabricated using MoS_2. The n-channel transistor operation was confirmed with an on/off ratio of $5x10^4$ and a filed effect mobility of 0.71 cm^2/Vs.

Keywords: solution process, MoS_2, high-k, thin film transistor

List of figures

Figure 1-1. Gate length scaling path (a) and (b) the representative illustration of short channel effect and punch through 10

Figure 1-2. Representative 2D materials crystal structure of (a) graphene, (b)boron nitride, (c) molybdenum disulfide and (d) black bone.....11

Figure 1-3. (a)The lattice structure of graphene (b) band structure. Enlargement of the band structure showing the Dirac cone.....12

Figure 1-4. 2H structure of MoS_2 show the two layers per unit hexagonal structure.....15

Figure 1-5. Calculated band structure of (a) monolayer, (b) bilayer, (c) hexalayer (d) bulk for MoS_2. 16

Figure 2-1. Illustration of the spin-coating process. 25

Figure 2-2 Schematic of GI-XRD.....27

Figure 2-3 Comparison of XRD data measured by (a)GI-XRD (b)normal θ-2θ for CdSeS. ..28

Figure 2-4. Vibration motion for the four first order Raman-active (E_{2g}^2, E_{1g}, E_{2g}^1 and A_{1g}) and the two dipolmoment-active (E_{1u}^1 and A_{2u}^1 modes). 30

Figure 2-5. Picture of Raman scattering experiment of T64000.....30

Figure 2-6. Schematic for the generation of energy difference by the photoemission. 32

Figure 2-7. Schematic of the Kratos Axis Ultra XPS system. 33

Figure 2-8. Schematic diagram of AFM 34

Figure 2-9. Force curve of AFM 35

Figure 2-10. TEM vs SEM electron optics schematics.....37

Figure 2-11. Contact angle of a liquid on a surface. 38

Figure 2-12. Surface energy measurement system. 40

Figure 2-13.Schemtic diagram capillary type TG/DTA system.....41

Figure 2-14. Picture of EXSTAR6000, Tg/DTA system.....42

Figure 3-1. Periodic table indicates what the metal oxide has possibility to be used as a gate

insulator.....45

Figure 3-2. Crystalline structures of ZrO_2 in O-Zr phase diagram at (a) room temperature (rt) for monoclinic, (b) high temperature for tetragonal (ht1) and (c) high temperature for cubic. 46

Figure 3-3. Diagram of (a) solution produce and (b) annealing process for NZO film.....48

Figure 3-4. (a) TEM cross section, EDS image of (b) Nb atom, and (c) Zr atom for NZO film fabricated by sol-gel technique on Si substrate with an annealing temperature of 800 ºC.....50

Figure 3-5. EDS spectra revealing the % compositions of Nb and Zr elements. 51

Figure 3-6. GI-XRD spectra of Nb 0 ~ 50 mol% doped ZrO_2, annealed at 800 ºC.....52

Figure 3-7. (a) Capacitance-voltage (C-V) curves of MIS structures with pure ZrO_2 and Nb (30%) doped ZrO_2 annealed at 800 °C and (b) accumulation capacitance of the NZO MIS structures as a function of Nb doping density.....54

Figure 3-8. AFM image of Nb 30 mol% ZrO_2 film. 55

Figure 3-9 AFM images of NZO-30 annealed at 1000 °C for (a) 5 min, (b) 15 min, (c) 30 min and (d) one hour. 56

Figure 3-10. XPS spectra for (a) Nb 3d, (b) Zr 3d, (c) O 1s of NZO-30 and (d) O 1s of ZrO_2. 59

Figure 3-11. GI-XRD for NZO with variation temperature from 500 ~ 1000 °C. 60

Figure 3-12. (a) Annealing temperature dependence of C-V curves for Nb 30 mol% ZrO_2 film and (b) accumulation capacitance of the MIS structures with pure ZrO_2 and Nb 30 mol% ZrO_2 films. 62

Figure 3-13. The leakage current density of NZO-30 annealed at 800 ºC.....63

Figure 4-1. Picture of quartz box for thermal treatment of MoS_2.....73

Figure 4-2. Schematic illustration for the synthesis process of MoS_2 film used in this work. 74

Figure 4-3. Solution state $(NH_4)_2MoS_4$ is dissolved in DMF (a)after two day, (b)after one week, (c) in DMSO (d) in NMP after two day.....75

Figure 4-4. Photographs of the spin-coated MoS_2 films on NZO using the $(NH_4)_2MoS_4$ precursor solution dissolved in (a) DMF and (b) NMP.....76

Figure 4-5. TG/DTA chart of $(NH_4)_2MoS_4$ (a) raw material and it was dissolved in (b) NMP, (c) DMSO.....77

Figure 4-6. Photographs of the spin-coated MoS_2 films on (a) HfO_2 and (b) $(Bi,La)_3Ti_4O_{12}$

using the $(NH_4)_2MoS_4$ precursor solution dissolved in NMP. 79

Figure 4-7. XPS spectrum of (a)Mo 3d for La_2O_3, $YbTiO_x$, $LaTaO_x$ and BLT,(b)Ta 4f for $LaTaO_x$ and (c) Ti 2p for $YbTiO_x$. 81

Figure 4-8. Surface morphology of $(NH_4)_2MoS_4$ dissolved in NMP solution on (a) SiO_2 and (b) $Pb(Zr,Ti)O_3$. 82

Figure 4-10. XPS spectra for (a) Molybdenum (Mo) 3d and (b) Sulfur (S) 2p peaks of the solution-processed MoS_2 film with different annealing temperatures. 86

Figure 4-11. GI-XRD patterns of the MoS_2 film fabricated by (a) the solution process with various thermal treatment temperatures with H_2/Ar and (b) without H_2/Ar atmosphere. 88

Figure 4-12. Raman spectra of MoS_2 films fabricated by solution process with different annealing temperature. 90

Figure 4-13. MoS_2 film annealed at (a) 600, (b) 800 and (c) 1000 ºC on the NZO. 92

Figure 4-14. EDS profile of MoS_2 on NZO. (a) TEM image, (b) merged Nb and Zr distribution (c)Nb atoms and (d)Zr atoms distribution. 93

Figure 4-15. (a) Raman spectra of MoS_2 fabricated by source solutions with various concentrations. (b) Frequency difference between the peak of the E_{2g} and A_{1g} mode as a function of the concentration of the source solution. 95

Figure 5-1. Process diagram for TFT with MoS_2 and NZO film. 103

Figure 5-2. Energy band structure between multilayer MoS_2 semiconductor and Ti, Cr, Ni, Au and Pt metal 104

Figure 5-3. Plan view of metal pad for multilayer MoS_2 transistor and its Raman spectra 105

Figure 5-4. The characteristic of gate-voltage and drain current for the transistor before vacuum and thermal treatment. 107

Figure 5-5. After vacuum and thermal treatment, the characteristic of (a)gate-voltage and drain current and (b) drain-voltage and drain current. 108

Table of Contents

1. Introduction 9

1.1 Limitation of silicon based system and appearance of two dimensional materials 9

1.2 Molybdenum disulfide (MoS_2) 14

1.3 Research purpose 17

References 19

2. Experimental and Analytic methodologies 22

2-1 Experimental methodology 22

2-1-1. Sol-gel method 22

2-1-2. Spin-coating 24

2-2 Analytic methodology 26

2-2-1 Grazing incidence X-ray diffraction (GI-XRD) 26

2-2-2 Raman scattering spectroscopy 28

2-2-3 X-ray photoelectron spectroscopy (XPS) 31

2-2-4 Atomic force microscope (AFM) 33

2-2-5 Transmission electron microscope (TEM) and Scanning electron microscope (SEM) 35

2-2-6 Surface energy measurement 37

2-2-7 Tg/DTA 40

References 42

3. Fabrication and characterization of high-k gate dielectric film 44

3-1 Introduction 44

3-2 Fabrication procedure 47

3-3 Results and discussion 49

3-4 Summary 63

References 65

4. Fabrication and characterization for semiconductor layer using MoS_2 67

4-1 Introduction 67

4-2 Fabrication procedure 69

4-3 Results and discussion 74

4-4 Summary 96

References 97

5. Characterization of TFTs using NZO as gate dielectric and MoS_2 as semiconductor 100

5-1 Introduction 100

5-2 Fabrication procedure 101

5-3 Results and discussion 104

5-4 Summary 109

References 110

6. Conclusions **111**

6-1. Summary and conclusions of this research **111**

6-2. Future Prospects of this study **114**

Announcement list **116**

Acknowledgement **118**

1. Introduction

1.1 Limitation of silicon based system and appearance of two dimensional materials

The modern electronics was started from a discovery of the transistor operation by John Bardeen, Walter Brattain, and Wiliam Shockley in the late 1940's. In addition, metal-oxide-semiconductor field-effect transistor (MOSFET), which is a main device of the present large scale integrated circuits (LSI), was invented around 1960. The amount of intense work has been made in miniaturizing the transistor dimensions and improving their performance [1]. As shown in figure 1-1(a), the gate length (L_g) of the MOSFET is approaching to 10 nm wider. The size of individual silicon atoms (around 0.2 nm) would be a physical limit, but its behavior becomes unstable and difficult to control before the device size reaches to this limitation because of the short channel effect as shown in figure 1-1(b). As the L_g decreases, the space between diffused depletion regions near source and drain also decreases. When the short channel effect becomes serious, the electron can move from drain to source, irrespective of the channel controlled by gate voltage (punch through) [2]. It is thought that there are two primary paths to overcome the current performance limitations of silicon based transistors. One is the changing the conventional planar metal-oxide-silicon field effect transistor (MOSFET) structure to three dimension (3D) structures such as fin FET, vertical TFT [3]. However, when these new structure are scaled down, they will face the same limitation because they are also based on silicon MOSFET concept. The other path is applying new material instead of silicon such as two dimension (2D) materials (graphene, MoS_2 and so on). It is suggested that use of atomically thin 2D materials gives immunity to the short channel

effect. In addition, a good interface quality is expected in field-effect transistors using 2D materials because there is no dangling bond on 2D materials [4,5].

2D materials (figure1-2) such as graphene, BN, MoS_2 and black bone are crystalline materials which has a single layer of atoms. Among them, to replace the silicon based transistor, the graphene have firstly attracted significant attention. It was firstly observed in electron microscopes in 1962 by Russian, but only studied the material supported on metal surfaces. The successful isolation of graphene was conducted in 2004 by Andre Geim and Konstantin Novoselov at the University of Manchester [6].

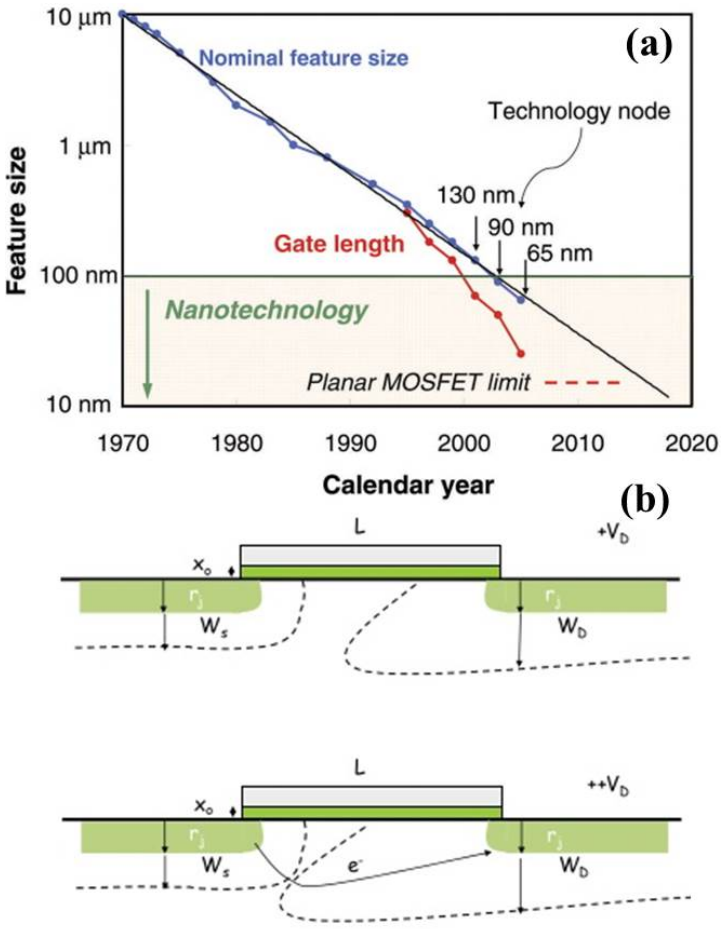

Figure 1-1. Gate length scaling path (a) and (b) the representative illustration of short channel effect and punch through

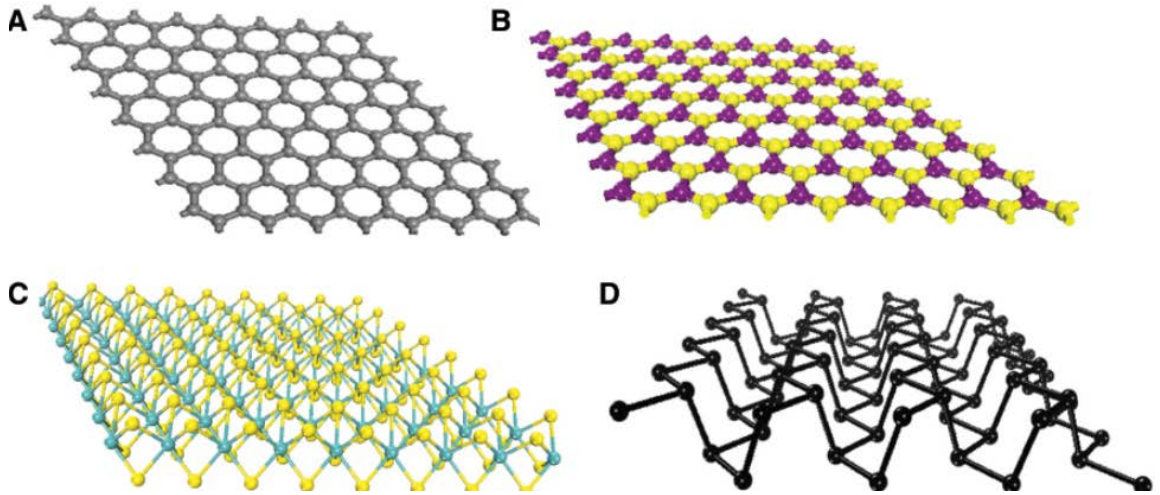

Figure 1-2. Representative 2D materials crystal structure of (a) graphene, (b)boron nitride, (c) molybdenum disulfide and (d) black bone.

The graphene has a hexagonal lattice structure with two carbon atoms in each unit cell as shown in figure 1-3(a). There is no vertical combination with carbon so the energy band structure of graphene is different from that of the conventional semiconductors [7] (figure 1-3(b)). The graphene has a Brillion zone (BZ) at six corners with degenerate conduction and valance bands so it has no energy band gap. Moreover, the dispersion relation curve is not quadratic like silicon semiconductor but linear near the BZ corner. It can be approached by the massless Dirac equation. Hence, it is called massless Dirac fermions for the electrons in graphene and Dirac points for the BZ corners [8]. The expected mobility for graphene is over 10^6 cm^2/Vs. It shows possibilities for the development of faster transistors with high transconductance, large gain and low consumption energy. The density of states at the Dirac points is zero so it makes graphene a semimetal. The unsual band structure of graphene has derived to a mount of attractive phenomena such as half-integer quantum Hall effect [9], Klein tunneling [10], electron focusing [11], RF electronics [12], advanced sensors [13],

semitransparent electrodes [14], low power switches [15], solar cells [16], battery energy storage [17], and tunable plasmonic devices for THz and mid-infrared applications [18].

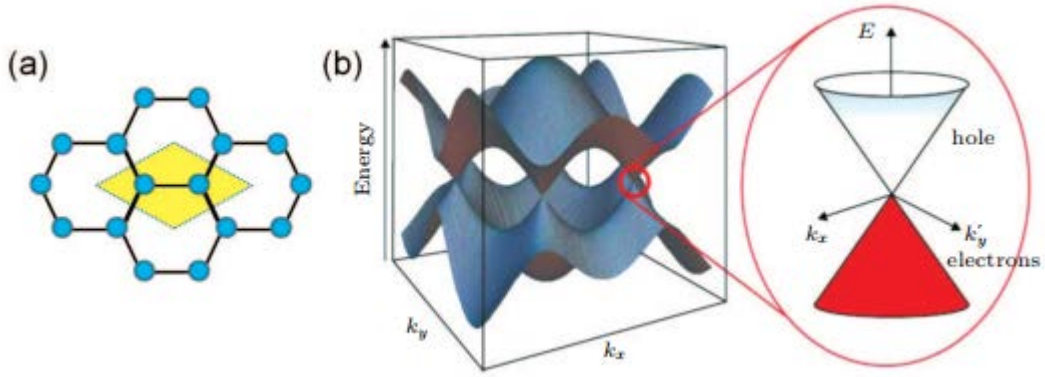

Figure 1-3. (a)The lattice structure of graphene (b) band structure. Enlargement of the band structure showing the Dirac cone.

However, since the bandgap (E_g) of graphene is zero, graphene-channel transistors usually show ambipolar behavior with low on/off current ratio [19]. Although many investigations have been conducted in order to generate the bandgap for graphene, it is difficult to obtain a sufficiently large bandgap for practical applications.

The hexagonal boron nitride (h-BN) as shown in figure 1-2(b) has repeated hexagon structure with atomically sheets but each side of the hexagon is a born and nitrogen combination instead of the carbon. Although the graphene is electrode, the h-BN is an insulator with 4.5 eV band gap (mono layer) even though it has same structure. Pacilé et al.[20] reported the investigation of exfoliated few layered h-BN at first.

The black phosphorus (BP) as shown in figure 1-2(d) is consisted with only phosphorus

atoms and has a layered structure. Bulk BP crystal has been studied extensively decades ago and there are many types of phosphorous structure. Among them, the most stable structure for an allotrope of phosphorus is orthorhombic. Each phosphorus atom is connected to two parallel adjacent atoms and to downward or upward one in black phosphorus. This vertical bond is repeated and it looks like ring oscillation. The width space in BP is around 0.53 nm and the lattice constant along vertical direction is 1.05 nm. Hence, the BP structure has reduced symmetry compared to graphene so it shows unique angle-dependent in-plane conductivities. The BP has a band gap between a graphene and BN so it can compensate the range for near and mid-infrared optoelectronics [21].

On the other hand, other types of 2D materials such as transition metal dichalcogenide (TMDC) as shown in figure 1-2(c) have properties which are different from the graphene, BN and BP. TMDC materials have bandgap. Hence, it is much easier to obtain transistors with large on/off ratio for TMDC than graphene. In addition, the TMDC monolayer does not have inversion region. It makes allows to generate a new degree of freedom of carriers [22]. TMDC monolayers have an energy band gap because of the strong spin-orbit coupling. It makes a spin-orbit splitting of several hundred meV in the valence region and a few meV in the conduction. Hence, there is possibility to tune the electron spin for excitation laser photon energy.

The bonding force between the layers for TMDC is Vander Waals force so it is often combined with other 2D materials like graphene and hexagonal boron nitride for heterostructure devices [23].

1.2 Molybdenum disulfide (MoS_2)

The molybdenum disulfide (MoS_2) is the inorganic compound composed of two elements (Mo, S) and classified as a metal dichalcogenide. In the first time, the MoS_2 have used as high quality lubricant because of excellent mechanical properties and relatively low reactivity (unaffected by dilute acids and oxygen) [24]. In recent time, atomically-thin layered MoS_2 has attracted attention as semiconductor since Radisavljevic *et al*. first demonstrated enhancement in carrier mobility (~200 cm^2/Vs) via top-gate dielectric engineering using exfoliated single MoS_2 layer at 2011 [25]. Since then, there are explosive researches in the development of field effect transistors (FETs), photo transistors/sensors, various integrated circuit (IC) modules and logic operators based on MoS_2 [26].

Bulk MoS_2 is composed of layers of monolayer MoS_2 weakly bonded by van der Waals force (vdW). Each monolayer of MoS_2 consists of hexagonally packed S-Mo-S units. Figure 1-4 shows the hexagonal structure of MoS_2 (2H-MoS_2) which as a whole exhibits hexagonal symmetry and the Mo atom has trigonal prismatic coordination. This phase has two layers per unit so it is named 2H. There are six S atoms bonded to each Mo atom with distance of 2.42 Å. In the 2H phase, the S atoms below the Mo atom are positioned exactly below the three S atoms which are bonded above the Mo atom because of this orientation when the structure is viewed from the top we can see only three sulfur atoms bonded to Mo atom. Bulk MoS_2 exists in this 2H phase and since the *d* orbitals are fully occupied, it behaves as a semiconductor.

Ellis *et al*.[27] calculated band structures of one to six layers and bulk MoS_2 using the screened hybrid density function theory. MoS_2 in bulk form is an indirect transition semiconductor with a band gap of 1.29 eV. When it is to be a monolayer, it becomes a direct

transition structure with an energy gap of 1.8 eV. As a second layer is added, it becomes an indirect transition semiconductor. With more added layers, the band gap agrees with that of a bulk crystal. The partial density of states for monolayer, bilayer, six layers and bulk MoS_2 are illustrated in figure 1-5. It can be confirm the effect of interlayer interactions on the band structure. For a bilayer, the conduction band along K to Γ line splits and shifts the minimum down leading to an indirect gap. The splitting increases with additional layers and hence reduces the gap.

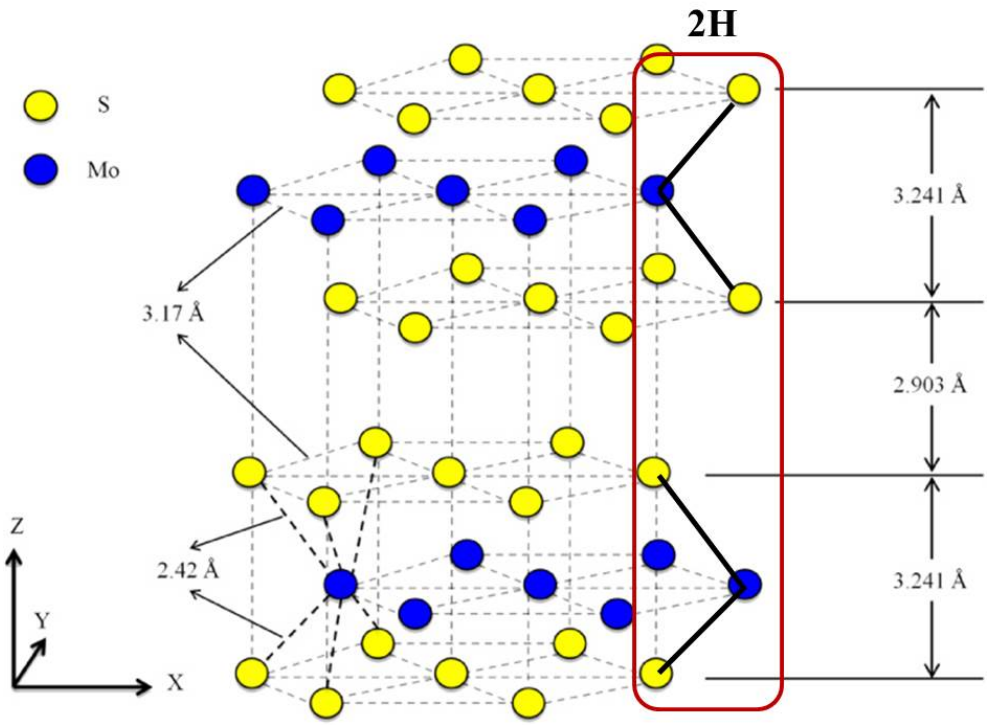

Figure 1-4. 2H structure of MoS_2 show the two layers per unit hexagonal structure.

The transistor using MoS_2 as a semiconductor shows an excellent gate control and high saturation current due to high carrier mobility of MoS_2 and it is chemically and thermally

stable at up to 100 ºC in an inert atmosphere. In case of silicon substrate, there are amount of dangling bonds which may produce defects leading to origin of noise. Since the MoS_2 has no dangling bond, it is expected that MoS_2 transistor shows very low noise. Moreover, a MoS_2 has good Mechanical properties. The stiffness is same as isopachous stainless steel and shows almost same degree of flexibility. It can also be stretched up to ten percent of its length [28]. These features of MoS_2 make this material promising for future electronics elements.

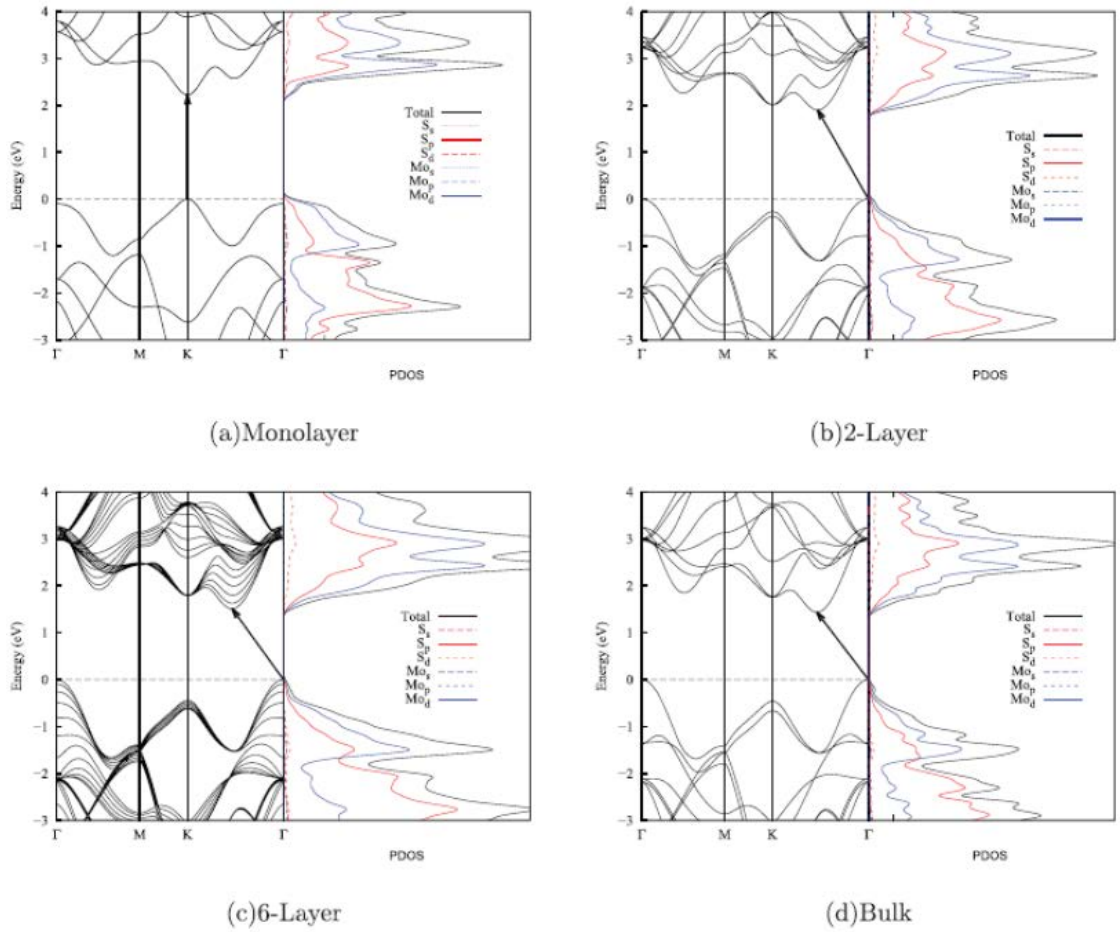

Figure 1-5. Calculated band structure of (a) monolayer, (b) bilayer, (c) hexalayer (d) bulk for MoS_2.

1.3 Research purpose

The objective of this research is to develop chemical solution process for MoS_2 thin films and to apply the solution-derived MoS_2 to thin film transistors. To achieve the TFT applications, MoS_2 films are grown on high-dielectric-constant (high-k) materials directly by chemical solution process.

Recently, exfoliated single layer MoS_2 has been applied to transistors, and excellent on/off current ratio with high carrier mobility [25] was reported. Several methods have been proposed to prepare MoS_2 layers, including physical [29] and chemical [30] exfoliation, chemical vapor deposition (CVD) [31], hydrothermal synthesis [32], electrochemical synthesis [33], sulfurization of molybdenum oxides [34] and Mo metal [35]. Nevertheless, most devices using the MoS_2 have been fabricated on small flake exfoliated from single crystals in order to investigate of fundamental properties [25]. However, there are many restrictions such as small and uncontrollable flake size and extreme difficulty in the alignment for device fabrication so it limits their application in macroscopic scale devices. On the other hand, the chemical solution process is promising for large area formation of MoS_2 with simple equipment at low cost. However, there are a few researches about chemical solution processes for MoS_2 films [36]. Therefore, in my work, chemical solution process for MoS_2 is systematically studied, including preparing precursor and optimizing thermal treatment process.

In addition, I prepared MoS_2 films directly on various high-k materials. Most demonstrations of MoS_2 synthesis such as CVD and solution-based deposition have been based on the silicon dioxide (SiO_2) or sapphire substrate because of the thermal stability and flat surface of the substrates, in such cases, the deposited MoS_2 film has to be transferred to

other substrates such as high-dielectric-constant (high-k) thin films to fabricate high-performance devices. However, during the transfer process of the MoS_2 film, problems including film wrinkle, chemical damage by etching solution of SiO_2 will rise. Hence, for practical thin film transistor (TFT) applications, it is preferable to directly investigate the process of fabricating a large-area MoS_2 film on high-k dielectric. In addition, there are two kinds of solution processes for MoS_2 fabrication: one utilizes a source solution with crystallized MoS_2 flakes dispersed in the solvent and the other uses chemical reactions of precursors which contain Mo and S elements with appropriate annealing steps. The latter is called "chemical" solution process and is promising for large-area and uniform MoS_2 fabrication at low cost.

In this work, direct deposition of MoS_2 films using a "chemical" solution process on high-k thin films has been investigated in a systematic manner. First, we demonstrate the coating properties of MoS_2 source solution prepared with $(NH_4)_2MoS_4$ dissolved in N-methyl-2-pyrrolidone on various kinds of high-k films. Next, we demonstrate the growth of MoS_2 films on Nb-doped ZrO_2 (NZO) film by using a two-step annealing method. This study also demonstrates that the thickness of the solution-derived MoS_2 can be controlled by the concentration of the source solution. Finally, the characteristic of TFT using MoS_2 as a semiconductor and NZO as a gate insulator will be investigated.

References

[1] Van Dormael, Armand, “The French Transistor”, Proceedings of the 2004 IEEE Conference on the History of Electronics, Bletchley Park, United Kingdom, 2004.

[2] Xing Zhou, Khee Yong Lim, D. Lim, “A general approach to compact threshold voltage formulation based on 2D numerical simulation and experimental correlation for deep-submicron ULSI technology development”, IEEE Transactions on Electron Devices, vol.47, pp.47, 2000.

[3] M.Jurczak, N.Collaert, A.Veloso, T.Hoffmann, S.Biesemans, “Review of FINFET technology,” 2009 IEEE International SOI Conference, pp.1, 2009.

[4] Q. H. Wang, K. Kalantar-Zadeh, A. Kis, J. N. Coleman and M. S. Strano, “Electronics and optoelectronics of two-dimensional transition metal dichalcogenides”, Nature Nanotechnology, vol.7, pp.699, 2012.

[5] Y. Yoon, K. Ganapathi and S. Salahuddin, “How Good Can Monolayer MoS2 Transistors Be?”, Nano Letter, vol. 11, pp.3768, 2011.

[6] Novoselov, K. S.; Geim, A. K.; Morozov, S. V.; Jiang, D.; Zhang, Y.; Dubonos, S. V.; Grigorieva, I. V.; Firsov, A. A. "Electric Field Effect in Atomically Thin Carbon Films", Science, vol.306, pp.666, 2004.

[7] Sarma S D, Adam S, Hwang E H and Rossi E,” Electronic transport in two-dimensional graphene“, Reviews of Modern Physics, vol.83, pp.407, 2011.

[8] Wang Xin-Ran, Shi Yi and Zhang Rong, ”Field-effect transistors based on two-dimensional materials for logic applications”, China Physics B, vol. 22, pp.098505, 2013.

[9] Zhang Y, Tan Y W, Stormer H L and Kim P, “Experimental observation of the quantum Hall effect and Berry's phase in graphene”, Nature, vol.438, pp.201, 2005.

[10] Young A F and Kim P,” Quantum interference and Klein tunnelling in graphene heterojunctions”, Nature Physics, vol.5, pp.222, 2009.

[11] Cheianov V V, Fal’ko V and Altshuler BL,” The focusing of electron flow and a Veselago lens in graphene p-n junctions”, Science, vol.315, pp.1252, 2007.

[12] H. Wang, A. L. Hsu, and T. Palacios, “Graphene Electronics for RF Applications,” IEEE Microwave Magazine, vol. 13, pp. 114, 2012.

[13] P. K. Ang, W. Chen, A. T. S. Wee, and K. P. Loh, “Solution-Gated Epitaxial Graphene as pH Sensor,” Journal of the American Chemical Society, vol. 130, pp. 14392, 2008.

[14] G. Eda, G. Fanchini, and M. Chhowalla, “Large-area ultrathin films of reduced graphene oxide as a transparent and flexible electronic material,” Nature Nanotechnology, vol. 3, pp. 270, 2008.

[15] K. M. Milaninia, M. A. Baldo, A. Reina, and J. Kong, “All graphene electromechanical switch fabricated by chemical vapor deposition,” Applied Physics Letters, vol. 95, pp. 183105, 2009.

[16] X. Wang, L. Zhi, and K. Mullen, “Transparent, Conductive Graphene Electrodes for DyeSensitized Solar Cells,” Nano Letters, vol. 8, pp. 323, 2008.

[17] E. Yoo, J. Kim, E. Hosono, H. Zhou, T. Kudo, and I. Honma, “Large Reversible Li Storage of Graphene Nanosheet Families for Use in Rechargeable Lithium Ion Batteries,” Nano Letters, vol. 8, pp. 2277, 2008.

[18] L. Ju, B. Geng, J. Horng, C. Girit, M. Martin, Z. Hao, H. A. Bechtel, X. Liang, A. Zettl, Y. R. Shen, and F. Wang, “Graphene plasmonics for tunable terahertz metamaterials,” Nature Nanotechnology, vol. 6, pp. 630, 2011.

[19] K. Novoselov, “Graphene: Mind the gap”, Nature Materials, vol.6, pp.720, 2007.

[20] Pacile, D., Meyer, J. C., Girit, C. O. & Zettl, A., “The two-dimensional phase of boron nitride: few-atomic-layer sheets and suspended membranes”, Applied Physics Letter, vol.92, pp.133107, 2008.

[21] F. Xia, H. Wang, Y. Jia, “Rediscovering Black Phosphorus as an Anisotropic Layered Material for Optoelectronics and Electronics”, Nature Communications, vol.5, pp.4458, 2014.

[22] Zeng, H.; Dai, J.; Yao, W.; Xiao, D.; Cui, X., "Valley polarization in MoS_2 monolayers by optical pumping", Nature Nanotechnology, vol.7, pp.490, 2012.

[23] Rycerz, A.; Tworzydło, J.; Beenakker, C. W. J., "Valley filter and valley valve in graphene", Nature Physics, vol.3, pp.172, 2007.

[24] Roger F. Sebenik, A. Richard Burkin, Robert R. Dorfler, John M. Laferty, Gerhard Leichtfried, Hartmut Meyer-Grünow, Philip C. H. Mitchell, Mark S. Vukasovich, Douglas A. Church, Gary G. Van Riper, James C. Gilliland retired, Stanley A. Thielke, "Molybdenum and Molybdenum Compounds", Ullmann's Encyclopedia of Chemical Technology,vol.10, pp.655, 2005.

[25] B. Radisavljevic, A. Radenovic, J. Brivio, V. Giacometti & A. Kis, “Single-layer MoS_2 transistors”, Nature nanotechnology, vol.6, pp.147, 2011.

[26] Hyong Seo Yoon, , Hang-Eun Joe, Sun Jun Kim, Hee Sung Lee, Seongil Im, Byung-Kwon Min and Seong Chan Jun, “Layer dependence and gas molecule absorption property in MoS_2 Schottky diode with asymmetric metal contacts”, Nature communications, vol.3, p.1011, 2012.

[27] Ellis, J. K., Lucero, M. J. & Scuseria, G. E., “The indirect to direct band gap transition in multilayered MoS_2 as predicted by screened hybrid density functional theory”, Applied Physics Letter, vol.99, pp.261908, 2011.

[28] Akinwande, Deji; Petrone, Nicholas, Hone, James, "Two-dimensional flexible nanoelectronics", Nature Communications, vol.5, pp.5678, 2014.

[29] D. Xiao, G. B. Liu, W. Feng, X. Xu and W. Yao, “Coupled Spin and Valley Physics in

Monolayers of MoS_2 and Other Group-VI Dichalcogenides", Physics Review Letter, vol.108, pp.196802, 2012.

[30] N. Coleman, M. Lotya, A. O. Neill, S. Bergin, P. King, U. Khan, K. Young, A. Gaucher, S. De and R. Smith, "Two-dimensional nanosheets produced by liquid exfoliation of layered materials", Science, vol.331, pp.568, 2011.

[31] Y. Yu, C. Li, Y. Liu, L. Su, Y. Zhang and L. Cao," Controlled Scalable Synthesis of Uniform, High-Quality Monolayer and Few-layer MoS_2 Films", Scientific Report, vol.3, article number 1866, 2013.

[32] Y. Peng, Z. Meng, C. Zhong, J. Lu, W. Yu, Y. Jia and Y. Qian, "Hydrothermal synthesis and characterization of single-molecular-layer MoS_2 and $MoSe_2$", Chemical. Letter, vol.8, pp.772, 2001.

[33] Q. Li, J. T. Newberg, J. C. Walter, H.C. Hemminger and R.M. Penner, "Polycrystalline molybdenum disulfide (2H-MoS_2) nano-and microribbons by electrochemical/chemical synthesis", Nano Letter, vol.4, pp.277, 2004.

[34] Y. C. Lim, W. Zhang, J. K. Huang, K. Liu, Y. H Lee, C. T. Liang, C. W. Chu and L. J. Li. "Lithography-free plasma-induced patterned growth of MoS2 and its heterojunction with graphene", Nanoscale, vol.4, pp. 6637, 2012.

[35] Y. Lee, J. Lee, H. Bark, I. K. Oh, G.H. Ryu, Z. Lee, H. Kim, J. H. Cho, J. H. Ahn and C. Lee, "Synthesis of wafer-scale uniform molybdenum disulfide films with control over the layer number using a gas phase sulfur precursor", Nanoscale vol.6, pp.2821, 2014.

[36] A. O'Neill, U. Khan, and J. N Coleman, "Two-dimensional nanosheets produced by liquid exfoliation of layered materials", Chemistry of Materials, vol.24, pp.2414, 2012.

2. Experimental and Analytic methodologies

2-1 Experimental methodology

2-1-1. Sol-gel method

Around 1970, three different groups in the field of inorganic materials published research results on preparation of glass and ceramics via solution or sol-gel route. H. Dislich prepared a pyrex-type borosilicate glass lens by heating a compact of metal alkoxide derived powder at temperatures as low as 650 ˚C [1]. Mazdiyasni et al. showed that well-sintered, dense ferroelectric ceramics can be obtained at temperatures as low as 900 ˚C, when sol-gel powders prepared from solutions of metal alkoxides are employed for sintering [2]. These works encouraged attention for a sol-gel preparation of inorganic materials, such as glasses and ceramics. Materials scientists and engineers paid attention to the possibility of this method in giving shaped materials directly from a solution without passing through the powder processing and the fact that the maximum temperature required for ceramics. Thus, many efforts have been made in preparing bulk body, coating film, membrane, fiber and particle, and many commercial products were born [3].

The significant characteristics unique to the sol-gel method became evident, when organic-inorganic hybrid materials were prepared by H. Schmidt and silica materials containing functional organic molecules were prepared by Avnir [4,5] in early 1980`s. Such materials are produced at low temperatures near room temperature, where no decomposition of organic matter takes place. Low temperature synthesis and preparation of materials is including not only glasses and ceramics but also organic and biomaterials [6].

Metal alkoxide ($M(OR)_n$) is derived from a alcohol (ROH) which has good controllability and is inexpensive organic compounds. It is easy to be decomposed by an acid via hydrolysis and thermal treatment and it finally make high purity hydrated oxides. This competitive process makes metal alkoxide the most common candidates for the solution precursor. The $M(OR)_n$ has high reactivity due to the presence of electronegative alkoxy groups. It makes the metal atoms in $M(OR)_n$ highly prone to nucleophilic combine. The reaction between $M(OR)_n$ and XOH molecule which has reactive hydroxyl groups, can be followed as eq.2-1:

$$\mathbf{M(OR)_n + (XOH)_x \rightarrow M(OR)_{n-x}(OX) + (ROH)_x} \quad \text{(eq.2-1)}$$

The chemical nature of X is important factor to decide the reactions such as hydrolysis (X = H), condensation (X = M) or chemical modification (X = R).

A nucleophilic substitution is followed as three step process:

1st. The nucleophilic addition is occurred from reaction of XOH group onto the positive charge metal atom.

2nd. The Proton is transferred from the transition state ($M(OR)_n(XOH)$) to the remnant alkoxy group.

3rd. The positive charge protonated species is taken off.

This reaction process depends on a charge distribution between the alkoxide and the transition state. Normally, the metal atom (M) and the remnant parts (ROH) must be positive. To obtain more accurate description of the reaction, the information of charge distribution in molecules is important. The Partial Charge Model usually used to investigate the charge distribution in given molecules [7].

2-1-2. Spin-coating

A spin coating is one of the most common methods to make a thin film on substrates and is used widely at variety of researches. The spin coating can be very easy to produce a uniform film from several nanometers to a few microns in thickness and it has good reproducibility [8]. The spin coating is used in organic electronics and nanotechnology. There are many kinds of the technique used in other semiconductor industries for the relatively thin films but also high uniformity are required for effective device preparation such as a self-assembly and organization to occur during the casting process.

The typical process for spin coating showed total process in figure 2-1. First of all, a small drop of a solution is dispensed on the center of a substrate. There are two common methods for spin-coating; static and dynamic dispense. The static dispense just drop a small solution on substrate. In this case, it needs much solution to cover full of substrate when the solution has high viscosity and large size substrate. Hence, to reduce the waste of solution, the low speed spinning step is inserted (dynamic dispense) because it does not need to deposit a solution to cover entire surface of the substrate. Dynamic dispense is particularly available when a fluid or substrate has poor wet ability. After the dispense process, it is accelerated to a high speed to make thin fluid to be desired thickness. The substrate is rotated at relatively low spinning speed to spread entirely due to the interplay with centripetal force and surface tension of the solution, and then it is rotated at high speed. During rotation, the desired material (precursor) is left due to evaporation of the solvent and the over flowed solution is lifted off because of a centripetal acceleration. In this step, the typical spin speeds range from 1500-6000 rpm for 10 seconds to several minutes. The final film thickness is determined by the combination of spin speed and time. In general, higher spin speeds and longer spin times

generate thinner film [9]. Finally, to eliminate remained solvent, the substrate is heated on hot-plate for a short time. The final film thickness is affected by the nature properties of the precursor solution such as viscosity, boiling temperature, contain percent of precursor and surface tension. Moreover, the final rotational speed, rate of increase and fume exhaust also contribute to the properties of coated film [10].

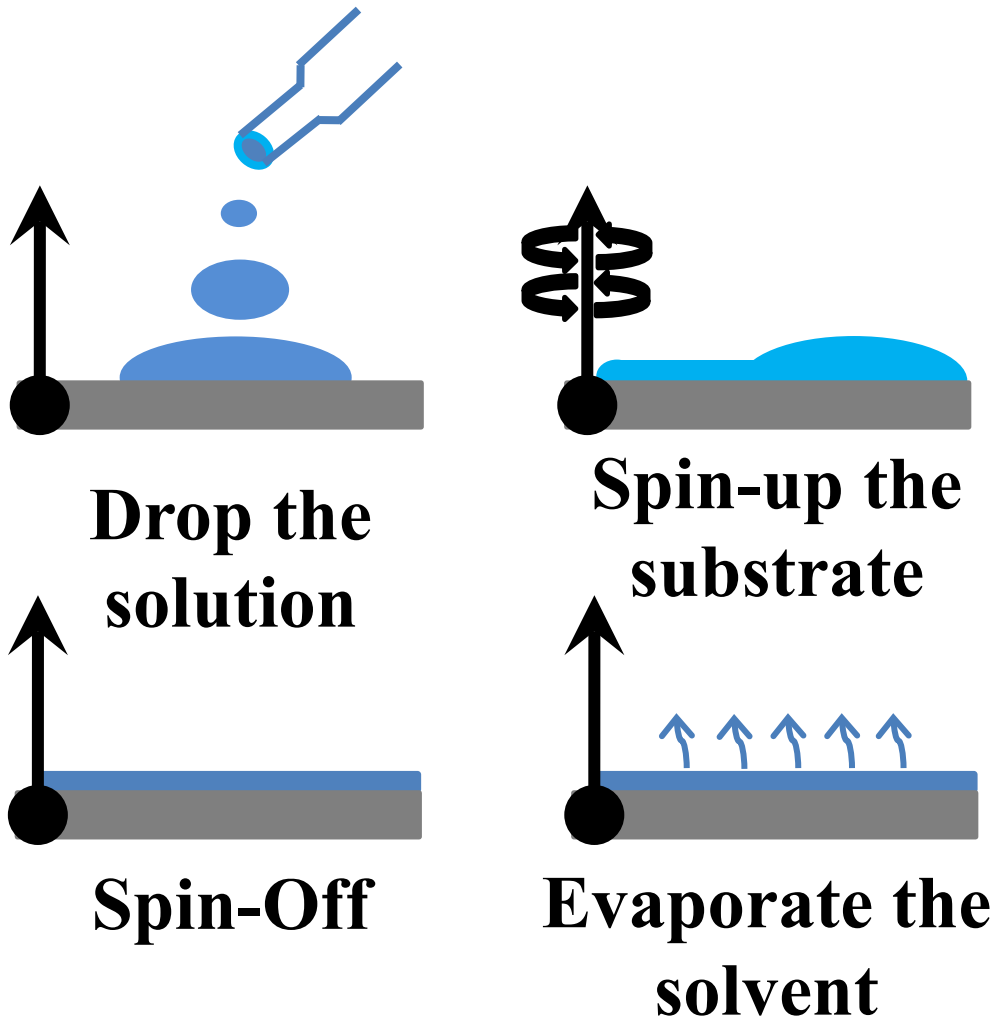

Figure 2-1. Illustration of the spin-coating process.

2-2 Analytic methodology

2-2-1 Grazing incidence X-ray diffraction (GI-XRD)

Many materials are crystalline which has the repeated structure. These crystals are composed by unit cells which the smallest number of atoms is contained. The dimension size of its unit cells is lattice parameter. The most famous method to determine the lattice constant of a crystalline is X-ray diffraction (XRD) using Bragg's law (eq.2-2). When two parallel waves was reflected by atoms on two parallel lattice planes, the wave which go to second lattice plane will travel an extra distance(l) in Figure 2-2. This diffracted wave has more travel distance ($2l$) than diffracted from first lattice plane. The distance $2l$ and diffracted angle (θ) depend on the distance of the two planes (d) in Figure 2-2 and its relationship is indicated by the function of $l=d\sin(\theta)$. If the $2l$ is equal to a wavelength (λ) or integer multiples of λ (i.e. $n\lambda$), the reflected waves will have same phase. Hence, the intensity of amplitude is to be maxima when the phase shift is exactly equal to $n\lambda$. This process is comprised in equation 2.2 which is so called the Bragg's law equation.

$$\boldsymbol{d=n\lambda/2\sin(\theta)} \text{ (eq.2.2)}$$

The crystalline structure of NZO and MoS_2 was investigated with the grazing incidence X-ray diffraction (GI-XRD). When XRD measurement is conducted using a conventional $\theta/2\theta$ scanning methods for thin film (< 1μm), relatively small signal from the film are produced because most X-Ray penetrated the thin film. For example, the data is shown in figure 2-3 to compare the difference of GI-XRD. Figures 2-3 shows a comparison of both a GI-XRD and a conventional $\theta/2\theta$ analysis for CdSeS thin film deposited on graphite. While there are only three peaks for graphite using the conventional method (figure 2-3 (b)), the GI-XRD methods

provides not only detail information for CdSeS thin film but also CdS component and graphite [11].

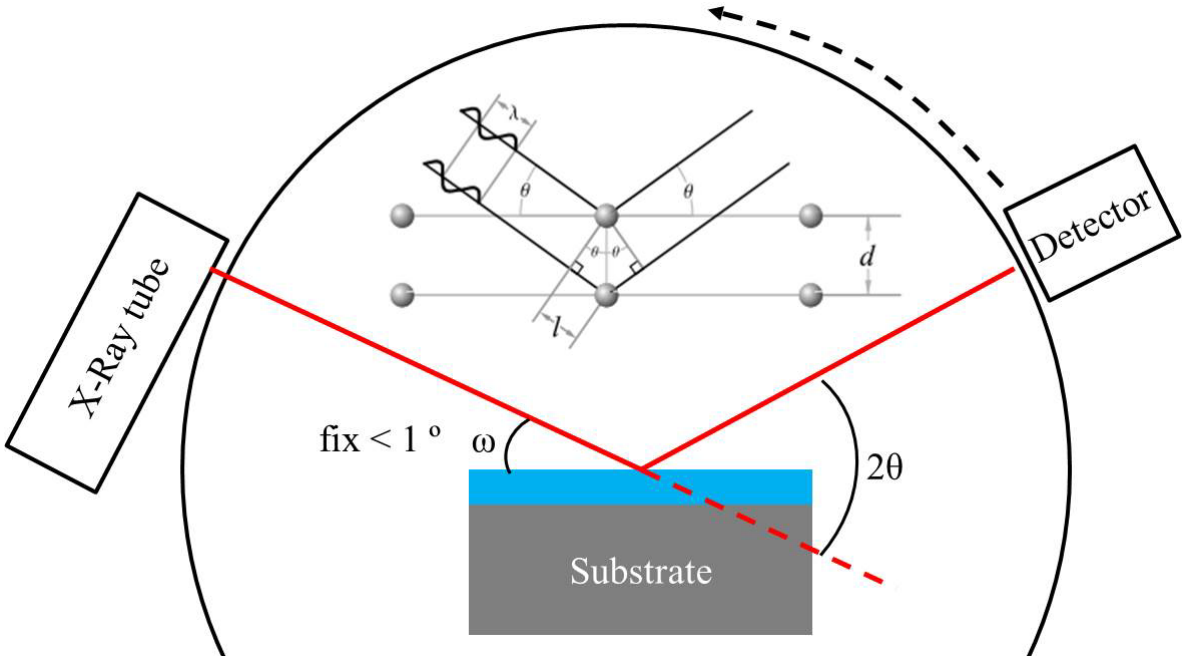

Figure 2-2 Schematic of GI-XRD.

In my experiments, the thickness of MoS_2 was under 10 nm so to obtain stronger signal, a scan with a fixed grazing angle (ω in figure 2-2) of incidence is conducted. The ω is generally chosen to be small angel range ($0^o<\omega<1$ °) to increase the travel pass. In my case, I set the ω where it showed the intensity of peak at 14 °. GI-XRD was analyzed using X`PERT PRO with a monochromatic Cu Kα (1.542 Å) X-ray source.

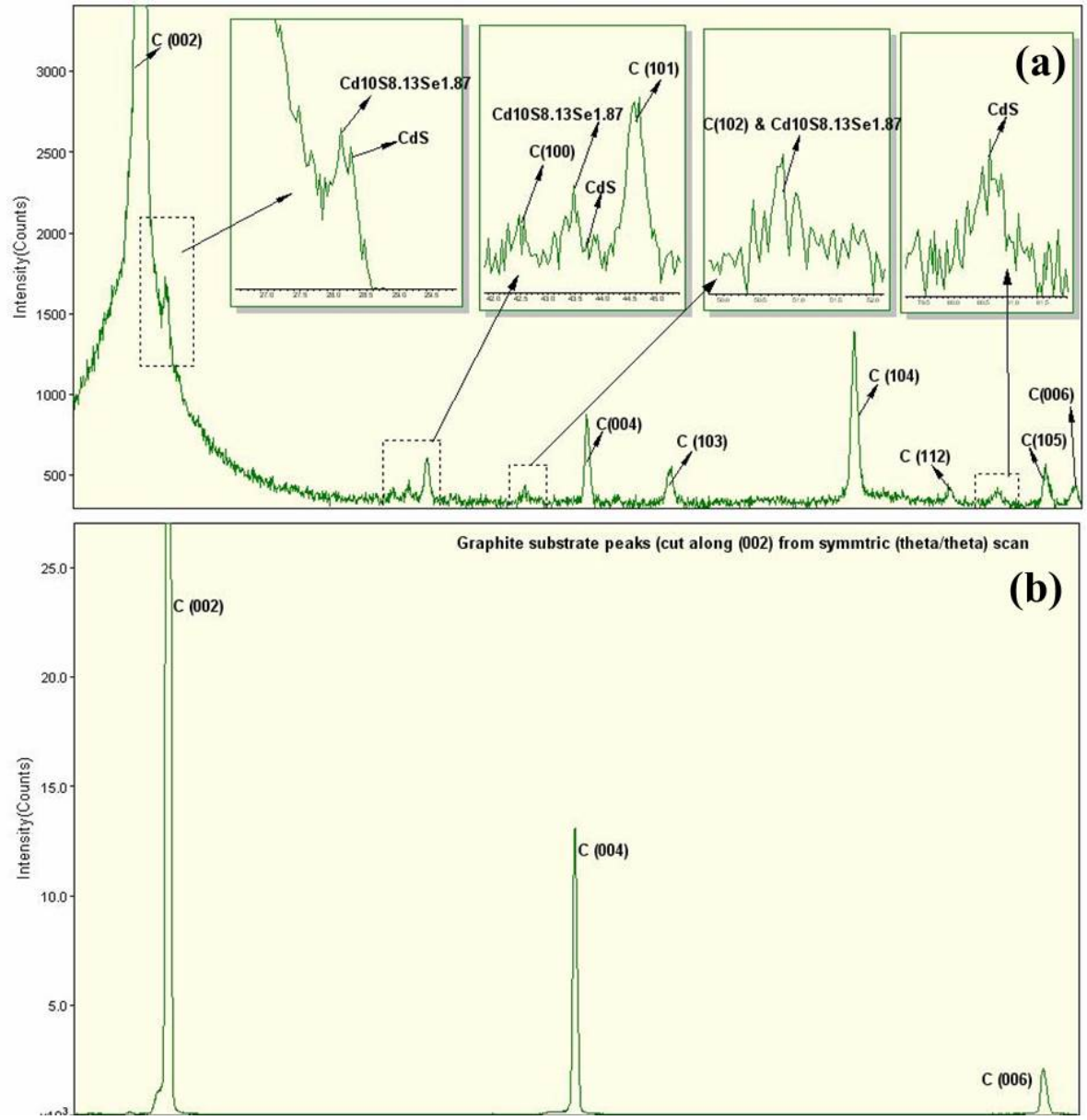

Figure 2-3 Comparison of XRD data measured by (a)GI-XRD (b)normal θ-2θ for CdSeS.

2-2-2 Raman scattering spectroscopy

Raman Spectroscopy is measurement of a vibration in molecular technique used to collect unique chemical information [12]. Each molecule has a different set of vibrational energy levels, and the photons emitted have unique wavelength shifts. When a monochromatic light

normally produced by a laser, is induced on the sample, the scattered photons almost have the same energy (elastic so called Raleigh scattering). This scattering phenomenon is main reason for the blue color of the sky. At short wavelength, it more effective and it is proportional to the fourth power of the frequency. However, a small fraction of the incidents photons (about $1/10^7$) is scattered due to interaction of molecular at optical frequencies different from the frequency of the incident photons (inelastic so named Raman scattering). Raman scattering can be occurred by a vibrational and rotational energy of a molecule.

The energy difference between the incident photon and the Raman scattered photon is same as the energy for a vibration of the scattering molecule (eq.2.3).

$$\underline{\boldsymbol{\omega}} = 1/\lambda_{incident} - 1/\lambda_{scattered} \quad \text{(eq.2.3)}$$

where $\underline{\boldsymbol{\omega}}$: Raman shift in wave number (cm^{-1}).

In case of 2H-MoS_2, there are several vibration (E^1_{2g} and A_{1g}) modes as shown in figure 2-4. Among them, four first-order Raman active modes (A_{1g}, E_{2g}^1, E_{1g} and E_{2g}^2) are used for a MoS_2 Raman spectroscopy studies. As shown in Figure 2-4, the A_{1g} mode shows the out-of-plane vibration of the S atoms. The other three first-order Raman active modes shows the in-plane vibrations. Among these modes, although E_{2g}^2, and E_{1g} is positioned under 50 cm^{-1}, the A_{1g} and E_{2g}^1 mode is located near 400 cm^{-1} so it is easy to be measured.

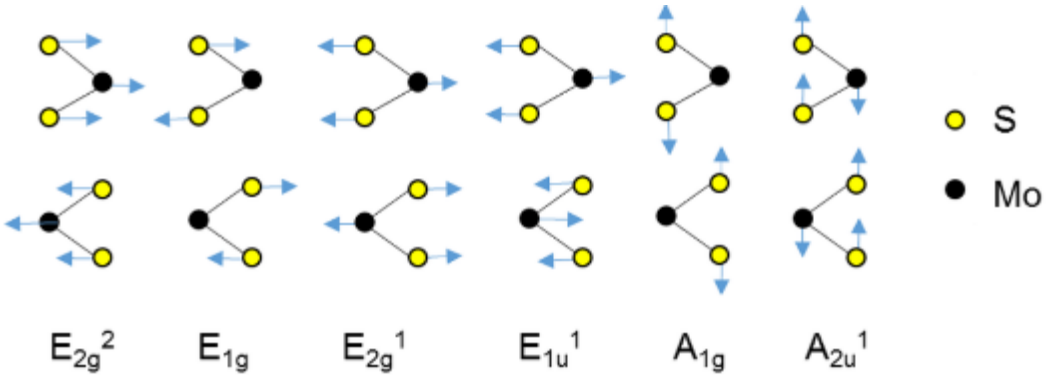

Figure 2-4. Vibration motion for the four first order Raman-active (E_{2g}^2, E_{1g}, E_{2g}^1 and A_{1g}) and the two dipolmoment-active (E_{1u}^1 and A_{2u}^1 modes).

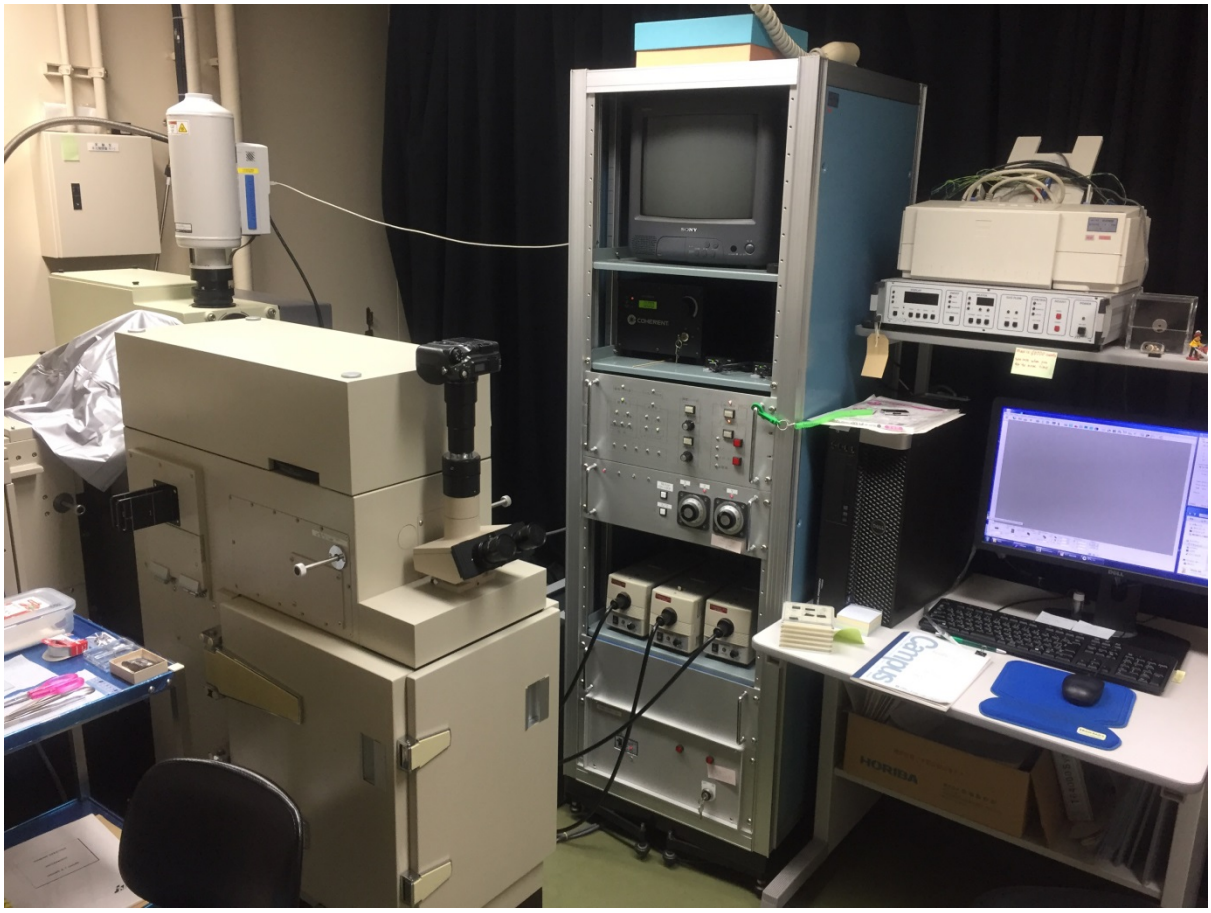

Figure 2-5. Picture of Raman scattering experiment of T64000.

In my experiment, the Raman scattering spectroscopy characteristics of the synthesized MoS_2 films were analyzed using T64000 (Horiba corp. figure 2-5 with a wavelength of 532 nm and a power of 20 mW. The elastically scattered light is filtered out using holographic gratings and multiple dispersion stages or more recently in the modern instruments using band-stop filters. The selected light is then detected by a photo-multiplier or CCD detector.

2-2-3 X-ray photoelectron spectroscopy (XPS)

Photoelectron spectroscopy is the technique detecting a photo-ionization and analysis of the kinetic energy of the emitted photoelectrons to investigate the composition and electronic state near the surface region (under 10 nm).

As shown in figure 2-6, the photon radiated by monochromatic source normally used X-Ray, is absorbed in a material then, ionization and the emission of a core (inner shell) electron are occurred with following equation (eq.2.4):

$$M + h\nu \rightarrow M^+ + e^- \text{ (eq.2.4)}$$

where h: Planck constant, ν :frequency, M (atom), e:electron.

From the conservation of energy rule, equation is changed following (eq.2.5):

$$E(M) + h\nu = E(M^+) + E(e^-) \text{ (eq.2.5)}$$

The eq.2.5 can be changed to eq.2.6 because the electron's energy can be present by kinetic energy (KE).

$$KE = h\nu - [\mathbf{E(M^+) - E(M)}] = h\nu - \mathbf{BE} \text{ (eq.2.6)}$$

The indicated brackets in eq.2.6 represent the energy difference between the ionized and neutral atoms so called the binding energy (BE) of the electron. For every element, there is a specific binding energy due to each core atomic orbital. This means that any detected electrons provide a specific fingerprint of the atomic species [13].

In my experiment, the XPS was conducted using an AXIS ULTRA (figure 2-7) with a monochromatic Al Kα (1486.7 eV) X-ray source for NZO and MoS_2 films.

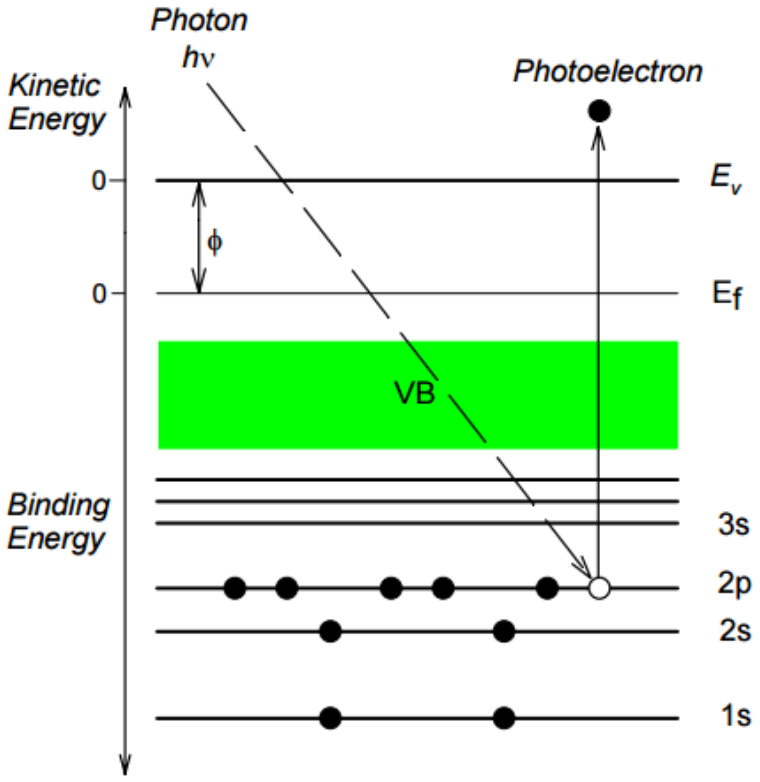

Figure 2-6. Schematic for the generation of energy difference by the photoemission.

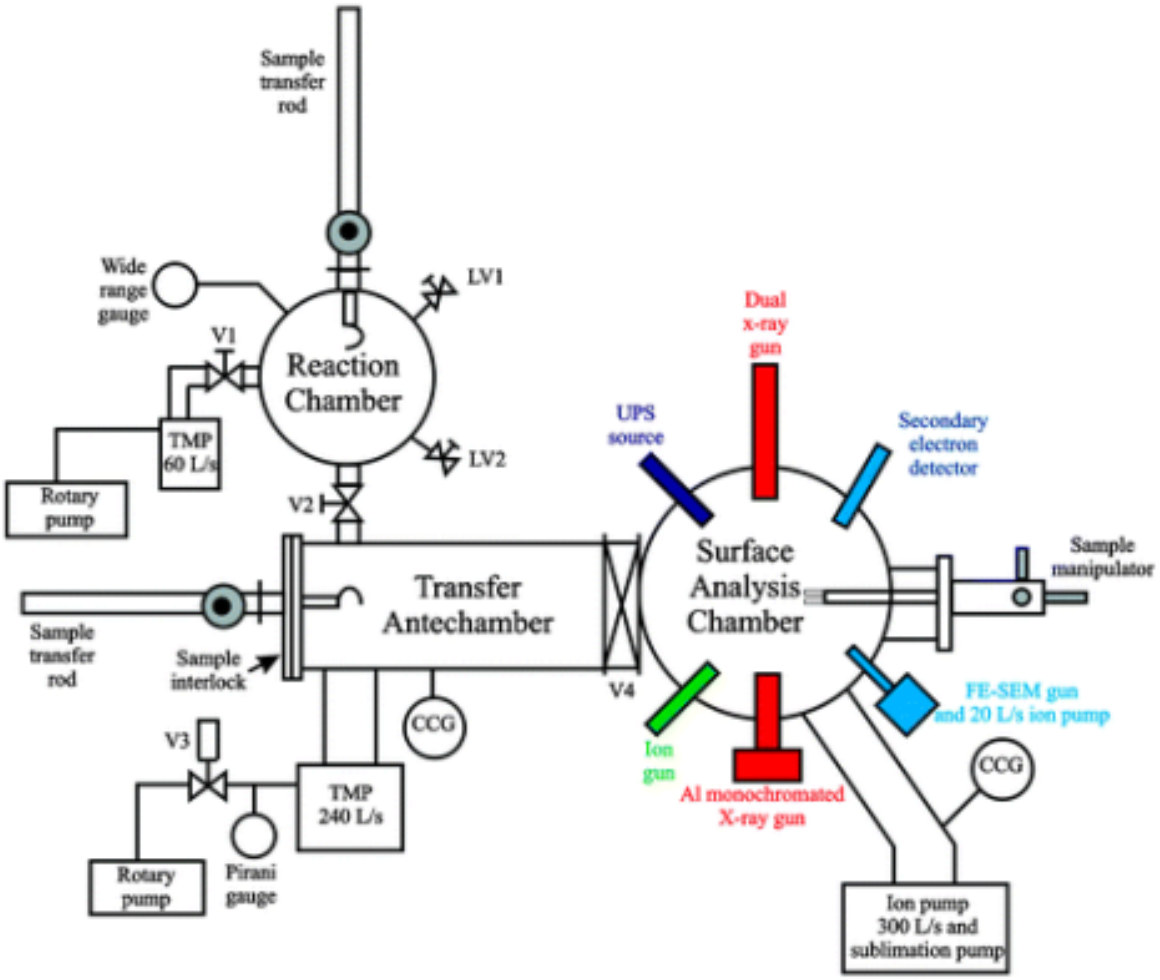

Figure 2-7. Schematic of the Kratos Axis Ultra XPS system.

2-2-4 Atomic force microscope (AFM)

Atomic Force Microscopy (AFM) as shown in figure 2-8 is an indirect imaging technique to record the three dimensional topography by sensing the force between a sample and a probing tip. AFM typically uses a silicon or silicon nitride cantilever which has a sharp tip with a few nanometer radiuses.

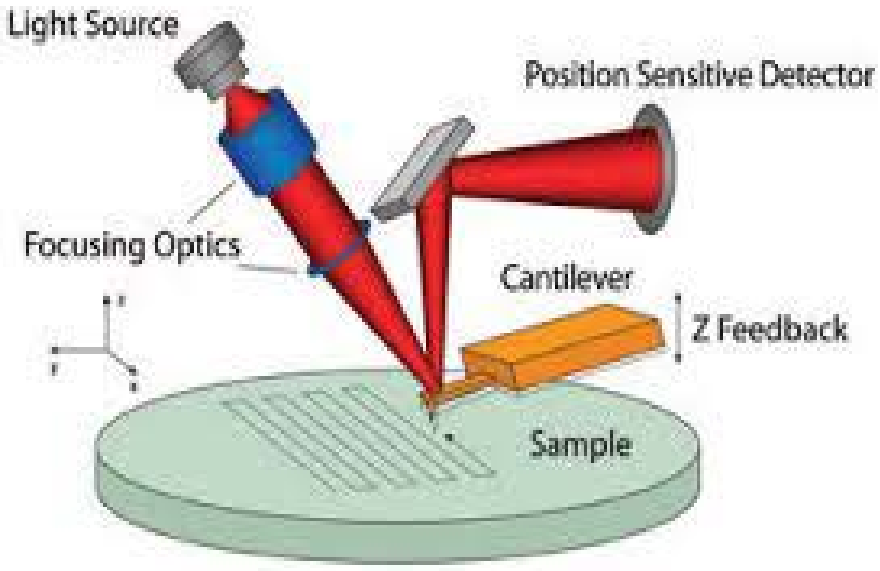

Figure 2-8. Schematic diagram of AFM

As the tip is close to the sample surface, the van der Waals force between the tip and the sample surface is increased. The force curve depends on the distance between the tip and the sample, is shown in Figure 2-9. There are two kinds of scan mode (contact and non-contact). In the contact mode, the repulsive force is used because the cantilever is closed less than a few angstroms to the sample surface (bold black line in left side of figure 2-9). The non-contact mode is used the attractive force which is generated by long-range van der Waals interactions. In this mode, the cantilever maintains the space of ten to hundred Å from the sample surface.

The cantilever moves back and forward on the surface to scan. The force on the cantilever varies depending on the surface height profile. A small integrated circuit with a piezo-electric crystal maintains a constant height difference (hence, a constant force). A laser is induced to back of the cantilever and the sensitive photo detector check the position changing of reflected laser. From this process, the height difference on the sample surface is calculated [14].

In my experiment, the AFM is used for the observation of surface morphology of NZO film using SII ARM4800 model.

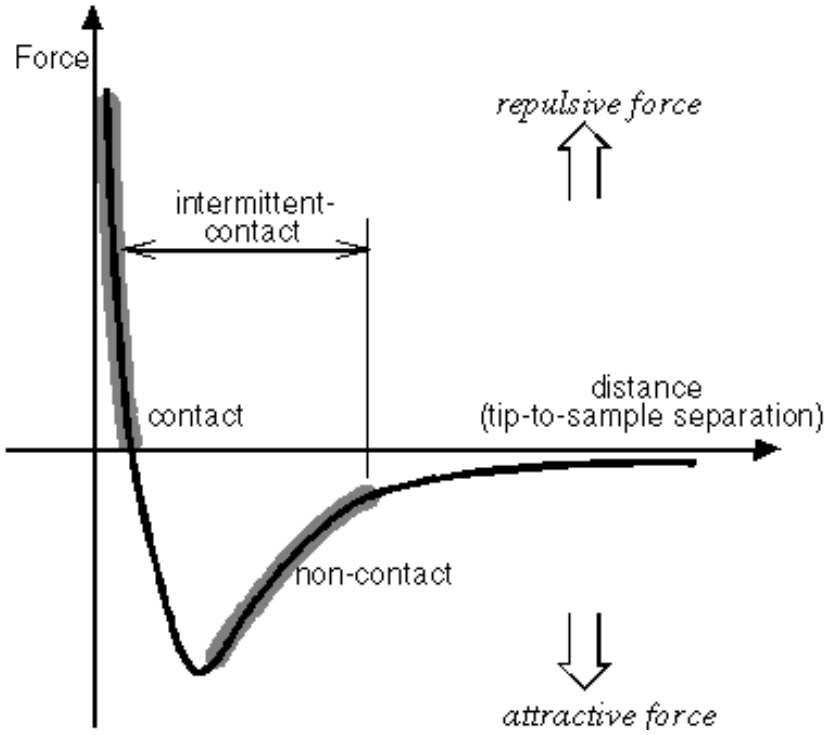

Figure 2-9. Force curve of AFM

2-2-5 Transmission electron microscope (TEM) and Scanning electron microscope (SEM)

A scanning electron microscope (SEM) is a valuable utility for imaging beyond the visible light diffraction limit. It uses a high energy electron beam (typically 0.1 to 50 keV) to scan the surface to generate an image profile. The incident electrons which have high energy can eject the electrons in outer shell of the sample atom. After undergoing additional scatterings within the sample, a fraction of these electrons leave the sample surface. These low energy

electrons emerging from the surface with energies less than 50 eV is named the secondary electrons. The SEM detects these secondary electrons and produces the whole sample image.

TEM was invented at 1931 by Max Knoll and Ernst Ruska, earlier than SEM at 1942. TEM was developed later because of the complex control of the machine's scanning. TEM is microscopy equipment in which an high energy electron is passed through an ultra-thin sample unlike SEM. Then, the penetrated electrons from the sample form two dimensional images which is magnified and focused by the several lens and it is detected by exposing to film or a charge coupled device camera. The TEM has small electron scattering in the sample so it has higher resolution than the SEM.

There is several similarities between SEM and TEM. Both are microscope to defect an electron and also use electrons (specifically, electron beams). Moreover, the samples in measurement are damaged due to high electron energy and sometimes it was mixed with a particular element in order to produce better quality observation. However, there is difference between SEM and TEM. The SEM use scattered electrons while TEM use transmitted electrons. There is a scattered electrons in SEM are divided as backscattered, secondary electrons. However, there are only transmitted electrons in TEM. In SEM, the scattered electrons are collected and counted to produce the image but in TEM, electrons are directly exposed to the image. In the strict sense, the purpose of analysis is also different. The SEM focuses on surface morphology of the sample but the TEM glance what is inside or beyond the surface. SEM also shows the sample bit by bit while TEM shows the sample as a whole. In case of the magnification, TEM has over several hundred million magnification level. It is 100 times higher than SEM of maximum magnification. Hence, the resolution of TEM (0.5 Å) is much higher than SEM (4 Å). However, SEM can give a better depth profile compared to TEM [15].

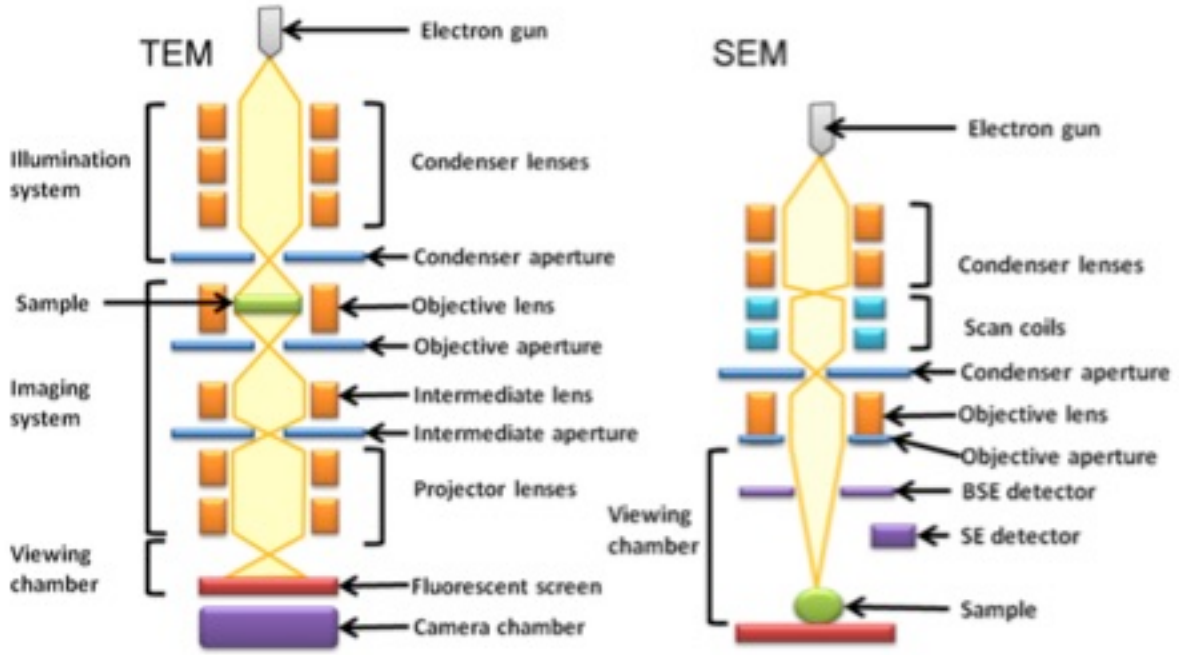

Figure 2-10. TEM vs SEM electron optics schematics.

In my experiment, the SEM (Hitachi S-5200) was used for observation surface morphology and the TEM was used performed using JEM-ARM200F with acceleration energy of 200 keV for the vertical image of films.

2-2-6 Surface energy measurement

The interpretation of surface energy has started from the macroscopic thermodynamic description using Young's equation. The surface energy depends on the interfacial intermolecular forces which are two representative components; non-polar (van der Waals) and polar (hydrogen bonding). The polar inter-force can be further spitted out electron acceptor or electron donor. The surface energy of substrate had been tried to estimate

indirectly using the measurement of contact angle by Zisman [16]. The surface energy can be quantitatively measured from the interactions between the surface and the standard liquids which have different interfacial components. To explain this method and the inter-force balance between the solid and liquid, Young's equation (eq.2.4) was used. In this case, the contact angles have to be larger than zero (Figure 2-11).

$$\gamma_S = \gamma_L \cos\theta + \gamma_{SL} \quad \textbf{(eq.2.4)}$$

where θ: the contact angle, γ_L: surface free energies of the liquid, γ_S: surface free energies of the solid and γ_{SL}: surface free energies between solid and liquid.

When the surface tension of the liquid is less than surface tension of the substrate, the liquid can be covered on the entire substrate.

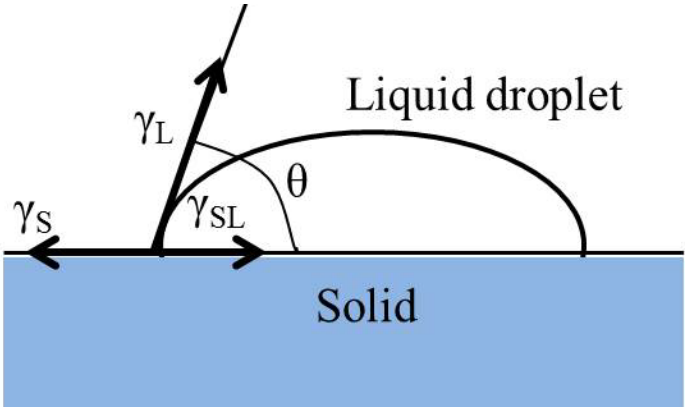

Figure 2-11. Contact angle of a liquid on a surface.

In the recent times, Young's equation is extended to interpret more accurate for surface

energy. Van Oss-Chaudhury-Good (vOCG) acid-base theory (eq. 2.7) which combines Young's equation and the extended Fowkes' equation by including acid-base interactions is usually used.

$$\gamma_L(1+\cos\theta) = 2\left(\sqrt{\gamma_S^{LW}\gamma_L^{LW}} + \sqrt{\gamma_1^+\gamma_2^-} + \sqrt{\gamma_1^-\gamma_2^+}\right) \quad \text{(eq.2.7)}$$

where γ_L : the surface tension of the standard liquid , γ_1^+ : the dispersive part of the surface tension of the standard liquid, γ_1^- :the base part of the surface tension of the standard liquid, γ_S^{LW}: the dispersive part of the surface energy of the substrate, γ_2^+: the acid part of the surface energy of the substrate, γ_2^-:the base part of the surface energy of the substrate.

Three standard liquid which has two different acid and base part of surface tension, is required for the vOCG equation to calculate the surface energy of substrate by using contact angle measurement. The surface energy of a substrate can be divided into three parts (dispersive, acid, base). The dispersive part is related to characterize the non-specific (ex. Van der Waals) interactions. An acid and a base are included in polar part. The acid and base part mean the specific interactions such as dipole-dipole, induced dipole-hydrogen bonding between substrate and the standard liquids, which donate electron density and accept electron density, respectively.

In our experiments, the contact angles were measured at room temperature with a goniometer-camera-computer system (DM300, Kyowa corp) as shown in figure 2-12.

Figure 2-12. Surface energy measurement system.

2-2-7 Tg/DTA

The thermal analysis (TA) investigates the behavior of the material as a function of temperature. There are several types of TA techniques such as thermogravimetry (TG), differential thermal analysis (DTA) and dynamic mechanical analysis. There are advantages of TA technique [17].

- Measure with wide temperature spectrum using various temperature program
- Almost types of sample (solid, liquid or gel) can be investigated
- Needs small amount of sample (1 μg-10 mg)
- Flexible required time from several minutes to several hours
- Reasonably priced.

TG is the branch of TA which observe the change of mass as a function of temperature in the scanning mode or as a function of time in the isothermal mode. TG is used to investigate

the decomposition of materials with a variety of conditions such as atmosphere and temperature, and to observe the kinetics of the physicochemical processes.

TG/DTA equipment is consisted as shown in figure 2-13 and 2-14. It has two sample pans which are supported by a precision balance. One is filled with the solution sample and the reference material such as alumina is inserted into another pan. These pans in a furnace are heated by processed program with inert gas. Thermocouples measure the temperature difference between two pans during thermal process. The reference material shows a linear increase with programed temperature so the temperature difference is recorded during thermal process when there are abovementioned reactions. A DTA spectrum makes the plot as a function of time and temperature difference.

In my experiments, EXSTAR600 was used to interpret solution decomposition. The solutions were heated at a constant rate of 10 ºC/min in N_2 atmosphere where the flow rate of N_2 was 50 mL/min.

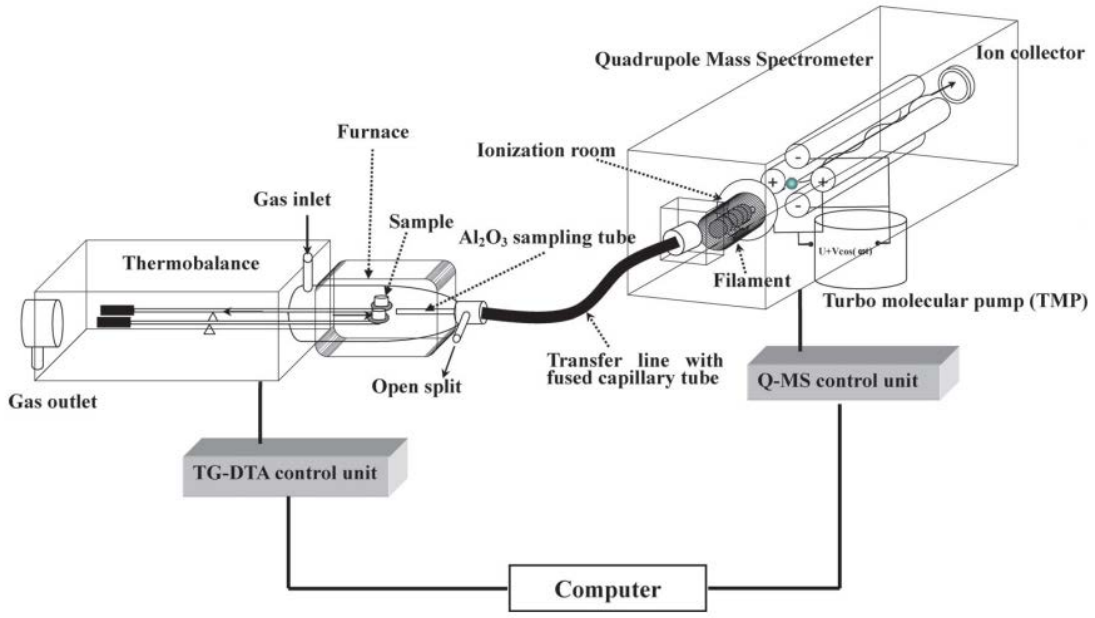

Figure 2-13.Schemtic diagram capillary type TG/DTA system

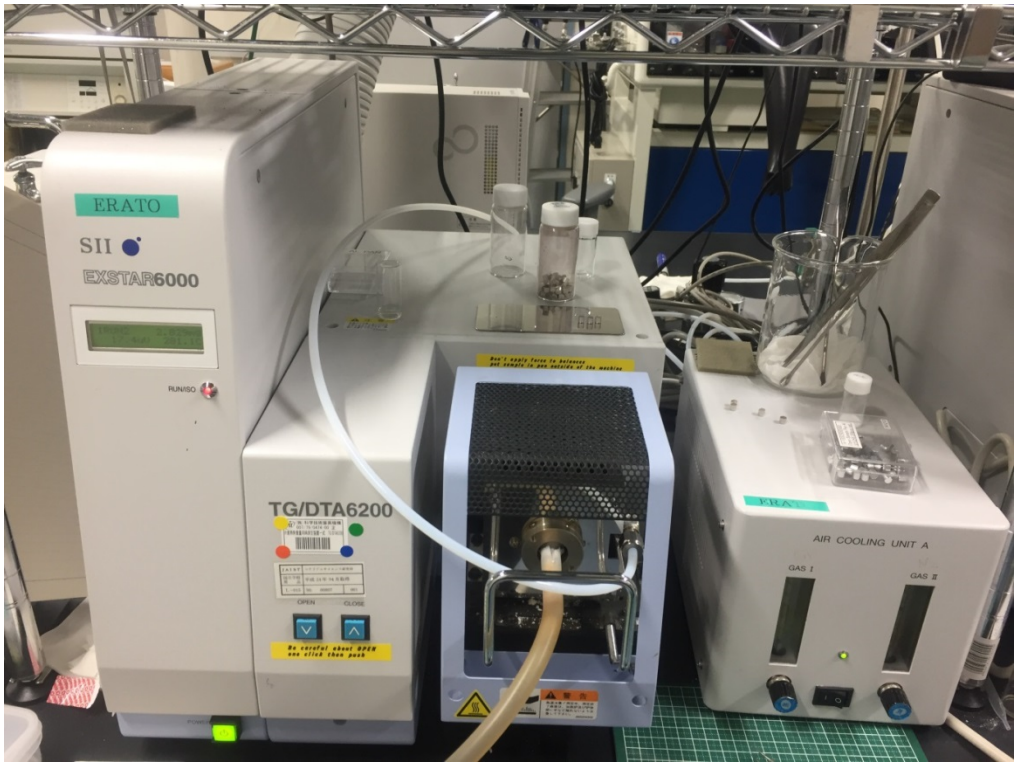

Figure 2-14. Picture of EXSTAR6000, Tg/DTA system

References

[1] H. Dislich, “New Routes to Multicomponent Oxide Glasses,” Angewandte Chemie International Edition, Vol. 10, pp. 383, 1971.

[2] K. S. Mazdiyasni, and L. M. Brown, “Synthesis and some properties of yttrium and lanthanide isopropoxides,” ibid, Vol. 55, pp.548, 1972.

[3] S. G. Porter, “Pyroelectric Detectors and Matenals,” Ferroelectrics, Vol. 33, pp. 193, 1981.

[4] H. Schmidt, “New Type of Non-Crystalline Solids Between Inorganic and Organic Materials ,” J. Non-Crystalline Solids, Vol. 73, pp. 681, 1985.

[5] D. Avnir, D. Levy, and R. Reisfeld, “The nature of the silica cage as reflected by spectral changes and enhanced photostability of trapped rhodamine 6G ,” J. Phys. Chem., Vol. 88, pp. 5956, 1984.

[6] D. C. Bradley, R. C. Mehrotra, and D. P. Gaur, “Metal alkoxides,” Academic press, New York, 1978.

[7] C. Sanchez, J. Livage, M. Henry, and F. Babonneau, “CHEMICAL MODIFICATION OF ALKOXIDE PRECURSORS,” J. Non-crystalline solids, Vol. 100, pp. 65, 1998.

[8] C J Lawrence and W Zhou Journal of Non-Newtonian Fluid Mechanics 39 137 (1991)

[9] Niranjan Sahu, B Parija and S Panigrahi, “Fundamental understanding and modeling of spin coating”, Indian Journal of Physics, vol.83, pp.493, 2009.

[10] C. J. Kim, D. S. Yoon, J. S. Lee, W. J. Lee, and L. No, “Electrical characteristics of (100), (111) and randomly aligned lead zirconate titanate thin films,” J. Appl. Phys., Vol. 76, pp. 7478, 1994.

[11] S. Levichev, A. Chahboun, P. Basa, A.G. Rolo, N.P. Barradas, E. Alves, Zs. J. Horvath, O. Conde, M.J.M. Gomes, ”Charging effects in CdSe nanocrystals embedded in SiO_2 matrix produced by RF magnetron sputtering”, Microelectronic Engineering, vol.85, pp.2374, 2008.

[12] Gurvinder Singh Bumbrah, Rakesh Mohan Sharma, “Raman spectroscopy-Basic principle, instrumentation and selected applications for the characterization of drugs of abuse”, Egyptian Journal of Forensic Sciences, vol.6, pp.209, 2016.

[13] John F.Watts, John Wolstenholme,”An Introduction to Surface Analysis by XPS and AES”, Wiley, 2003.

[14] U. Hartmann, “An Elementary Introduction to Atomic Firce Microscopy and Related Methods”, technical note, Institute of Experimental Physics, Unicersity of Saarbrucken, Germany, 1997.

[15] J. B. Warren and B. J. Panessa-Warren, “A Comparison of Nanometrology Using TEM and SEM”, Microsc Microanal, vol.11, pp.1932, 2005.

[16] Finn Knut Hansen, “The Measurement of Surface Energy of Polymers by Means of Contact Angles of Liquids on Solid Surfaces”, Surface energy of Polymers, p.1, 2004.

[17] T. Hatakeyama and F.X. Quinn, “Thermal Analysis Fundamentals and Applications to Polymer Science”, Wiley, 1999.

3. Fabrication and characterization of high-k gate dielectric film

3-1 Introduction

The physical thickness of gate insulator of Si-MOSFETs is rapidly decreasing. When SiO_2 thickness becomes less than 2-3 nm, the gate leakage current becomes high due to the direct tunnelling. Hence, to overcome the difficulty, there have been amount of researches for new materials which have higher dielectric constant than SiO_2. The requirements of a new oxide are summarized by five cases [1].

1. High enough dielectric constant
2. Thermodynamically stable with Si due to directly contact with the Si
3. Act as an insulator
4. Good electrical interface with Si
5. Few bulk electrically active defects

In figure 3-1, elements in white cells satisfy the requirements for the gate oxide material. Elements in the blue cells were ruled out due to various reasons such as not a solid at 1000 K, radioactive and reaction with Si. Among white space one, high-permittivity (high-k) dielectrics such as ZrO_2, HfO_2, La_2O_3, Ta_2O_5, TiO_2 have been extensively researched [2]. The

Ta_2O_5, TiO_2 cannot be used because it is reactive with Si. The La_2O_3 can be changed to La(OH) easily by reaction with water from air so it also did not apply to device.

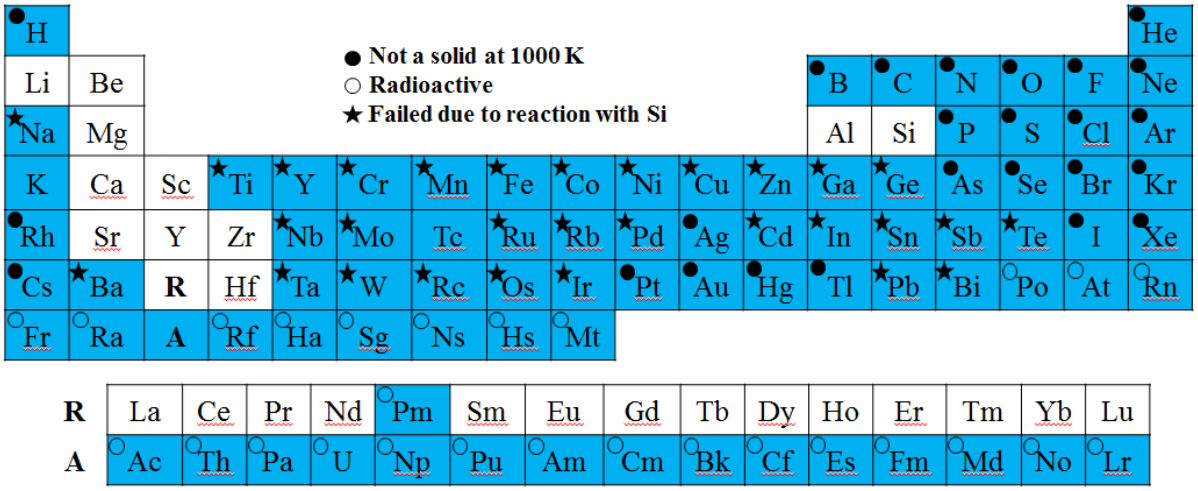

Figure 3-1. Periodic table indicates what the metal oxide has possibility to be used as a gate insulator.

The ZrO_2 and Al or Si doped ZrO_2 films are of the greatest industrial interest for current and near future generation technology nodes [3-4]. The dielectric constant of ZrO_2 thin films depends strongly on their phase and crystallinity, which can be regulated via control of the growth temperature and film thickness. A ZrO_2 has three crystalline structures: monoclinic (m-ZrO_2), tetragonal (t-ZrO_2) and cubic (c-ZrO_2) as shown in figure 3-2. A ZrO_2 has three crystalline structures at atmospheric pressure and its most stable phase depends on the temperature; cubic over 2400 °C, tetragonal over 1200 °C and monoclinic under 1200 °C [5]. The dielectric constant of each phases is different (monoclinic: 20, tetragonal: 35~40, cubic: 45) due to the increase of symmetry rate of oxygen and zirconium. In detail, the large dielectric constants arise from enhanced symmetry of polarity, and Born effective charges from hybridization of oxygen atom [6]. The highest dielectric constant of 46 has been

predicted for bulk ZrO_2 crystallized with tetragonal phase. However, to obtain a t-ZrO_2, annealing temperature over 1170 ºC is needed. To stabilize the tetragonal phase of ZrO_2 at lower temperature, many kinds of dopants such as aliovalent (Y^{3+}, Ca^{2+}) and tetravalent (Si^{4+}, Ce^{4+}, Ge^{4+}) elements have been investigated [7-11]. However, there are only a few reports about the stabilizing effect of pentavalent ions such as Nb^{5+} and Ta^{5+} for ZrO_2 because the size and the charge are thought to be unfavourable to stabilize metastable ZrO_2 in point of traditional view [12]. In addition, there are few studies about the electrical properties of Nb doped ZrO_2 thin film on Si substrate.

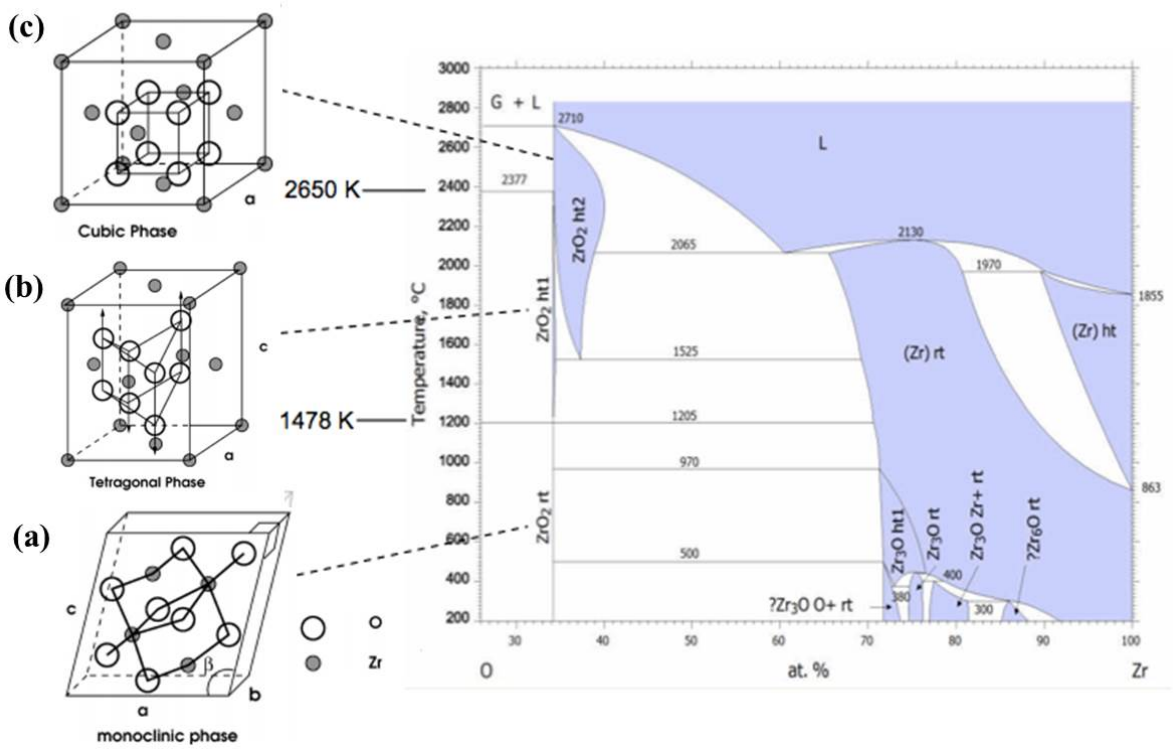

Figure 3-2. Crystalline structures of ZrO_2 in O-Zr phase diagram at (a) room temperature (rt) for monoclinic, (b) high temperature for tetragonal (ht1) and (c) high temperature for cubic.

In my work, we have investigated crystallographic and electrical properties of the Nb doped ZrO_2 (NZO) thin film deposited on Si substrate by the sol-gel method. It was found that sol-gel derived Nb-doped ZrO_2 film showed tetragonal phase even at relatively low annealing temperature, resulting in high dielectric constant.

3-2 Fabrication procedure

The NZO film was deposited on the highly doped silicon substrate to make the metal-insulator-semiconductor (MIS) structure. Figure 3-3 (a) shows the process diagram for the NZO precursor solution. The starting materials for Nb and Zr were niobium 2-ethylhexanoate (NEH: $Nb(O_2C_2H(C_2H_5)C_4H_9)_4$) and zirconium acetylacetonate (Zr(acac) : $C_{20}H_{28}O_8Zr$), respectively. The Zr(acac) was dissolved in the propionic acid in advance. Then, the NEH was inserted into the solution to adjust the desired mol ratio. The mol ratio of Nb was varied from 2 mol% to 50 mol% to optimize a condition. Then, the Nb-Zr precursor was stirred for two hours at 800 rpm on a hot plate at 130 ºC.

Prior to the deposition process, n-type Si(100) substrate was cleaned with acetone, methanol and de-ionized water after dipping into HF solution to remove the native silicon oxide layer. Then, Nb-Zr precursor solution was spin-coated on Si substrate at 500 rpm for 5 seconds then, at 3000 rpm for 20 seconds. The coated film was baked at 250 ºC for 5 minutes on a hot plate in an atmosphere. Next, baked NZO films were annealed at 400 ºC for 5 min then, annealed again at 500~1000 ºC for 20 minutes in air (N_2:O_2=3:1) by rapid thermal annealing (RTA) system as shown in figure 3-3(b). Finally, the gold was evaporated to form top and bottom electrodes for electrical measurements.

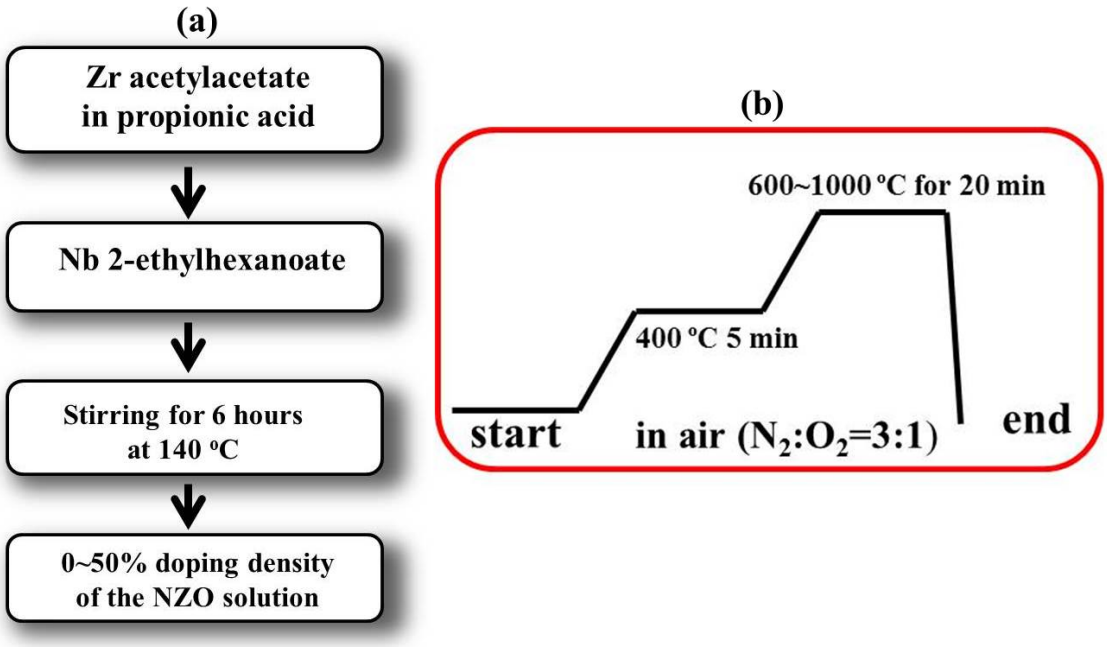

Figure 3-3. Diagram of (a) solution produce and (b) annealing process for NZO film.

The crystalline phase of the NZO films on Si substrate was characterized by X-ray diffraction (XRD) analysis, transmission electron microscopy (TEM) and X-ray photoelectron spectroscopy (XPS). The XPS was conducted using an AXIS ULTRA with a monochromatic Al Kα (1486.7 eV) X-ray source. The TEM was performed using JEM-ARM200F with acceleration energy of 200 keV. The GI-XRD was analyzed using X`PERT PRO with a monochromatic Cu Kα (1.542 Å) X-ray source. The surface morphology was observed by atomic force microscope (AFM) using SII AFM5200S. The capacitance-voltage (C-V) using Toyo technology system and the current density-voltage (J-V) measurements using Agilent 4155C were carried out to characterize the electrical properties.

3-3 Results and discussion

From the cross section TEM image shown in figure 3-4(a), the thickness of NZO film fabricated with an annealing temperature of 800 ºC was found to be about 10 nm. The 3 nm of SiO_2 interfacial layer was formed between NZO film and Si substrate because of high temperature annealing in air. Although the annealing time was only 20 minutes, it was found that the NZO film was crystallized and there were several large domain regions, which indicated the film had a polycrystalline structure.

Energy dispersive X-ray spectrometry (EDS) produces the X-Ray spectrum using emitted electrons by inducing high energy on the sample to investigate a localized chemical elements. The EDS mapping for Nb and Zr atom distribution within the thin film are shown in figure 3-4(b) and (c). It was found that Nb was doped in the ZrO_2 film uniformly and no significant diffusion of Zr and Nb into SiO_2/Si substrates was observed.

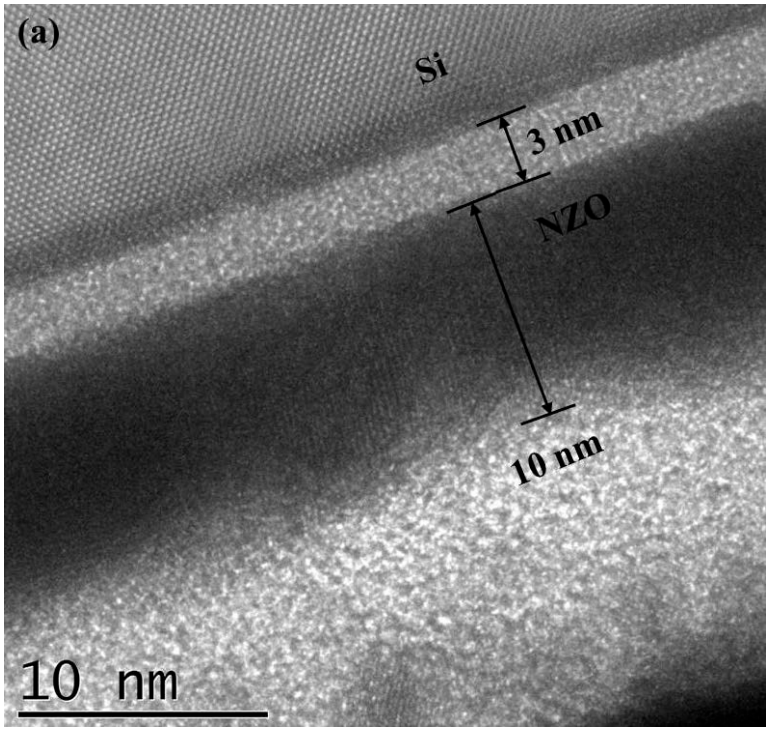

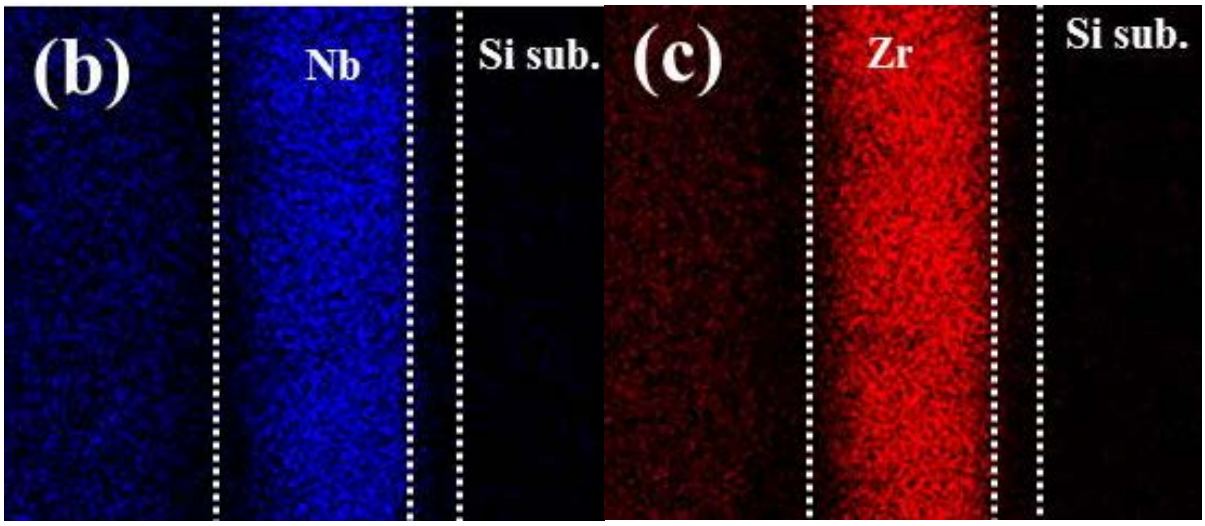

Figure 3-4. (a) TEM cross section, EDS image of (b) Nb atom, and (c) Zr atom for NZO film fabricated by sol-gel technique on Si substrate with an annealing temperature of 800 ºC.

In this experiments, the source solution with a composition of 30% were prepared. To compare components proportion change between solution and deposited film, the EDS spectra was measured. The peak of Zr-Kα and Nb-Kα is positioned at 15.74 eV and 16.58 eV respectively as shown in figure 3-5. The calculated atom percent of Zr and Nb was 67.4 % and 32.6 %, respectively. The deposited film shows almost same components proportion with the precursor solution.

Figure 3-6 shows the grazing incidence X-ray diffraction (GI-XRD) patterns for NZO films with various Nb compositions from 0 to 50 %. All NZO films were annealed at 800 ºC, because pure ZrO_2 showed highest accumulated capacitance when it was annealed at 800 ºC as shown in figure 3-11(b). It was reported that a sol-gel derived ZrO_2 film forms a metastable tetragonal phase due to the thermal decomposition of zirconium salts, alkoxides and hydroxide [13]. In our experiments, the spin-coated ZrO_2 film also showed both m-ZrO_2 peaks at 28.5 ° and t-ZrO_2 peaks at 30.6 °, 51.2 ° and 60.5 ° as shown in figure 3-6.

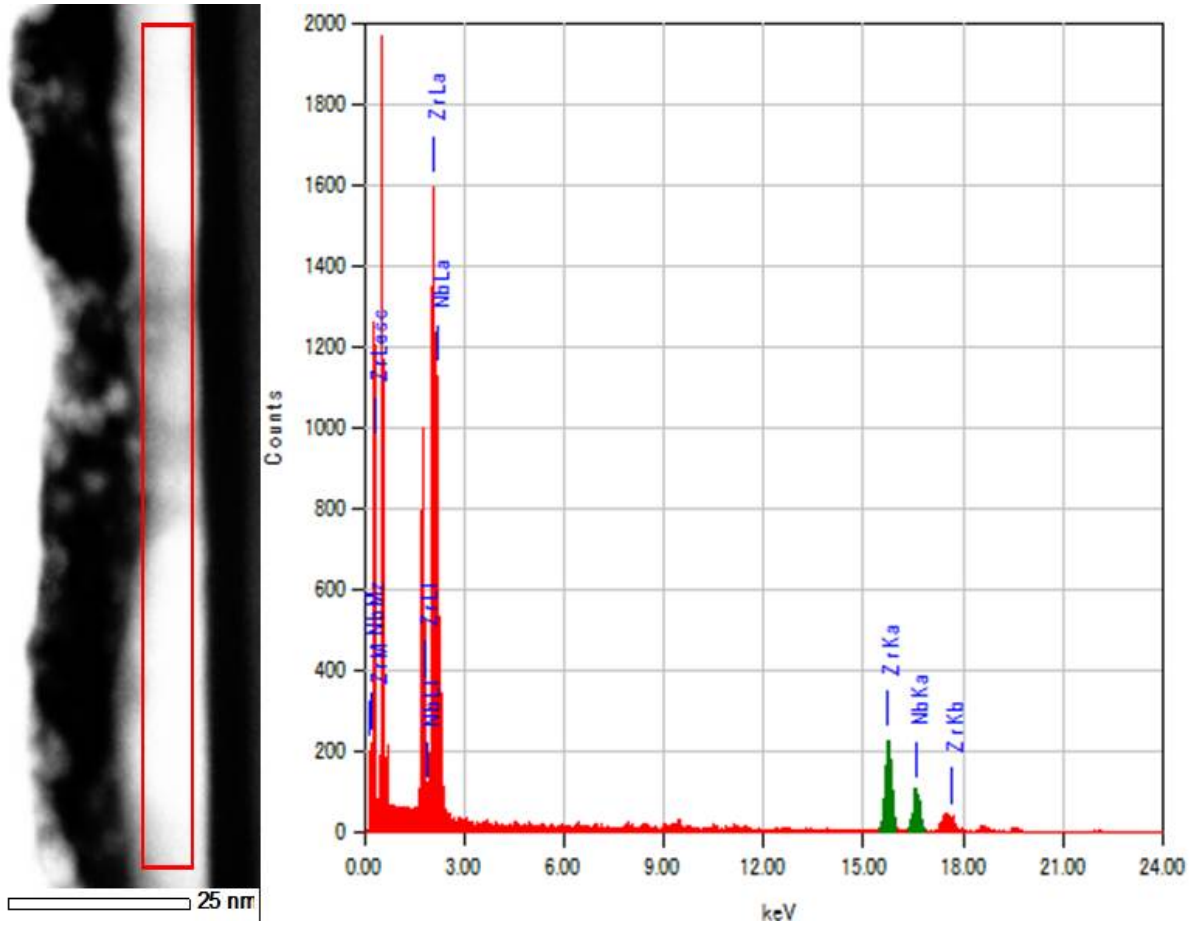

Figure 3-5. EDS spectra revealing the % compositions of Nb and Zr elements.

On the other hand, the XRD peaks due to t-ZrO_2 were observed as shown in figure 3-6 for the sol-gel derived NZO films with Nb compositions of less than 30%. It should be noted that the Nb doped films showed only a tetragonal phase. When the Nb composition is more than 40%, the t-ZrO_2 peak intensities decrease and diffraction peaks from niobium pentoxide (Nb_2O_5) at 53.7º and 55.4º start to appear. Hence, it can be concluded that NZO films fabricated by the sol-gel technique exhibit tetragonal ZrO_2 phase when the Nb composition is less than 30%, and that further doping of Nb does not enhance the growth of the tetragonal phase.

The capacitance-voltage (C-V) characteristics of the MIS structure with pure ZrO_2 and 30% Nb-doped ZrO_2 (NZO-30) are shown in figure 3-7(a). The accumulation capacitance of the MIS structure with NZO-30 film is much larger than that of the MIS structure with pure ZrO_2 film. This suggests the dielectric constant of the NZO-30 is larger than that of pure ZrO_2. In addition, the threshold voltage shift and hysteresis of C-V curve of the MIS structure with NZO-30 film are smaller than those of the MIS structure with pure ZrO_2 film.

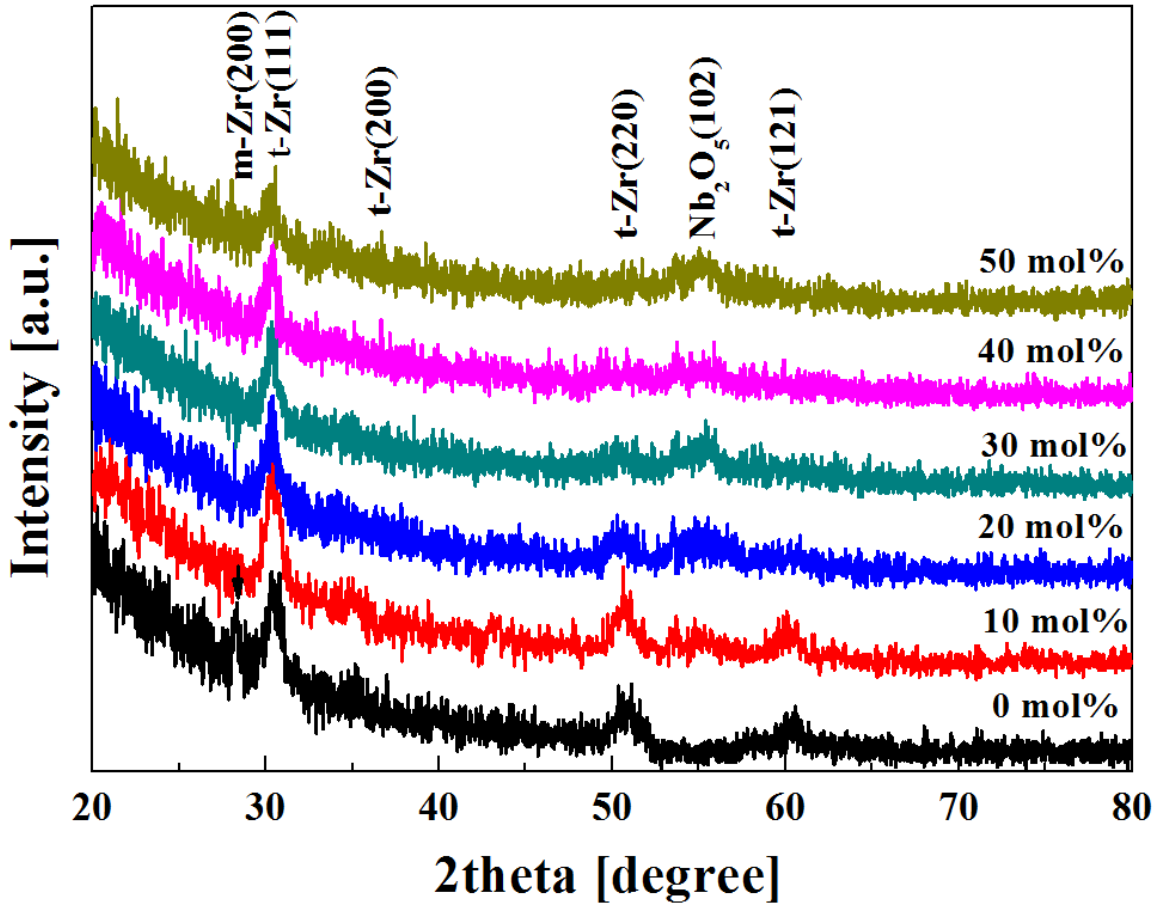

Figure 3-6. GI-XRD spectra of Nb 0 ~ 50 mol% doped ZrO_2, annealed at 800 ºC.

The accumulation capacitances deduced from the C-V curves of the NZO-30 MIS structures with various Nb mol ratios were plotted in figure 3-7(b) as a function of Nb doping

density. It was found that the accumulation capacitance increased with Nb doping density until the largest capacitance of 0.83 μF/cm^2 for the NZO-30 film with Nb composition of 30 mol%. However, the accumulation capacitance decreased when the doping density was more than 30 mol%. The relative dielectric constant of NZO-30 film was estimated to be approximately 40 by taking the capacitance of SiO_2 interfacial layer into account. On the other hand, the relative dielectric constant of pure ZrO_2 fabricated in this work was 20, which reasonably agrees with a reported values for monoclinic ZrO_2 [14]. It is worth noting that the dielectric constant is increased by Nb doping and reaches the maximum value at Nb mol ratio of 30%. This may correlate with the XRD data, which suggests that the formation of the tetragonal phase is limited when the Nb content is more than 40%.

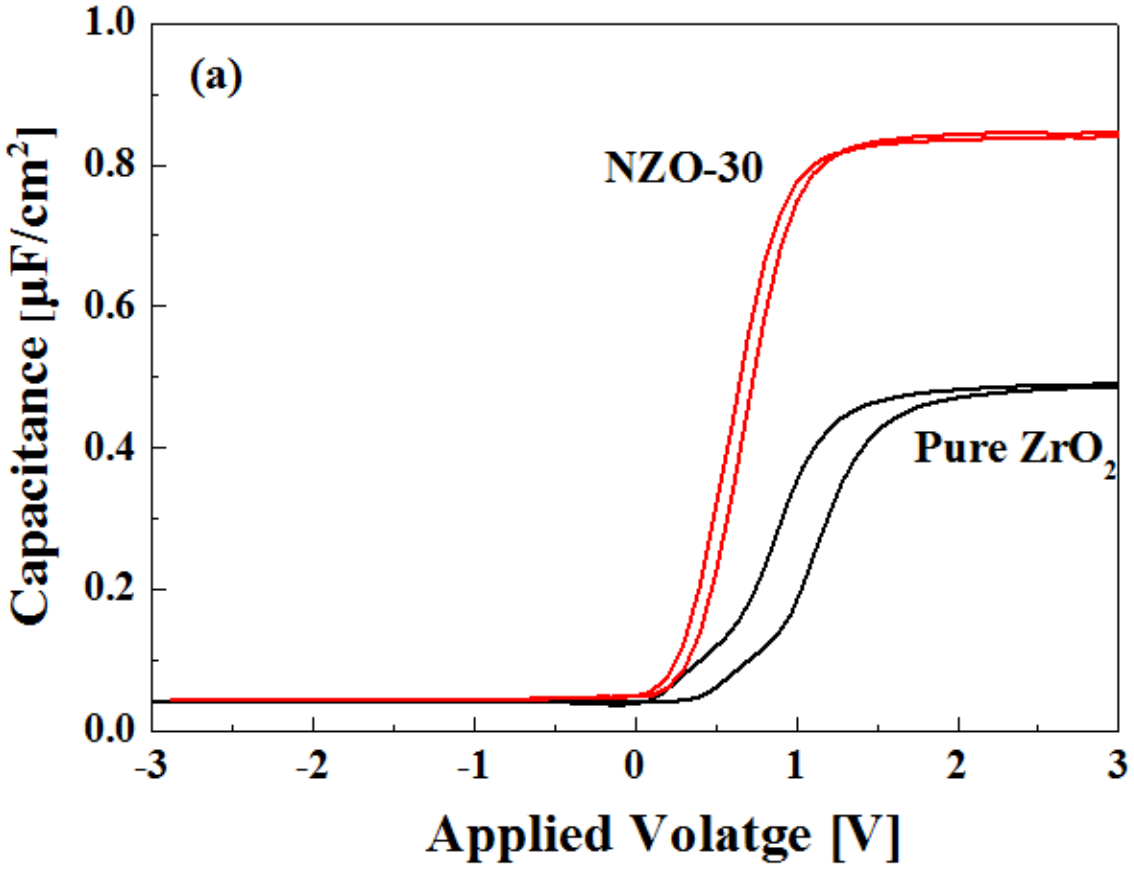

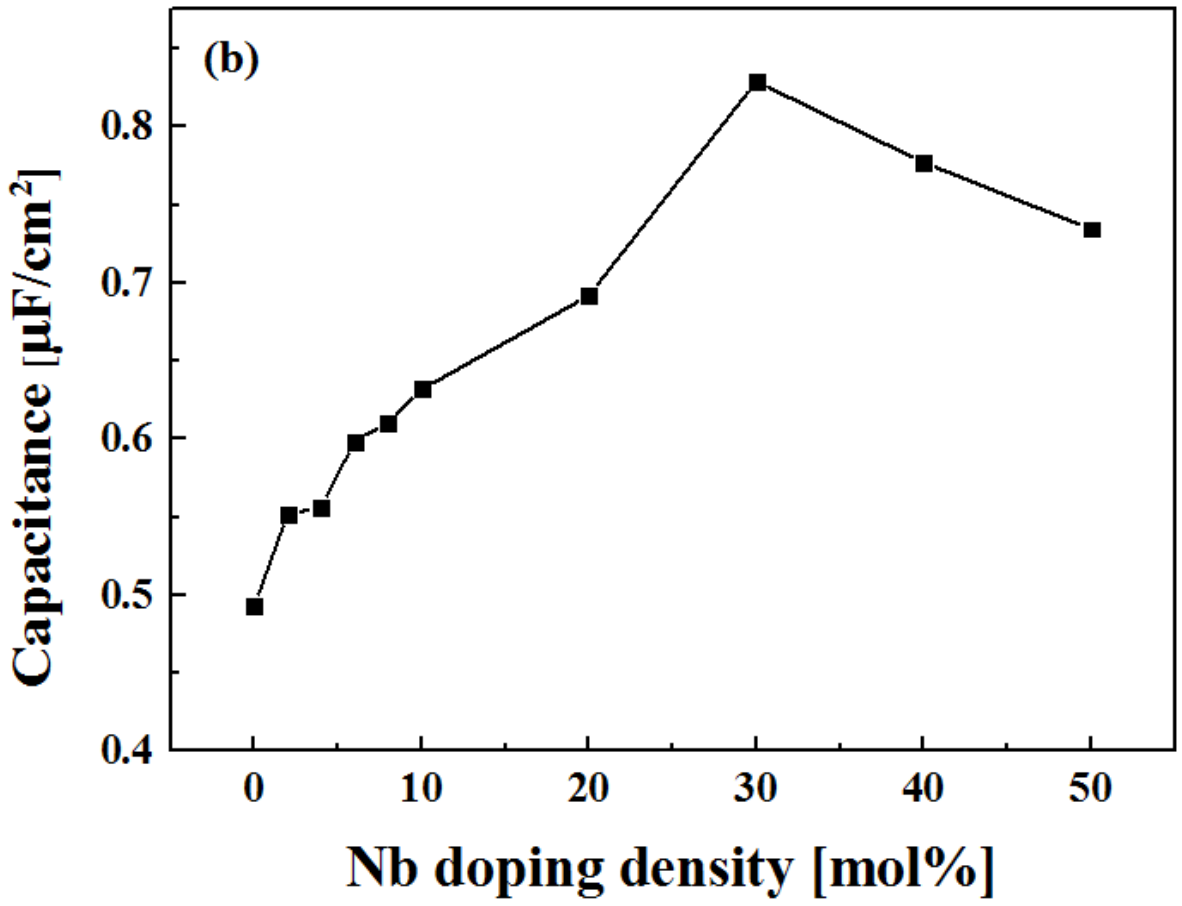

Figure 3-7. (a) Capacitance-voltage (C-V) curves of MIS structures with pure ZrO_2 and Nb (30%) doped ZrO_2 annealed at 800 °C and (b) accumulation capacitance of the NZO MIS structures as a function of Nb doping density.

Surface flatness is one of the important factors that affect the operation of microelectronic devices [15]. The surface morphology of NZO-30 annealed at 800 °C for 20 min, as shown in figure 3-7. The scan size is 10 x 10 μm and speed was 10 Hz. The root mean square roughness was 1.02 nm. This value is comparable with pure and yttrium doped ZrO_2 [16] even though the NZO film is crystallized. However, it was observed that if the film was annealed for a longer time (~1.5 h) or higher temperature (1000°C), the mean square

roughness increased to 7~8 nm. Hence, the optimization of annealing conditions is important for practical device applications.

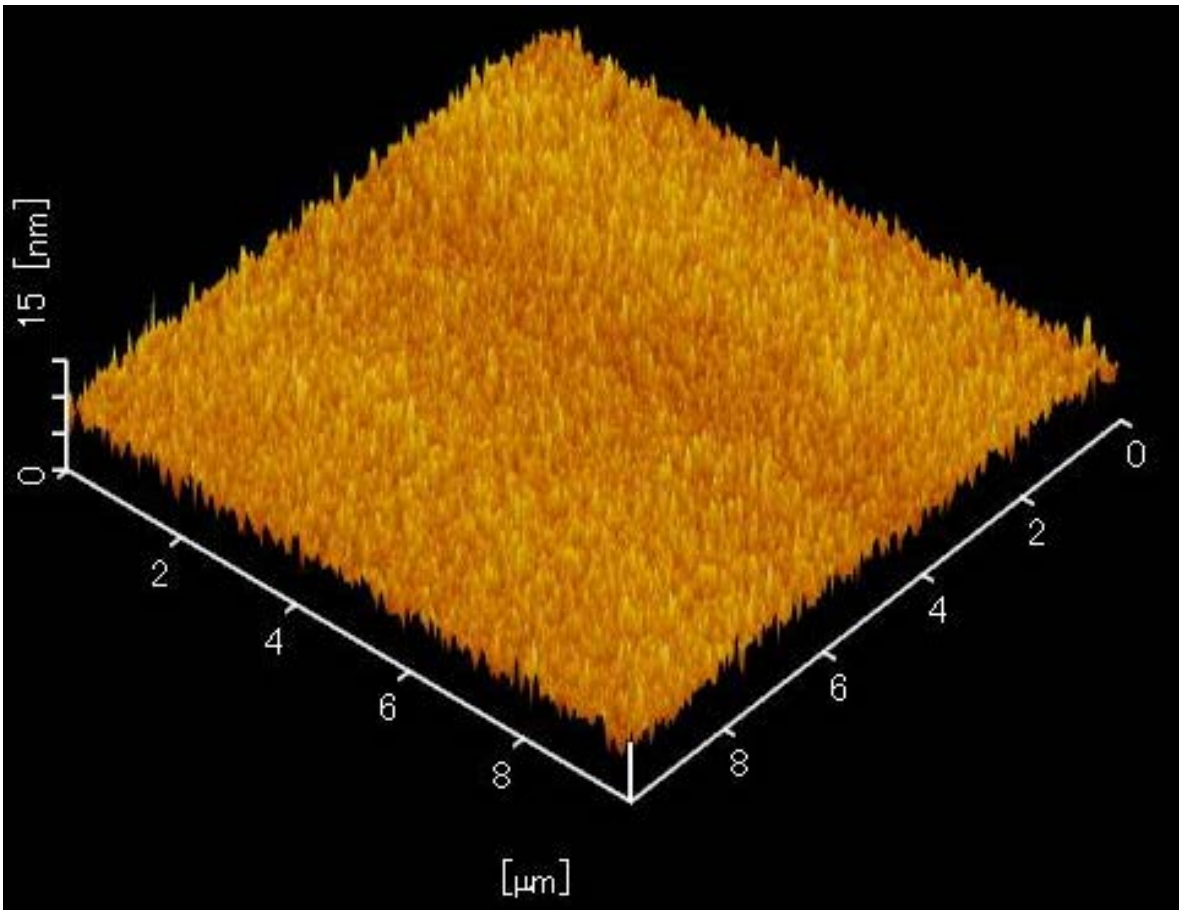

Figure 3-8. AFM image of Nb 30 mol% ZrO_2 film.

In my experiments, it needs 1000 °C for high crystallized MoS_2. Figure 3-9 shows the surface morphology alternation of NZO-30 film annealed at 1000 °C with variation thermal treatment time. The roughness of NZO-30 film annealed for 5, 15, 30, 60 min were 1.8, 3.3, 4.8 and 6.9 nm.

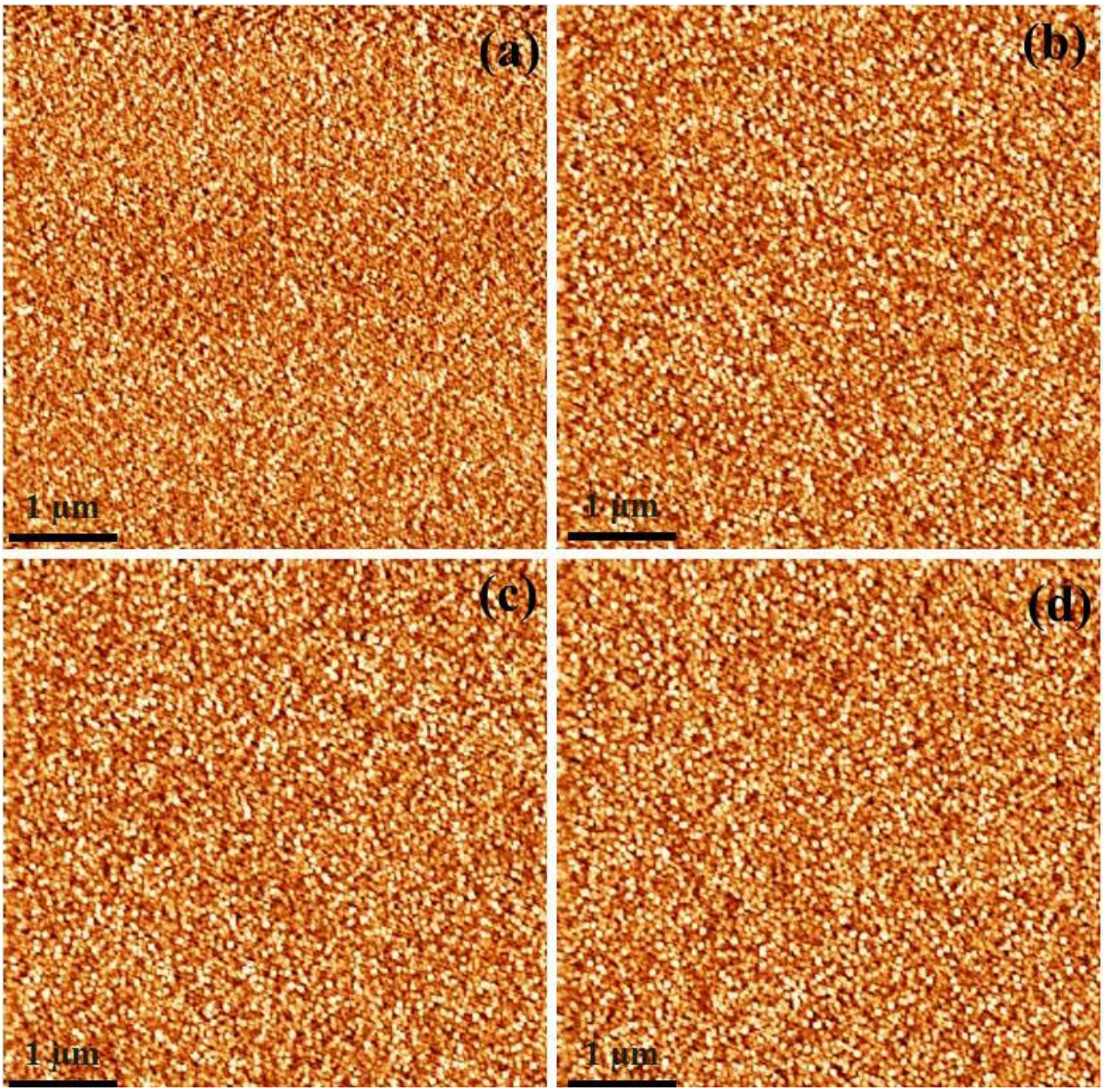

Figure 3-9 AFM images of NZO-30 annealed at 1000 °C for (a) 5 min, (b) 15 min, (c) 30 min and (d) one hour.

Figure 3-10 shows the XPS data of NZO-30 for (a) Nb 3d, (b) Zr 3d, (c) O 1s states and (d) ZrO_2 for O 1s with calibrating of carbon (C) 1s peak at 284.8 eV. XPS spectrum for O 1s of pure ZrO_2 is also shown in figure 3-10 (d) for comparison. All graphs were fitted using Gaussian function. It is known that Nb oxides has three phases; Nb_2O_5, NbO_2 and NbO [17].

If Nb atom is substituted with Zr site, it could be form Nb^{4+} for NbO_2. From figure 3-10(a), there are not Nb_2O_5 related peaks at 205.9 eV and 208.7 eV, but Nb_2O_5 related peaks at 207.5 eV and 210.2 eV, which indicate that only Nb^{5+} is observed. This agrees with previous researches [18, 19] that the stable ion state of Nb in ZrO_2 is 5+. The well-known ZrO_2 peaks were observed at 186.0 eV and 183.5 eV for NZO-30 film as shown in figure 3-10(b). The O 1s peaks of NZO-30 and pure ZrO_2 are divided by Gaussian function as shown in figures 3-10 (c) and (d). The O 1s peak of pure ZrO_2 can be divided into four peaks, which suggests the solution processed ZrO_2 has the several absorbed species such as water to form the hydroxide (Zr-O-H at 531.2 eV) and carbon to form the metal carbonate (Zr-C-O at 532 ~ 533 eV) as shown in figure 3-10(d). These bonds are induced to the oxygen vacancy and surface defects [20]. On the other hand, the XPS peak of NZO-30 can be divided into three peaks. It shows no hydroxide bond and it has relatively small peaks for metal carbonate as shown in figure 3-10(c). These results suggest the absorption of undesired species could be suppressed by Nb doping. This may be one of the reasons why the C-V curve of the MIS structure with NZO-30 film shows small hysteresis and threshold voltage shift as shown in figure 3-7(a).

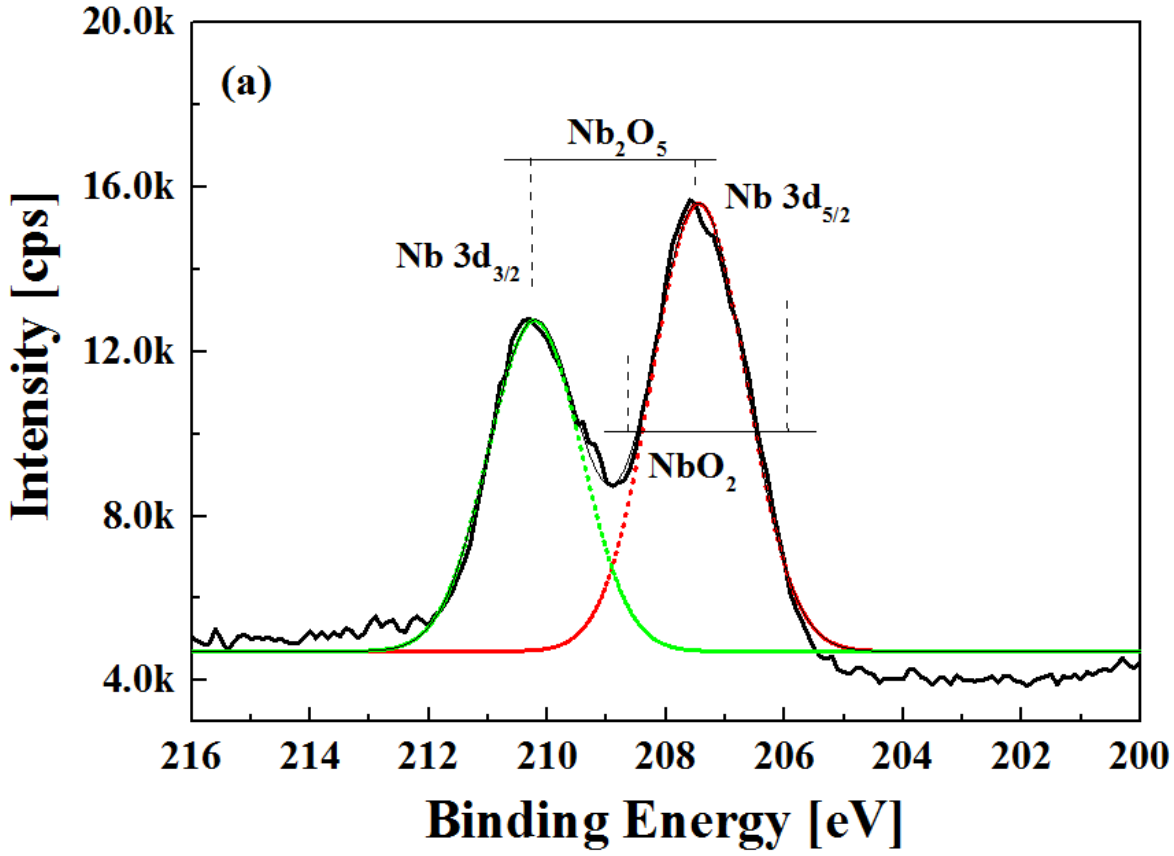
(a)
Nb2O5
Nb 3d5/2
Nb 3d3/2
NbO2
Intensity [cps]
Binding Energy [eV]
20.0k
16.0k
12.0k
8.0k
4.0k
216
214
212
210
208
206
204
202
200

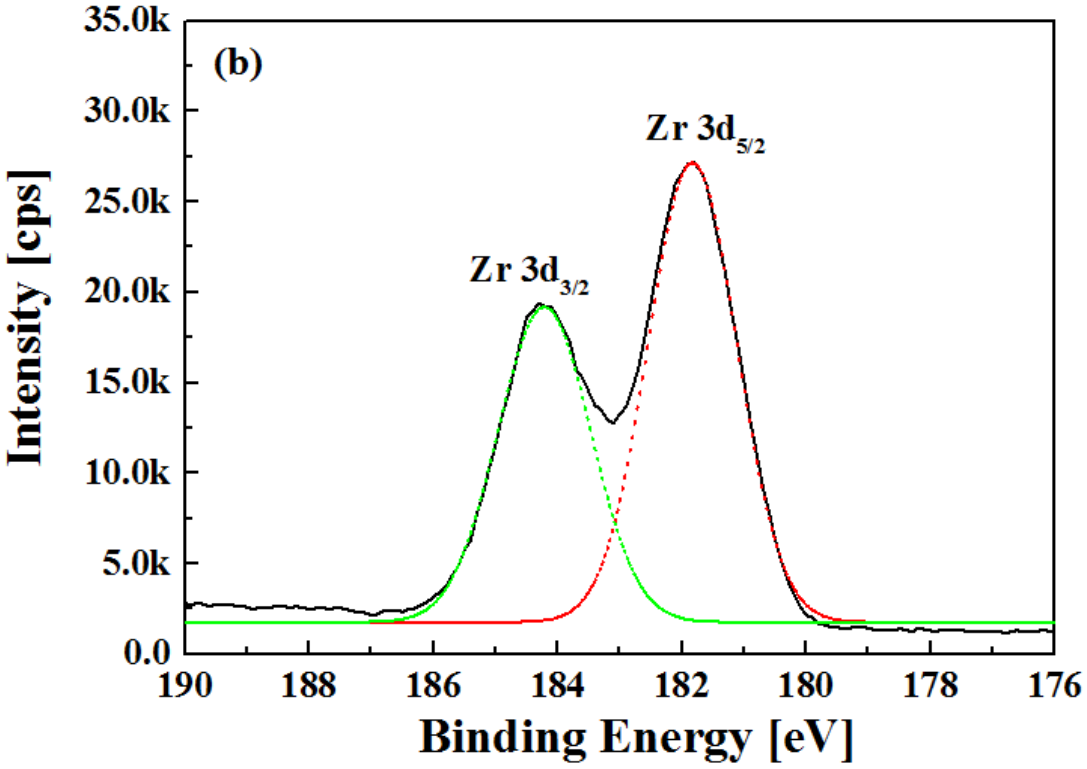
(b)
Zr 3d5/2
Zr 3d3/2
Intensity [cps]
Binding Energy [eV]
35.0k
30.0k
25.0k
20.0k
15.0k
10.0k
5.0k
0.0
190
188
186
184
182
180
178
176

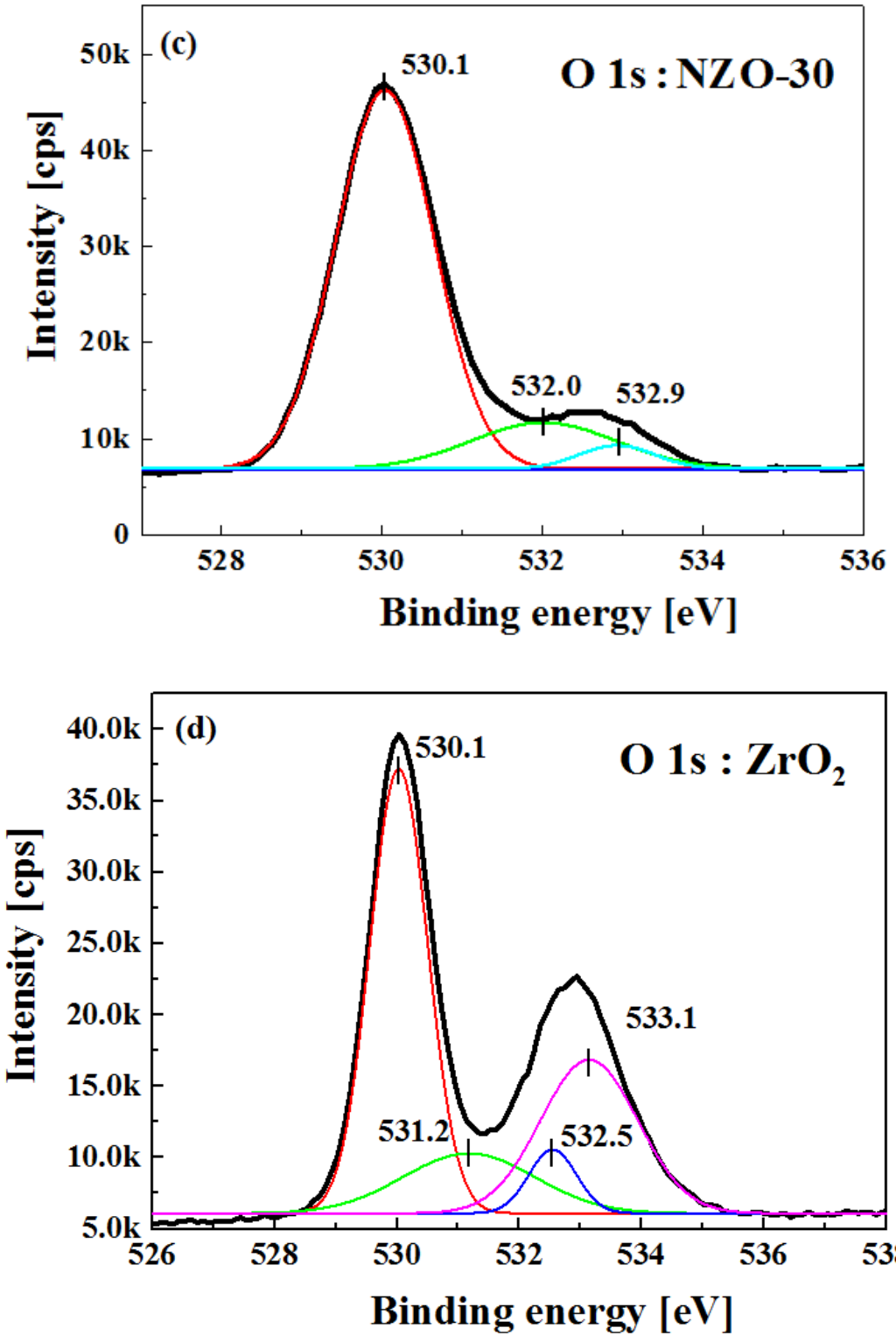

Figure 3-10. XPS spectra for (a) Nb 3d, (b) Zr 3d, (c) O 1s of NZO-30 and (d) O 1s of ZrO_2.

We next examined annealing temperature dependence on crystallinity and electrical properties of NZO film with a fixed Nb content of 30%. The XRD analysis (figure 3-11) showed that when the annealing temperature was more than 700 ºC, clear diffraction peaks from the tetragonal phase were observed. As the annealing temperature was increased, the peak intensity of the tetragonal phase increased.

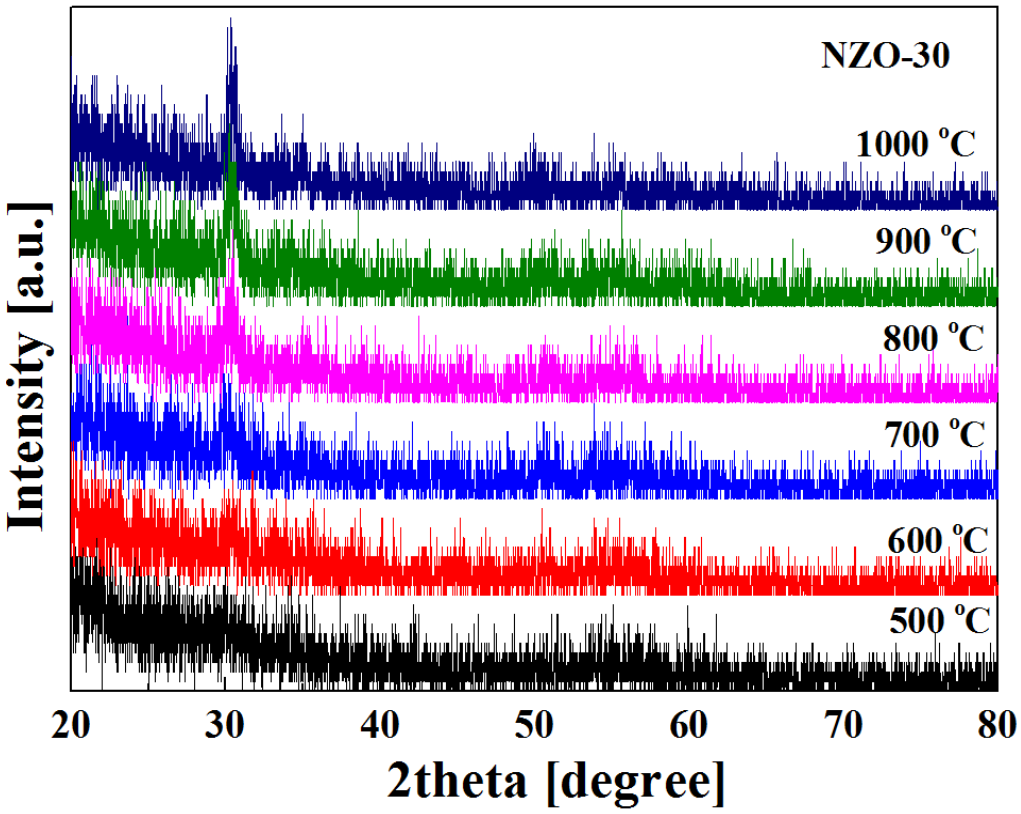

Figure 3-11. GI-XRD for NZO with variation temperature from 500 ~ 1000 °C.

Figure 3-12 shows the C-V characteristics of the MIS structure where NZO film with Nb30% was used. The annealing temperature was varied from 500 to 800 ºC. When the annealing temperature was below 500 ºC, the C-V curve for MIS structure with NZO film showed hysteresis with a low accumulation capacitance because the crystallization of the

NZO film was not enough. When the annealing temperature is over 800 ºC, the accumulation capacitance starts to decrease because the thickness of the SiO_2 interfacial layer between NZO and Si substrate was increased due to the high temperature annealing which enhances unintentional oxidation of Si substrate. From the film thickness of NZO and SiO_2 as shown in figure 3-4, the calculated dielectric constant of NZO film with 30 mol% Nb was about 40. This value is comparable with the value for a tetragonal ZrO_2.

Figure 3-13 shows the leak current density of NZO film with a Nb composition of 30 mol%, annealed at 800 ºC. There are linear and non-linear regions because of mixing the current mechanism such as Schottky, Poole- Frenkel, and Fowler Nordheim tunneling [21]. Chang and Lin have reported that the dominated conduction mechanism of ZrO_2 films prepared by the chemical vapor deposition method is due to Pool Frenkel conduction [22].

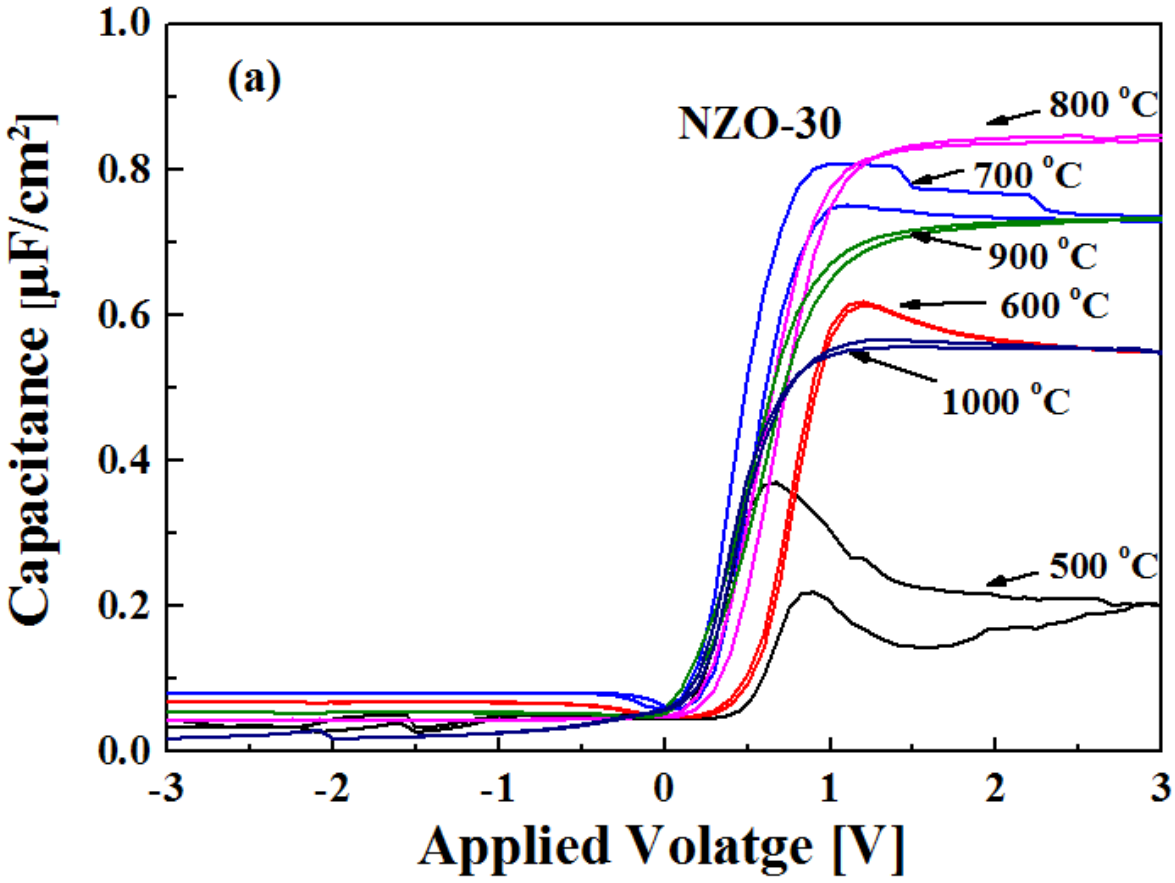

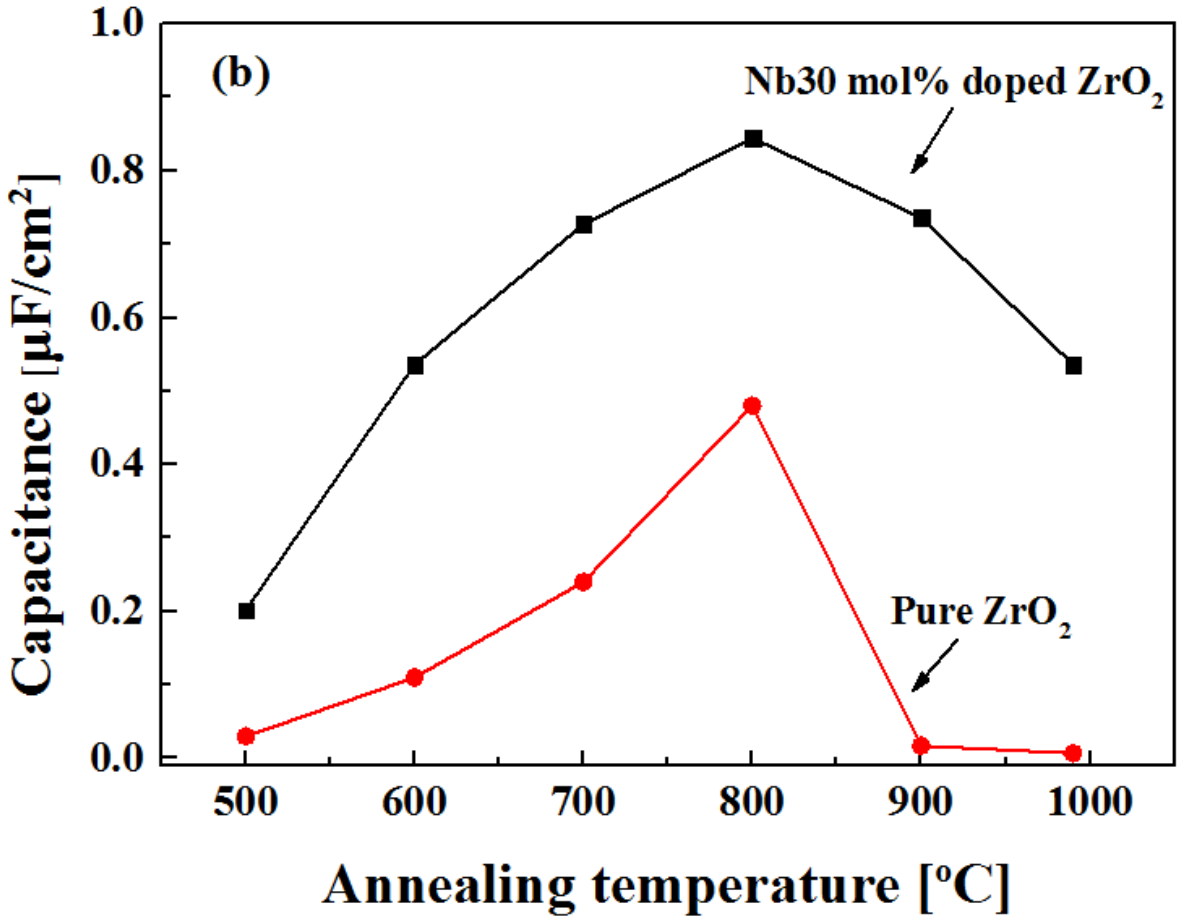

Figure 3-12. (a) Annealing temperature dependence of C-V curves for Nb 30 mol% ZrO_2 film and (b) accumulation capacitance of the MIS structures with pure ZrO_2 and Nb 30 mol% ZrO_2 films.

The NZO film with the Nb composition of 30 mol% fabricated in this work has 10^{-6} A/cm^2 under 4.4 V. The current graph is redrawn with log (J)-$E^{1/2}$ scale as shown in the inset of figure 3-13. It was found under electric field of 1.7 MV/cm, the current mechanism is Pool Frenkel conduction as Chang and Lin reported. In addition, Fowler Nordheim tunneling was observed over 1.8 MV/cm.

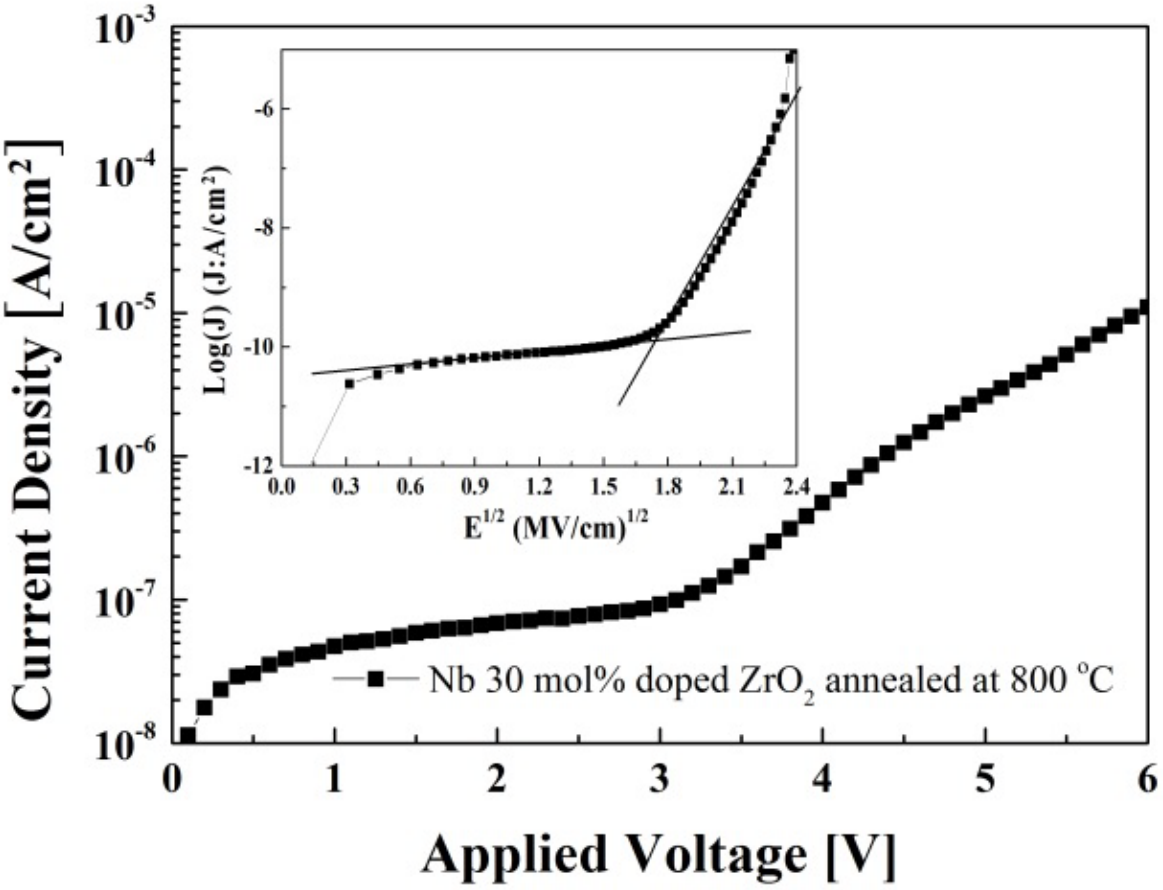

Figure 3-13. The leakage current density of NZO-30 annealed at 800 ºC.

3-4 Summary

In this work, the crystalline structure and electrical properties of NZO films spin-coated on Si substrate were studied. The sol-gel derived NZO thin film exhibited polycrystalline structure, when the film was annealed at more than 700 ºC. It is found that the Nb doping is helpful to stabilize the tetragonal ZrO_2 but it is also found that high Nb doping density (over 40 mol%) interferes with the formation of tetragonal ZrO_2 phase. In our experiments, a large relative dielectric constant of 40 was obtained for the NZO film with a Nb doping

density of 30 mol% when the annealing temperature was 800 ºC. The MIS structure with NZO film shows a reasonably low leakage current of 10^{-6} A/cm^2 at 4.4 V. From these results, it can be concluded that Nb could be a promising dopant for stabilized t-ZrO_2 which has good electrical properties for capacitor applications.

References

[1] J. Robertson, “High dielectric constant oxides”, European Physical Journal Applied Physics, vol.26, pp.265, 2004.

[2] Dayu Zhou, U. Schroeder, Jin Xu, J. Heitmann1, G. Jegert, W. Weinreich, M. Kerber, S. Knebel1, E. Erben and T. Mikolajick, “Reliability of Al_2O_3-doped ZrO_2 high-k dielectrics in three dimensional stacked metal insulator metal capacitors”, Journal of Applied Physics, vol. 108, pp.124104, 2010.

[3] Deok-Sin Kil, Han-Sang Song, Kee-Jeung Lee, Kwon Hong, Jin-Hyock Kim, Ki-Seon Park, Seung-Jin.Yeom, Jae-Sung Roh, Noh-Jung Kwak, Hyun-Chul Sohn, Jin-Woong Kim, and Sung-Wook Park, “Development of New TiN/ZrO_2/Al_2O_3/ZrO_2/TiN Capacitors Extendable to 45 nm Generation DRAMs Replacing HfO_2 Based Dielectrics”, 2006 Symposium on VLSI Technology, pp.38, 2006.

[4] Ho Jin Cho, Young Dae Kim, Dong Su Park, Euna Lee, Cheol Hwan Park, Jun Soo Jang, Keum Bum Lee, Hai Won Kim, Young Jong Ki, Il Keun Han, Yong Wook Song, “New TIT capacitor with ZrO_2/Al_2O_3/ZrO_2 dielectrics for 60 nm and below DRAMs” Solid-State Electron, vol.51, pp.1529, 2007.

[5] Richard H. J. Hannink, Patrick M. Kelly and Barry C. Muddle, “Transformation Toughening in Zirconia-Containing Ceramics” Journal of American Ceramic Society, vol.83, pp.461, 2000.

[6] David Vanderbilt, Xinyuan Zhao and Davide Ceresoli, “Structural and dielectric properties of crystalline and amorphous ZrO_2”, Thin Solid Films, vol.486, pp.125, 2005.

[7] Shih-Ming Ho, “On the Structural Chemistry of Zirconium Oxide” Material Science Engineer, vol.54, pp.23, 1982.

[8] Alvise Benedetti, Giuliano Fagherazzi, Francesco Pinna, “Preparation and Structural Characterization of Ultrafine Zirconia powdwers,” Journal American Ceramic Society, vol.72, pp.467, 1989.

[9] Francisco del Monte, Willa Larsen, John D. Mackenzie, “Stabilization of Tetragonal ZrO_2 in ZrO_2–SiO_2 Binary Oxides,” Journal of American Ceramic Society, vol.83, pp.628, 2000.

[10] Sarit. Bhaduri, S. B. Bhaduri and Elison. Zhou, “Auto ignition synthesis and consolidation of Al_2O_3–ZrO_2 nano/nano composite powders”, Journal of Material Research, vol.13, pp.156, 1998.

[11] Ping. Li and I-Wei Chen, “Effect of Dopants on Zirconia Stabilization—An X-ray Absorption Study: I, Trivalent Dopants,” Journal of American Ceramic Society, vol.77, pp.118, 1994.

[12] Ping. Li and I-Wei Chen, “Effect of Dopants on Zirconia Stabilization—An X-ray Absorption Study: III, Charge-Compensating Dopants,” Journal of American Ceramic Society, vol. 77, pp.1289, 1994.

[13] F. Kazemi, A. Saberi, S. Malek-ahmadi, S. Sohrabi, H.R. Rezaie and M. Tahriri, “A Novel Method for Synthesis of Metastable Tetragonal Zirconia Nanopowders at low temeratures”, Ceramics-Silicate, vol. 55, pp. 26, 2011.

[14] David Vanderbilt, Xinyuan Zhao and Davide Ceresoli, “Structural and dielectric properties of crystalline and amorphous ZrO_2”, Thin Solid Films, vol. 486, pp.125, 2005.

[15] G. Palasantzas and J. Th. M. Ed Hosson, “The effect of mound roughness on the electrical capacitance of a thin insulating film”, Solid State Communications, vol.118, pp.203, 2001.

[16] N. P. Simonenko, E. P. Simonenko, V. G. Sevastanov, N. T. Kuznetsov, “Production of $8\%Y_2O_3$-$92\%ZrO_2$ (8YSZ) thin films by sol-gel technology”, Russia Journal of Inorganic Chemical, vol.60, pp.795, 2015.

[17] D. Bach and L. Price, in Microscopy and Microanalysis (Cambridge University press, Cambridge), vol.12, pp.416, 2006.

[18] José E.M. Lopesb, Marcelo M. Oliveira, Maria das Graças S. Costa, Gilvan P. de Figueredo, Jomar S. Vasconcelosc, José H.G. Rangela, “Chemical synthesis and characterization of Nb-ZrO_2”, Ceramics international, vol.42, pp.861, 2016.

[19] Uuganbayar Otgonbaatar, Wen Ma, Mostafa Youssef, and Bilge Yildiz, “Effect of Niobium on the defect chemistry and oxidation kinetics of tetragonal ZrO_2”, Journal of physical chemistry, vol.118, pp.20122, 2014.

[20] Apurba Sinhamahapatra, Jong-Pil Jeon, Joonhee Kang, Byungchan Han and Jong-Sung Yu, “Oxygen-Deficient Zirconia : A New Materilas for Solar Light Absorption”, Scientific Reports, vol. 6, article number 27218, 2016.

[21] K. C. Chiang, Ching-Chien Huang, G. L. Chen, Wen Jauh Chen, H. L. Kao and Yung-Hsien Wu, “High-Performance MIM Capacitors for Analog Applications”, IEEE Transaction Electronic. Device, vol.53, pp.2312, 2006.

[22] J. P. Chang and Y.-S. Lin, “Dielectric Property and Conduction Mechanism of Ultrathin Zirconium Oxide Films” Applied Physics Letter, vol.79, pp.3666, 2001.

4. Fabrication and characterization for semiconductor layer using MoS_2

4-1 Introduction

Recently, two dimensional (2D) materials have attracted significant attention because of their high carrier mobility and outstanding mechanical properties [1]. However, since the bandgap (E_g) of graphene is zero, graphene-channel transistors usually show ambipolar behavior with low on/off current ratio [2]. Although many investigations have been conducted in order to generate the bandgap for graphene, it is difficult to obtain a sufficiently large bandgap for practical applications. On the other hand, other types of 2D materials such as transition metal dichalcogenides (TMDC) also show great potential in nanoelectronics and optical applications. In particular, atomically layered molybdenum disulfide (MoS_2) has attracted attention in recent times. When the thickness of MoS_2 is reduced from bulk to nanosheet regime, the band structure transforms from an indirect (Eg=1.2 eV) to a direct (Eg=1.8 eV) [3,4] bandgap.

For fabrication of MoS_2 layers, there are many methods such as physical [6-7] and chemical [8-9] exfoliation, chemical vapor deposition (CVD) [10], hydrothermal synthesis [11], electrochemical synthesis [12], sulfurization of molybdenum oxides [13] and Mo metal [14]. Nevertheless, most MoS_2-based devices have been built on small flakes exfoliated from bulk in order to investigate of fundamental properties [15]. However, the small size and difficulty of finding the position of exfoliated for thin film has come up as the limitation. On the other hand, the chemical solution process is promising for large area formation of MoS_2 with simple equipment at low cost. Moreover, it is appropriate for synthesis with simple

control of the layer thickness by varying the concentration of the solution or the spinning speed [16].

The spin-coated MoS_2 film have been demonstrated at 1999 by J. Putz et al [17] using $(H_3NC_nH_{2n}NH_3)MoS_4$ precursor but in this stage, the report showed only a possibility of applying the solution process for MoS_2. After that, in 2012, Keng-Ku Liu et al[18] showed the MoS_2 fabrication on SiO_2 and sapphire using dip-coating. In 2015, Jaehyun Yang et al [16] made the MoS_2 on SiO_2 using the spin-coating. So far, most demonstrations of MoS_2 synthesis such as CVD and solution-based deposition have been carried out on the silicon dioxide (SiO_2) or sapphire substrate because of the thermal stability and flat surface of the substrates but the deposited MoS_2 film has to be transferred to other substrates such as high-dielectric-constant (high-k) thin films to fabricate high-performance devices. However, during the transfer process of the MoS_2 film, problems such as film wrinkle, chemical damage by etching solution of SiO_2 should be occurred. Hence, for practical thin film transistor (TFT) applications, it is necessary to investigate a direct deposition process of the MoS_2 film on high-k dielectric.

In this work, direct deposition of MoS_2 films using a “chemical” solution process on high-k thin films has been investigated. First, we demonstrate the coating properties of MoS_2 source solution prepared with $(NH_4)_2MoS_4$ dissolved in N-methyl-2-pyrrolidone on various kinds of high-k films. Next, we will explain about the selection of high-k oxide film for the MoS_2. Then, we demonstrate the growth of MoS_2 films on Nb-doped ZrO_2 film by using a two-step annealing method. This study also demonstrates that the thickness of the solution-derived MoS_2 can be controlled by the concentration of the source solution.

4-2 Fabrication procedure

We directly fabricated MoS_2 films through a chemical solution process on high-k films using an $(NH_4)_2MoS_4$ precursor. First, we investigated the coating properties of MoS_2 source solution on various kinds of dielectric oxide films. To understand the coating property of the MoS_2 precursor on various high-k films, the surface energies of the oxide films were estimated according to the contact angle measurements. As shown in table 2 each oxide film was carefully prepared with proper annealing process. The oxide films were dried at 110 °C for 1 min to evaporate the water on the surface before the surface energy measurements, and the contact angles were measured at room temperature by the sessile drop method with a goniometer-camera-computer system (DM300, Kyowa corp). To calculate surface energy of each oxide film, the van Oss-Chauhury-Good (OCG) equation (eq.4-1) and a definition of surface energy (eq.4-2) were applied.

$$\gamma^{L}(1+\cos\theta)=2\{(\gamma^{S,LW}\gamma^{L,LW})^{1/2}+(\gamma^{S+}\gamma^{L-})^{1/2}+(\gamma^{S-}\gamma^{L+})^{1/2}\} \quad \text{(eq.4-1)}$$

$$\gamma^{S}=\gamma^{S,LW}+2(\gamma^{S+}\gamma^{L-})^{1/2} \quad \text{(eq.4-2)}$$

where θ and γ are the contact angle and the surface tension of the strandard liquid, respectively, the superscripts of L and S mean the liquid and the solid (oxide substrate), and the LW, + and – indicate the Lifshitz-van der Waals, electron-acceptor, and electron-donor of the surface tension, respectively.

To solve eq.1, three unknown values ($\gamma^{S,LW}$, γ^{S+}, γ^{S-}) have to be identified using the contact angles measured by three standard solutions with a known value of $\gamma^{L,LW}$, γ^{L+}, γ^{L-} [19]. The standard liquids used in our experiments, were deionized water, diiodomethane, ethylene

glycol and glycerin and their surface energy components at room temperature are summarized in table 1. When the contact angle of ethylene glycol was too small, glycerin was used instead of ethylene glycol.

Table1. Used standard liquids and their surface tension components of the Lifshitz-van der Waals component (γ^{LLW}), electron-acceptor (γ^{L+}) and electron-donor (γ^{L-}) at room temperature for surface energy measurement.

Solution	γ^{LLW}	γ^{L+}	γ^{L-}	γ^{L}
Water	21.8	25.5	25.5	72.8
Diiodo-methane	50.8	0	0	50.8
Ethylene glycol	29	1.92	47	48
Glyserin	34	3.92	57.4	64

As mentioned later, of the high-k materials studied in this work, zirconium oxide (ZrO_2) was selected because of its relatively high dielectric constant (25~40) and superior thermal stability at high temperature (~1000 ºC) [20]. Furthermore, to enhance the dielectric constant and stabilize the phase of ZrO_2, niobium (Nb) doped ZrO_2 was used [21] Nb-doped ZrO_2 (NZO) films were prepared using a chemical solution process. To prepare the source solution of NZO, the zirconium acetate was dissolved in propionic acid in advance; then, the Nb 2-ethylhexanoate was inserted at a density of 0.1 mol/kg. Nb content was 30%. The NZO solution was stirred on a hot plate at 150 ºC for four hours. The prepared solution was spin-coated on the cleaned highly-doped Si substrate at 3000 rpm for 25 sec. The NZO film was annealed at 1000 ºC for 5 min in a pressure of 1 kPa with an air (N_2:O_2=3:1), prior to MoS_2 coating to circumvent unexpected crystal phase change and reaction with the MoS_2 which

anneals at 600-1000ºC. The details of NZO film formation along with electrical properties are given in chapter 2.

The source solution for MoS_2 was prepared as follows. The $(NH_4)_2MoS_4$ (99.97%, Sigma-Aldrich) of 0.052g powder was added to 4 g N-methyl-2-pyrrolidone (NMP) to prepare the 0.05 mol/kg of dark red solution. The $(NH_4)_2MoS_4$ solution was sonicated for 30 min. Next, the source solution for MoS_2 with the $(NH_4)_2MoS_4$ precursor was spin-coated on NZO-covered Si substrate with 3000 rpm for 120 sec. No surface treatment such as silane coupling agent was performed for NZO film. The spinning time had to be relatively long because the vapour pressure of NMP was low (0.048 kPa at 20 ºC). The spin-coated film was dried at 250 ºC for 5 min to evaporate the solvent. To confirm the growth of MoS_2 on NZO and to optimize the annealing conditions, we fabricated a rather thick film by repeating the coating and dry processes three times. In order to examine the controllability of the thickness and to fabricate thin films, we spin-coated the source solution with various concentrations (0.00625, 0.0125, 0.025, 0.05 mol/kg) only once.

The represented transformation processes of $(NH_4)_2MoS_4$ to MoS_2 are shown in eq.4-3 ~ eq.4-5 [22].

$$(NH_4)_2MoS_4 \rightarrow 2NH_3 + H_2S + MoS_3 \qquad \text{(eq.4-3)}$$

$$MoS_3 \rightarrow MoS_2 + S \qquad \text{(eq.4-4)}$$

$$(NH_4)_2MoS_4 + H_2 \rightarrow 2NH_3 + 2H_2S + MoS_2 \qquad \text{(eq.4-5)}$$

As shown in eq.1, the thermolysis of $(NH_4)_2MoS_4$ in an N_2 environment resulted in the decomposition of $(NH_4)_2MoS_4$ into MoS_3, and the transform of MoS_3 to MoS_2 (eq.4) required a high temperature (> 800 ºC) annealing process. It has been also suggested that the

conversion temperature of $(NH_4)_2MoS_4$ to MoS_2 can be reduced to ~ 425 ºC in the presence of H_2 gas as described in eq. 4-5. The reaction process shown in eq.4-5 is sensitive to the presence of oxygen. If there is oxygen, $(NH_4)_2MoS_4$ is partially changed to MoO_3, thus, the reducing atmosphere (H_2 gas) is needed to avoid oxidation during the annealing process. In this work, prior to the H_2/Ar gas introduction, the quartz tube of the RTA system was evacuated by a mechanical pump to less than 2 Pa. We repeated the purge process three times using Ar gas and a mechanical pump before the annealing.

The carbon contamination from the residual solvent is one of the major causes of sulfur deficit in the composition [17] and the produced MoS_2 films are often amorphous or have low crystallinity. Therefore, to prevent sulfur deficiencies in the film and to obtain high quality of MoS_2, a sulfur atmosphere is needed during the crystallization annealing process even though sulfur atoms are emitted from the film according to the reaction shown in eq. 4-4. In this work, we apply a sulfur atmosphere using the quartz box (width:length:height=5:5:4 cm) that contains sulfur powder (99.98%, Aldrich). To control internal pressure of sulfur vapor by external Ar pressure, holes are formed on quartz box as shown in figure 4-1. Use of H_2S gas was avoided because of its hazardous nature.

Considering the various aspects mentioned above, we choose two step annealing process indicated in figure 4-2. Firstly, the spin-coated and dried MoS_2 film on NZO/Si substrate was annealed at 450 ºC in a reducing atmosphere (H_2:Ar=5%:95%, forming gas, 1 kPa) for 20 min. Then, the film was inserted into the quartz box with 0.001g of sulfur powder and annealed again at 600~ 1000 ºC in Ar inert gas (1 kPa) for 20 min.

Figure 4-1. Picture of quartz box for thermal treatment of MoS_2.

The Raman scattering spectroscopy characteristics of the synthesized MoS_2 films were analyzed using T64000 (Horiba corp.) with a wavelength of 532 nm and a power of 20 mW. The Raman signals were normalized by the intensity of Si peak at 523 cm^{-1}. X-ray photoelectron spectroscopy (XPS) was conducted using an AXIS ULTRA with a monochromatic Al Kα (1486.7 eV) X-ray source. The binding energy was calibrated with a C 1s peak of 284.8 eV to eliminate the charging effect of the sample during XPS analysis. Transmission electron microscopy (TEM) was performed using JEM-ARM200F with acceleration energy of 200 keV. Grazing incidence X-ray diffraction (GI-XRD) was analyzed using X`PERT PRO with a monochromatic Cu Kα (1.542 Å) X-ray source. When the MoS_2 films were measured by XRD, the incidence angle was fixed at 0.3~0.45 degree then only the detector was moved to collect the signals. Thermogravimetry(TG)/Differential thermal analysis (DTA) was conducted using SEIKO EXSTRA6000 in N_2 atmosphere with temperature rate

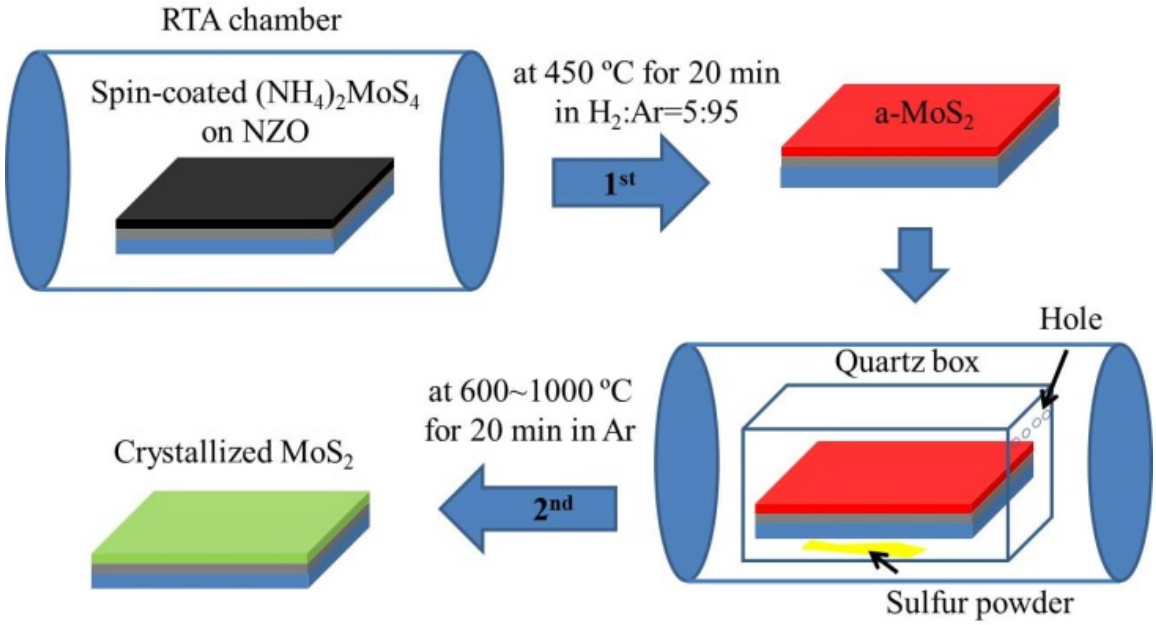

Figure 4-2. Schematic illustration for the synthesis process of MoS_2 film used in this work.

4-3 Results and discussion

In solution process for MoS_2, the existence of the tetrathiomolybdate anion (MoS_4^{2-}) anion is important. There are several kinds of precursor for this anion but the most simple one is $(NH_4)_2MoS_4$. For the solvent, the candidates were dimethylformamide (DMF), dimethyl sulfoxide (DMSO), N-Methyl-2-pyrrolidone (NMP) which has same polar aprotic type. Among them, I selected NMP as a solvent, although many other researches usually used the DMF. There were three reasons for this. First issue is stability of the solution. As shown in figure 4-3(a) and (b), in case of DMF, the yellow particles were attached on glass surface and the precipitate also were generated only after one day. The colour of solution was dark red but it was changed to bright red after several days even though it was sealed. Although the mechanism or chemical reactions for these changes are not clear, these degenerated solutions

showed bad coating property on oxide film. However, the solution dissolved in the NMP and the DMSO is stable and there is no change of solution state as shown in figure 4-3 (c) and (d).

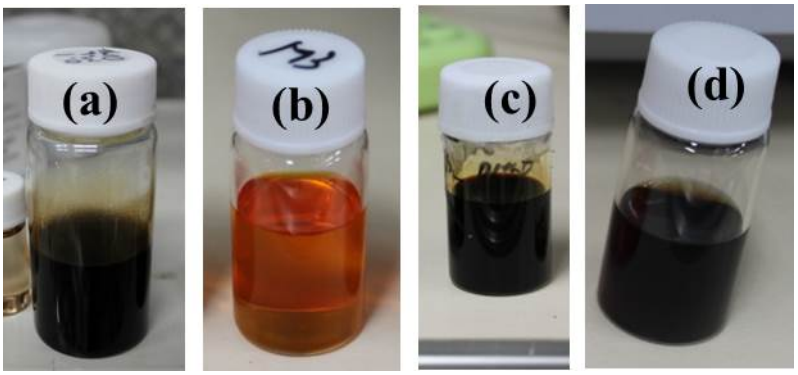

Figure 4-3. Solution state $(NH_4)_2MoS_4$ is dissolved in DMF (a)after two day, (b)after one week, (c) in DMSO (d) in NMP after two day.

Second reason was film uniformity. When the precursor dissolved in DMF was spin-coated on the NZO film, the spin-coated film was not uniform and had a textured structure (figure 4-4(a)), even though the spin-coating process was carried out immediately just after the preparation of source solution. The spin-coated film using NMP was uniform as shown in figure 4-4(b).

Third one was small solvent contamination effect for decomposition of $(NH_4)_2MoS_4$. Figure 4-5 (a) shows the TG/DTA graph of the $(NH_4)_2MoS_4$ powder which was analysed in N_2 atmosphere [23].The $(NH_4)_2MoS_4$ decomposes to MoS_x under between 160 and 220 °C. MoS_x is changed to MoS_2 between 200 °C and 360 °C. The MoS_2 was recombined with oxygen then changed to MoO_3 between 360 °C and 425 °C. These processes make two large peaks near 200 °C and 400 °C in DTA spectrum. The DTG peak position of $(NH_4)_2MoS_4$ dissolved in DMSO (figure 4-5(b)) shows several peaks between 250 °C and 400 °C. It means that there are other reactions due to the solvent contaminant.

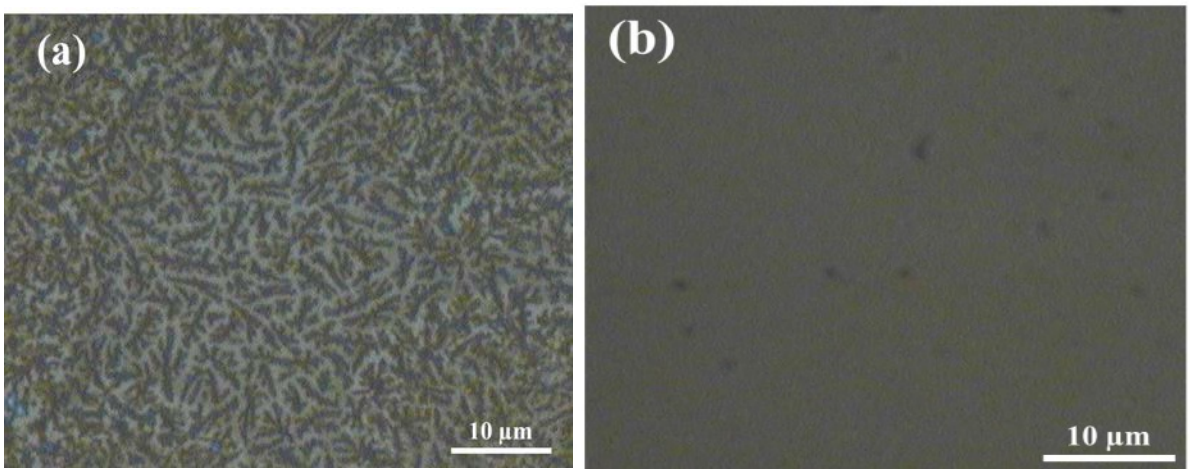

Figure 4-4. Photographs of the spin-coated MoS_2 films on NZO using the $(NH_4)_2MoS_4$ precursor solution dissolved in (a) DMF and (b) NMP.

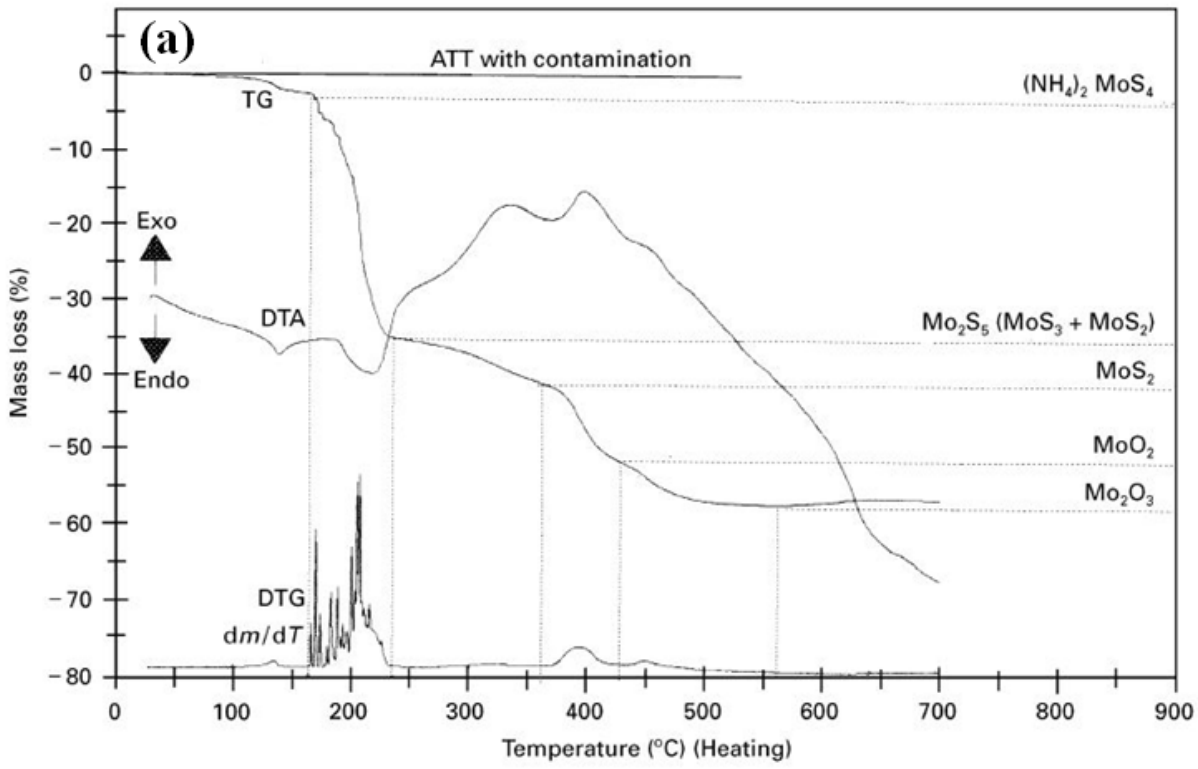

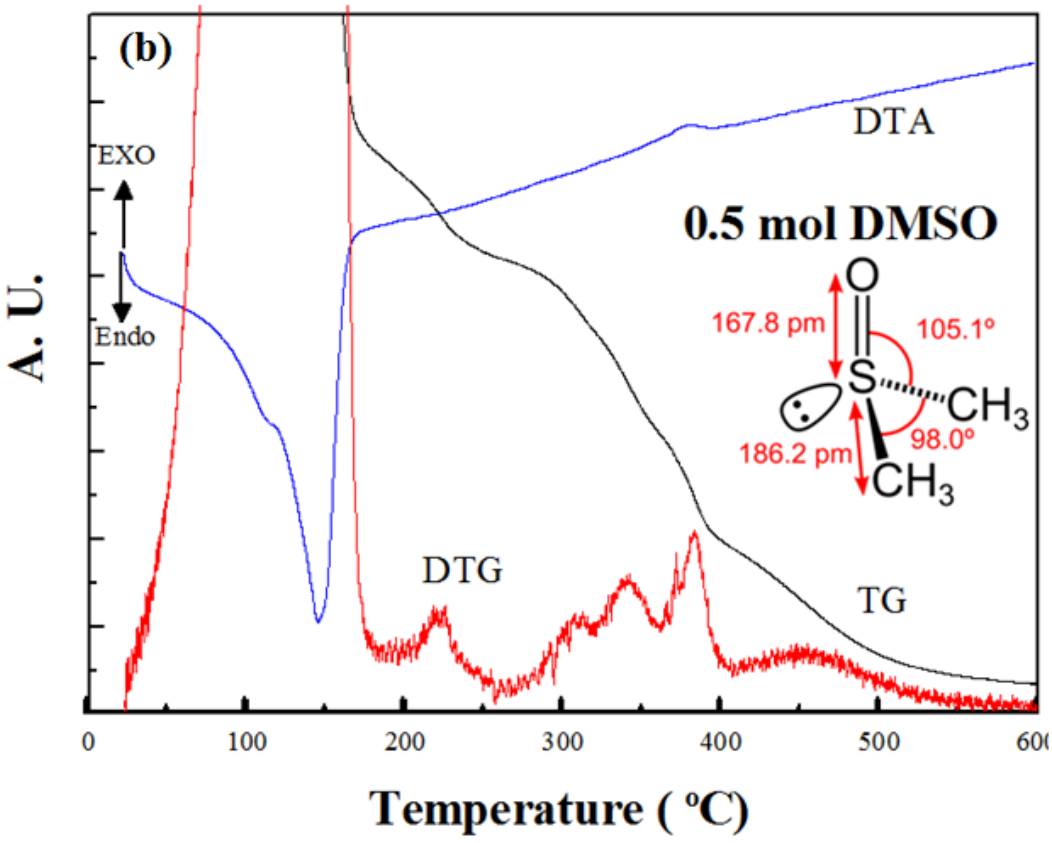

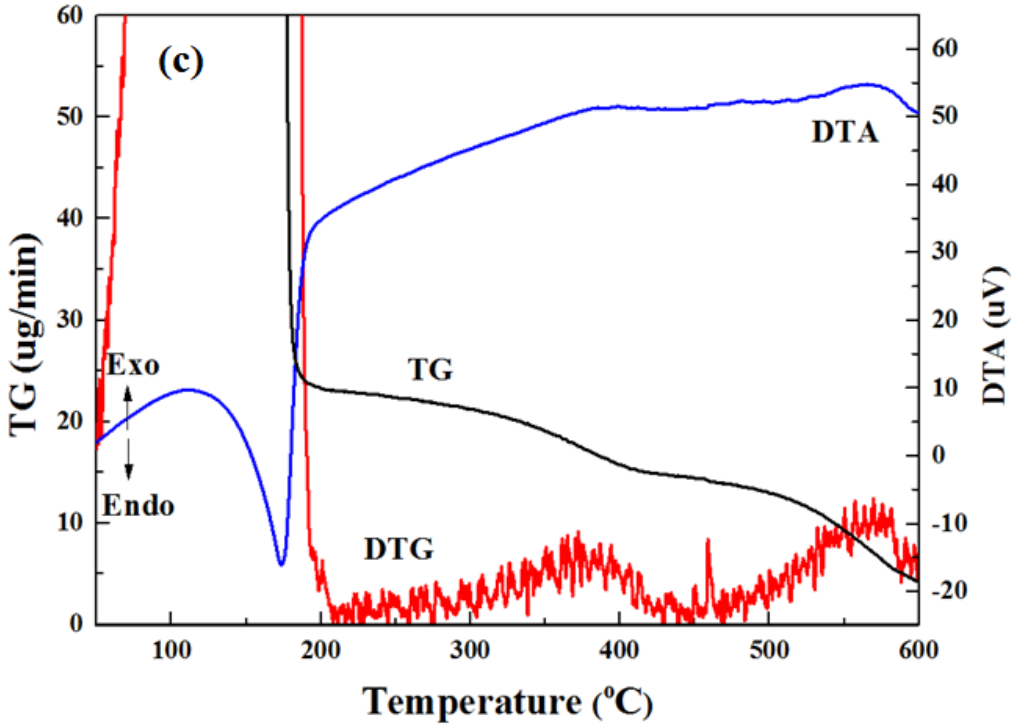

Figure 4-5. TG/DTA chart of $(NH_4)_2MoS_4$ (a) raw material and it was dissolved in (b) NMP, (c) DMSO.

Although the DTG peak position of $(NH_4)_2MoS_4$ dissolved in NMP (figure 4-5(c)) solvent under 200 °C does not show due to a large boiling temperature of NMP (205 °C), it shows same peak position with raw precursor (figure 4-5 (a)) between 360 °C and 400 °C. It means that the NMP shows small effect of decomposition of $(NH_4)_2MoS_4$ for MoS_2. Therefore, we have used the NMP solvent instead of DMF.

It needs relatively high annealing temperature (1000 °C) and sulfur atmosphere are needed for MoS_2 thermal treatment process. These conditions could be an important restriction to select gate dielectric materials. In table 2, the state of the MoS_2 at 1000 °C in sulfur atmosphere on various oxide films, is summarized. The "good" means that there is no change by optical microscope observation. In case of HfO_2, the spin-coated HfO_2 on Si substrate was annealed at 1000 °C in O_2 atmosphere, there is no change.

Table 2. Surface state change for the materials annealed at 1000 °C in Ar and annealed at 1000 °C with MoS_2.

Material	Annealing at 1000 °C in Ar	Annealing at 1000 °C with MoS_2
HfO_2	Good	Bad
$(Bi,La)_4Ti_3O_{12}$	Good	Bad
$YbTiO_x$	Good	Bad
$LaTaO_x$	Good	Bad
La_2O_3	Good	Good
ZrO_2	Good	Good
$NbZrO_x$	Good	Good
$AlNbZrO_x$	Good	Good

However, as shown in figure 4-6(a), when the MoS_2 precursor was spin-coated on the HfO_2 and was annealed at 1000 °C in sulfur atmosphere, the surface state of HfO_2 was

changed. Hence, I excluded HfO_2 as a gate insulator for MoS_2 transistors. The ferroelectric $(Bi,La)_4Ti_3O_{12}$ (BLT) was not changed, either, when it was annealed at 1000 °C in O_2 atmosphere but the surface colour was turned to white when it was annealed at 1000 °C in sulfur atmosphere. The surface state of $LaTaO_x$, $YbTiO_x$ also showed similar changes as the BLT.

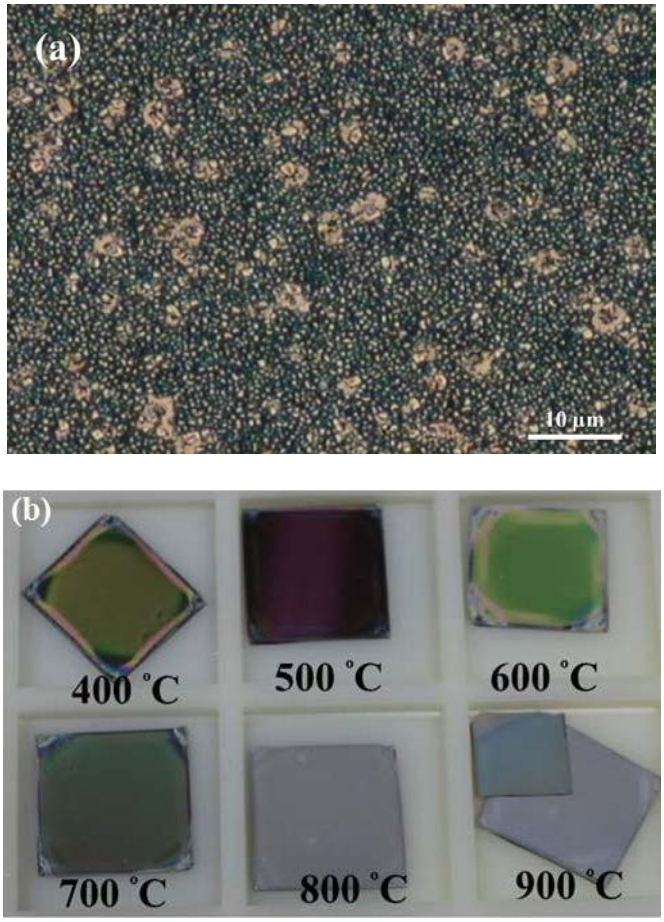

Figure 4-6. Photographs of the spin-coated MoS_2 films on (a) HfO_2 and (b) $(Bi,La)_3Ti_4O_{12}$ using the $(NH_4)_2MoS_4$ precursor solution dissolved in NMP.

To investigate the coupling state of oxide material, XPS measurement was conducted. The XPS of Mo 3d peaks when MoS_2 was formed on the La_2O_3, $YbTiO_x$, $LaTaO_x$ and BLT were compared in figure 4-7. In the XPS of Mo 3d orbital, there are Mo $3d_{3/2}$ peak at 229. 8 eV,

Mo $3d_{5/2}$ peak at 232.9 eV for a MoS_2 and Mo $3d_{3/2}$ peak at 236. 4 eV, Mo $3d_{5/2}$ peak at 233.1 eV for a MoO_3 and S 2s at 227 eV. The XPS of the MoS_2 on La_2O_3 shows peaks related to MoS_2 but there are not only MoS_2 peaks but also MoO_3 peaks in the $LaTaO_x$. Moreover, the XPS for $YbTiO_x$ and BLT shows only MoO_3 peaks.

As shown in figure 3-1, the Ta_2O_5 and TiO_2 could not be used for Si due to a reaction with Si and decomposition of the oxide. Figure 4-7 (b), (c) shows the XPS of Ta 4f for $LaTaO_x$ and Ti 2p for $TbTiO_x$, respectively. These spectrums were analysed by Gaussian function. There are raw metal peaks, significantly. It means that Ta_2O_5 and TiO_2 were decomposed to metal. The detached oxygen from oxide film could be combined with Mo instead of S.

Therefore, the oxide film which have Ta and Ti atoms, could not be applied for substrate of solution processed MoS_2.

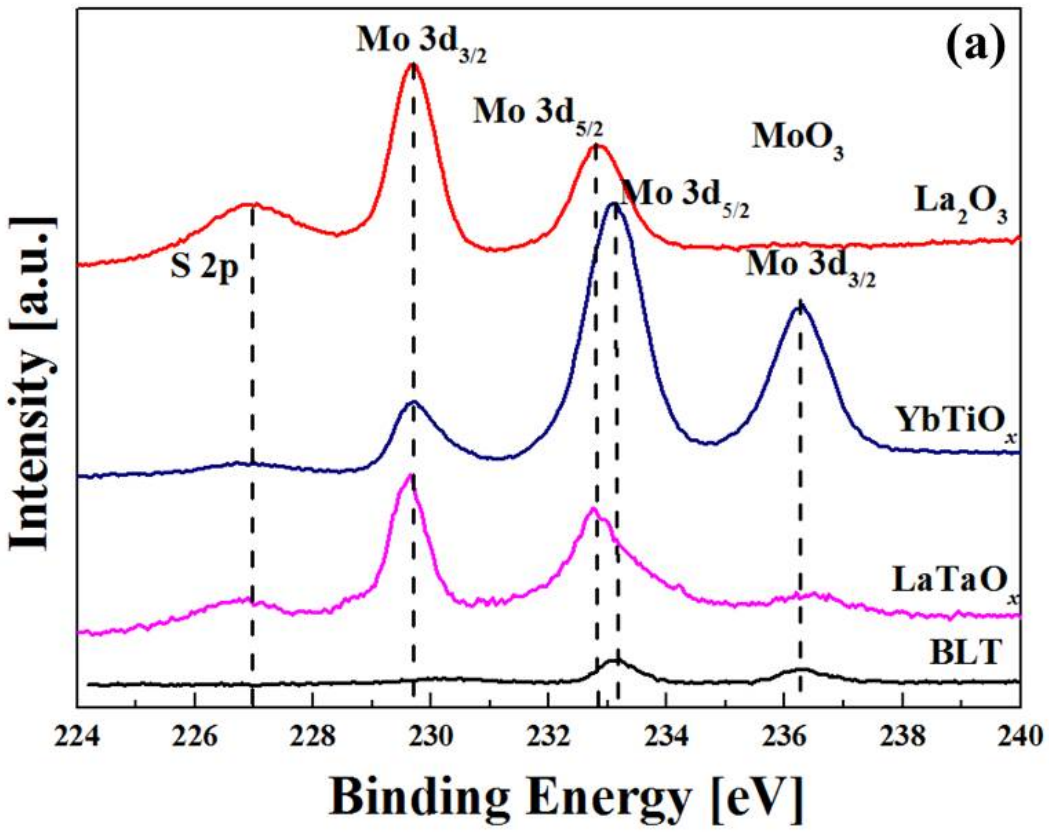

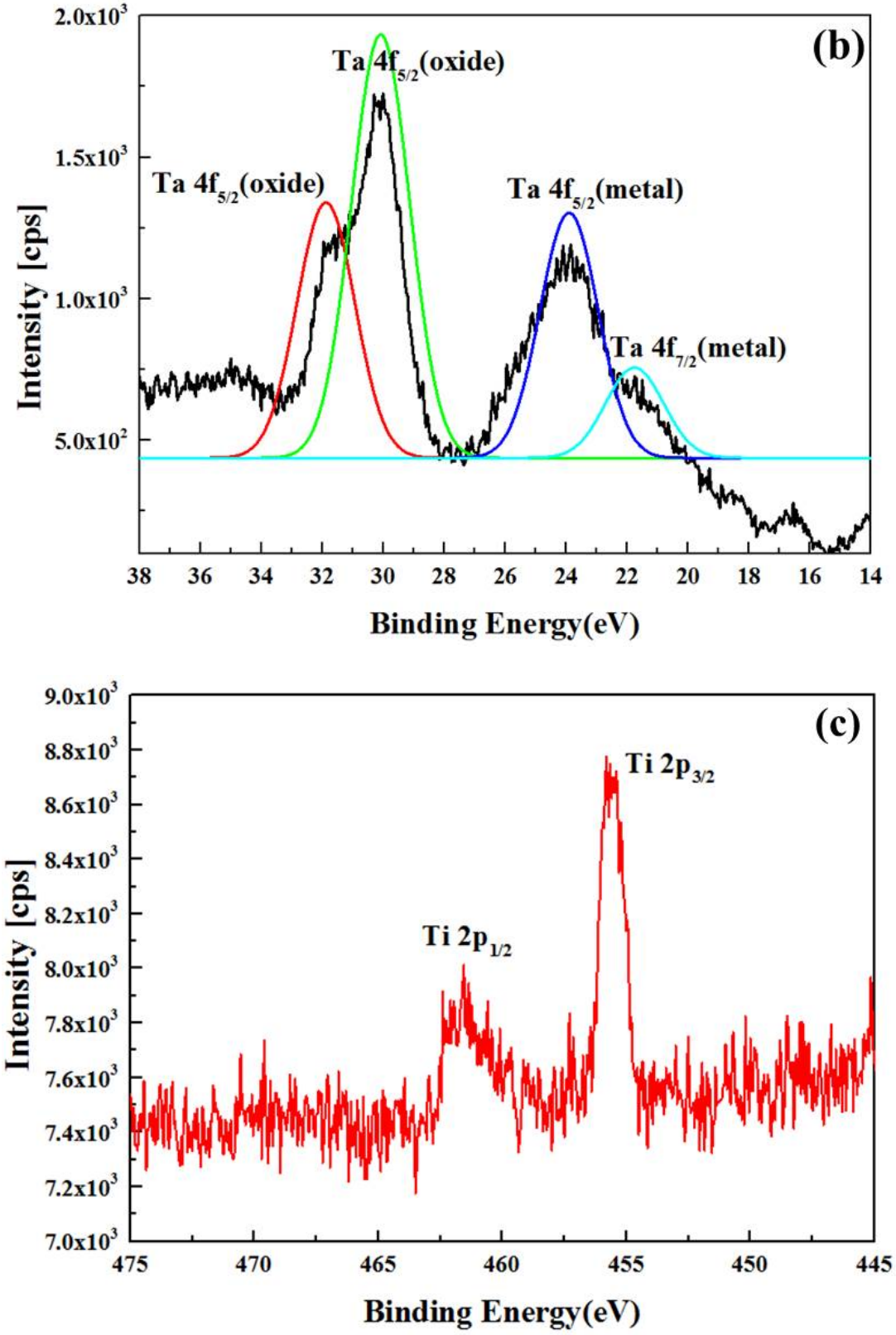

Figure 4-7. XPS spectrum of (a)Mo 3d for La_2O_3, $YbTiO_x$, $LaTaO_x$ and BLT,(b)Ta 4f for $LaTaO_x$ and (c) Ti 2p for $YbTiO_x$.

The morphology of MoS_2 precursor spin-coated on SiO_2 has many pores as shown in figure 4-8(a) and on $Pb(Zr,Ti)O_3$ in figure 4-8 (b). The coating property is strongly related to the surface energy [24]. The estimated contact angles and calculated components of the oxide substrate are summarized in table 3, along with the coating state and film state after annealing at 1000 ºC with sulfur. In general, the substrate with high surface energy could be coated more easily. However, the $Pb(Zr,Ti)O_3$ (PZT) film, which has the highest surface energy in table 3, showed poor coating property identical to figure 4-8(b) for the $(NH_4)_2MoS_4$ solution. Although the other oxide films such as Al_2O_3, HfO_2, ZrO_2 and $(Bi,La)_4Ti_3O_{12}$ have lower surface energy than PZT, the coating property was found to be good. It is evident in table 3 that PZT has a large electron-acceptor ($\gamma+$) value. The other substrates which exhibited poor coating property, Si and SiO_2 also have large $\gamma+$ values. Therefore, to obtain a fully covered film, the ionic nature of the substrate has to be considered as well as the surface energy.

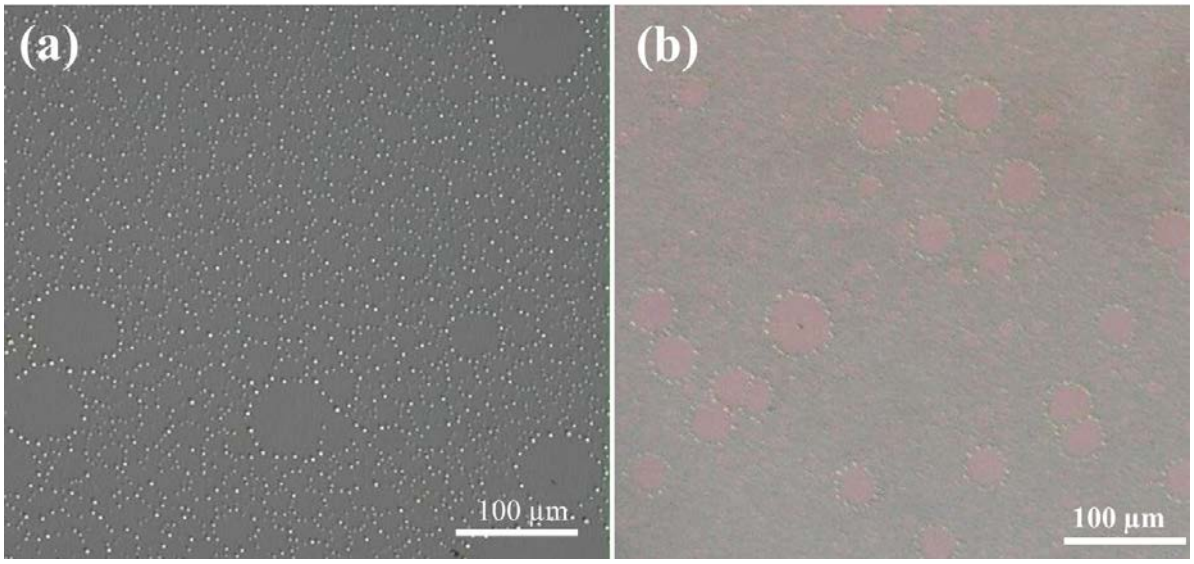

Figure 4-8. Surface morphology of $(NH_4)_2MoS_4$ dissolved in NMP solution on (a) SiO_2 and (b) $Pb(Zr,Ti)O_3$.

Putz et al. have suggested the solution structure of $(NH_4)_2MoS_4$ [26], when $(NH_4)_2MoS_4$ is dissolved in solvent, there is the network linked via [RNH_2—H—NH_2R] cations as shown in figure 4-9 (a), where the proton is stabilized via two NH_2 molecules, which may play an important role for coating properties. If the substrate surface has a significant amount of positive ions, it becomes difficult to deposit the films because of the Coulomb repulsive force with cations as shown in figure 4-9 (b). For Si, SiO_2 and PZT, the estimated γ+ values were relatively high. Hence, it is difficult for the $(NH_4)_2MoS_4$ solution to be spin-coated completely.

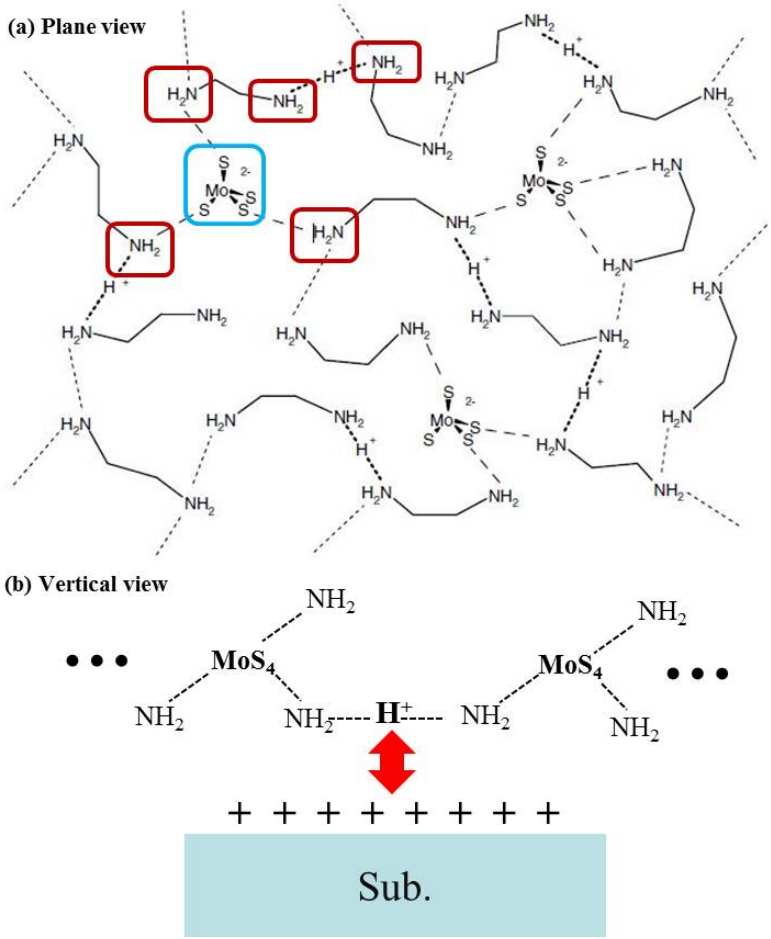

Figure 4-9. Structure of $(NH_4)_2MoS_4$ solution (a) plane view refered from [26] and (b) vertical view.

Table 3 Summary of the estimated contact angle of the test liquid, calculated surface energy components, coating state and film state annealed at 1000 °C with sulfur

Substrate	Contact angle				γ_s^{LW}	γ_s^+	γ_s^-	γ_s	Coating state	Film state annealed at 1000 °C with sulfur
	water	diiodomethane	Ethylene glycol	glycerin						
Al_2O_3	33.8	38.9	32.7	-	40.2	0	54.1	40.4	good	good
HfO_2	24.8	32.6	21.7	-	41.9	0.08	65.3	46.5	good	poor
ZrO_2	9.7	34.2	-	15.6	42.4	0.07	64.5	46.6	good	good
$Pb(Zr,Ti)O_3$	31.4	27.1	-	38	45.4	0.47	41.6	54.2	poor	-
$(Bi,La)_4Ti_3O_{12}$	24.8	32.6	27	-	40.4	0.06	46.3	43.8	good	poor
LZO	23.5	28.7	1.0		44.7	0.065	54.4	48.5	good	-
NZO	34.3	35.4	19.9		41.8	0.1	47.0	47.3	good	good
ALZ	17.3	35	0.7		42.0	0.1	60.1	47.3	good	-
Si	59.7	48.8	38.1	-	35.0	0.43	22.3	41.2	poor	-
SiO_2	47	45.1	25.1	-	37.5	0.53	33.4	45.4	poor	-

Although the $(NH_4)_2MoS_4$ precursor was coated well on the oxide films such as HfO_2, we could not obtain good MoS_2 film formation when it was annealed at 1000 ºC with sulfur (figure 4-6(a)). The ZrO_2 based oxide substrate shows both good coating film and no change after high temperature annealing with sulfur. Hence, we use ZrO_2-based high-k film as a substrate.

The XPS spectra for the Mo and S regions are indicated in figure 4-10 for the solution-processed MoS_2 films fabricated on NZO with different annealing temperatures. The Mo 3d doublets at 232.9 eV ($3d^{5/2}$) and 229.8 eV ($3d^{3/2}$) are clearly found when the annealing temperature is more than 700 °C in figure 4-10(a). The sulfur of the 2p doublet peaks are positioned at 163.75 eV ($2p^{1/2}$) and 162.66 eV ($2p^{3/2}$) (figure 4-10(b)). The intensities of both Mo and S peaks become larger with the annealing temperature. On the other hand, when the film was annealed at 450 ºC in H_2/Ar gas, the intensities of these peaks are small. In addition, the Mo peak related to MoO_3 is observed as shown in figure 4-10(a), which indicates Mo atoms react with oxygen partially and they are not fully combined with sulfur atoms. This is probably due to the residual oxygen in the annealing furnace. If the $(NH_4)_2MoS_4$ is reacted with oxygen of the NZO film, the MoO_3 trace has to be found for films fabricated at higher annealing temperature, which is not the case in this work.

To investigate the crystalline properties of MoS_2 films fabricated with different annealing temperature, GI-XRD (figure 4-11) patterns and Raman (figure 4-12) spectra were measured. In figure 4-11, a small peak found at 30º is from NZO (111) oxide. The film annealed at 450 ºC in only Ar atmosphere has XRD peaks at 12.6º and 25.7º, which suggests the formation of MoO_3 (020) and (040) instead of MoS_2. As mentioned previously, the H_2 gas is important in suppressing the oxidation in the reaction process.

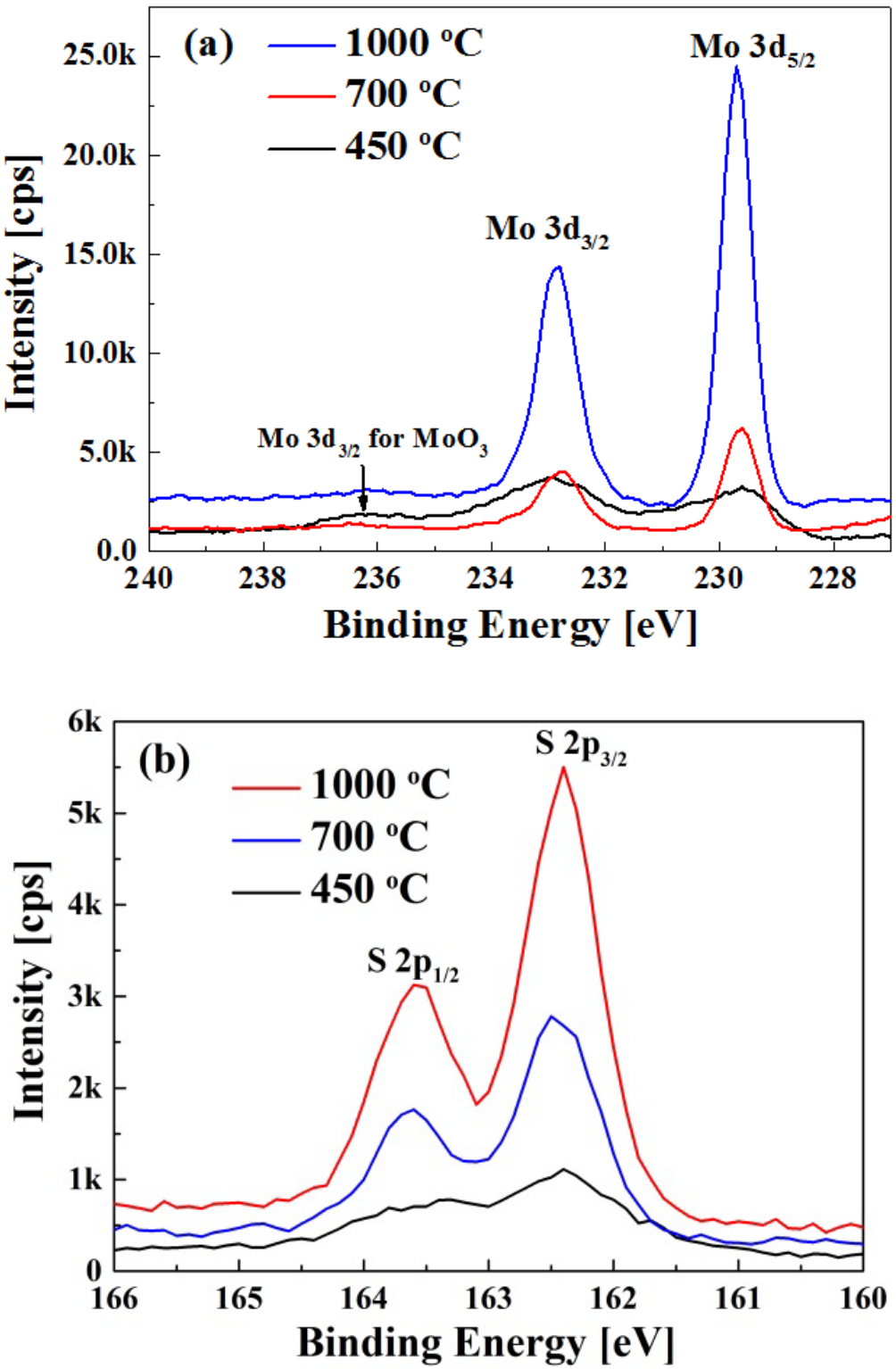

Figure 4-10. XPS spectra for (a) Molybdenum (Mo) 3d and (b) Sulfur (S) 2p peaks of the solution-processed MoS_2 film with different annealing temperatures.

In fact, the X-ray diffraction peaks from MoO_3 are found when the film was annealed at 450 ºC without H_2/Ar gas (figure 4-11(a)). For the film annealed at 600 ºC in forming gas, small broad peaks around 14º are observed, which suggests MoS_2 formation as a result of the imperfect crystalline nature of the film. For the films fabricated with the annealing temperature of higher than 700 °C, XRD peaks of MoS_2 (002) at 14 º were clearly found, moreover, the peak intensity becomes larger as the annealing temperature increases. Only the (002) diffraction from the MoS_2 crystallites is observed. The size of the crystallites can be calculated using the Scherrer formula (eq. 4-6).

$$D=K\lambda/\beta \cos(\theta) \qquad \text{(eq.4-6)}$$

where β is the full width half maximum (FWHM) in radians that the graph was refined by using Gaussian function; K is a constant (0.89); θ is the diffraction angle; and λ is the Cu Kα wavelength (1.54 Å).

The calculated grain size also increases from 8.8 nm for the film annealed at 700 ºC to 27.1 nm for the film annealed at 1000 ºC. Hence, it is found that high temperature annealing enhances the crystalline growth of MoS_2. However, it should be noted that the eq.4-6 is valid for conventional polycrystalline films.

Figure 4-12 shows the Raman spectra measured for the film fabricated with various annealing temperatures. The MoS_2 film annealed at 450 ºC (first step only) shows unclear peak at 387.0 cm-1 (E_{2g}) and 410.0 cm-1(A_{1g}) because of its low crystallinity whereas after higher temperature (> 600 ºC) annealing with sulfur vapor (second step), clear peaks can be observed at 384.2 cm-1(E_{2g}) and 410.0 cm-1(A_{1g}).

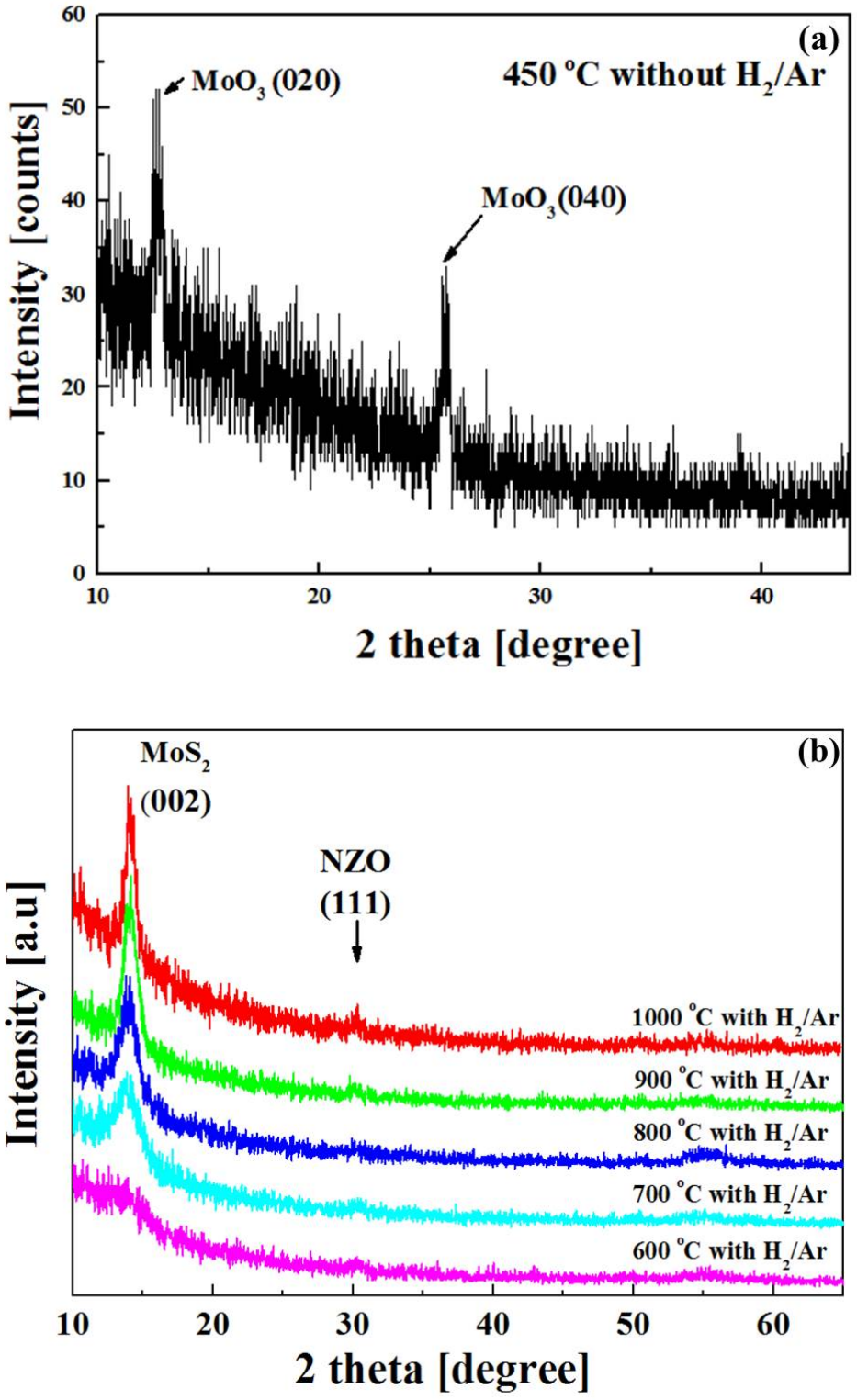

Figure 4-11. GI-XRD patterns of the MoS_2 film fabricated by (a) the solution process with various thermal treatment temperatures with H_2/Ar and (b) without H_2/Ar atmosphere.

The MoS_2 film annealed at 1000 ºC shows a high intensity and narrow FWHM. It is interesting to note that the peak separation (between the peak of the E_{2g} mode to the peak of the A_{1g} mode) for films annealed at 1000 ºC film is wider than that for those annealed at lower temperatures. There are two possible reasons for this: the effects of thickness and the grain boundary density. It is well known that a thick MoS_2 film has wider peak separation than a few layers MoS_2 [26]. On the other hand, it is reported that the peak separation becomes narrow at the edge of the MoS_2 [27], which means if the film has a lot of grain boundaries, the peak separation will decrease. As shown in figure 4-11(b), in our experiments, the calculated grain size of the MoS_2 annealed at 600 °C is smaller than that of the film annealed at 1000 °C. Hence, the Raman signal for the film annealed at 600 °C contains the effects of grain boundaries to a greater extent.

To observe how the layered MoS_2 was grown on NZO dielectric film, we performed TEM observations for the MoS_2 films annealed at 600, 800 and 1000 °C. The cross section TEM images of MoS_2 fabricated on NZO are shown in figure 4-13. It is evident that the surface of NZO has a curved surface and layered-structure MoS_2 was grown conformally. Note that the layer of MoS_2 is parallel to the surface, which contrast with the sputtered film ,where perpendicular grains were observed for thick MoS_2 films [28].

The MoS_2 film with a layered structure parallel to the surface is advantageous for transistor applications because high mobility is observed for this direction. The TEM cross section of MoS_2 film annealed at 600 ºC is shown in figure 4-13(a). When the annealing temperature is 600 °C, the discontinuity of the crystalline is found in very short length (< 3 nm); this indicates small crystallites were grown. Note that the layers of the MoS_2 crystallites follow on the curved NZO surface even when the annealing temperature is 600 °C.

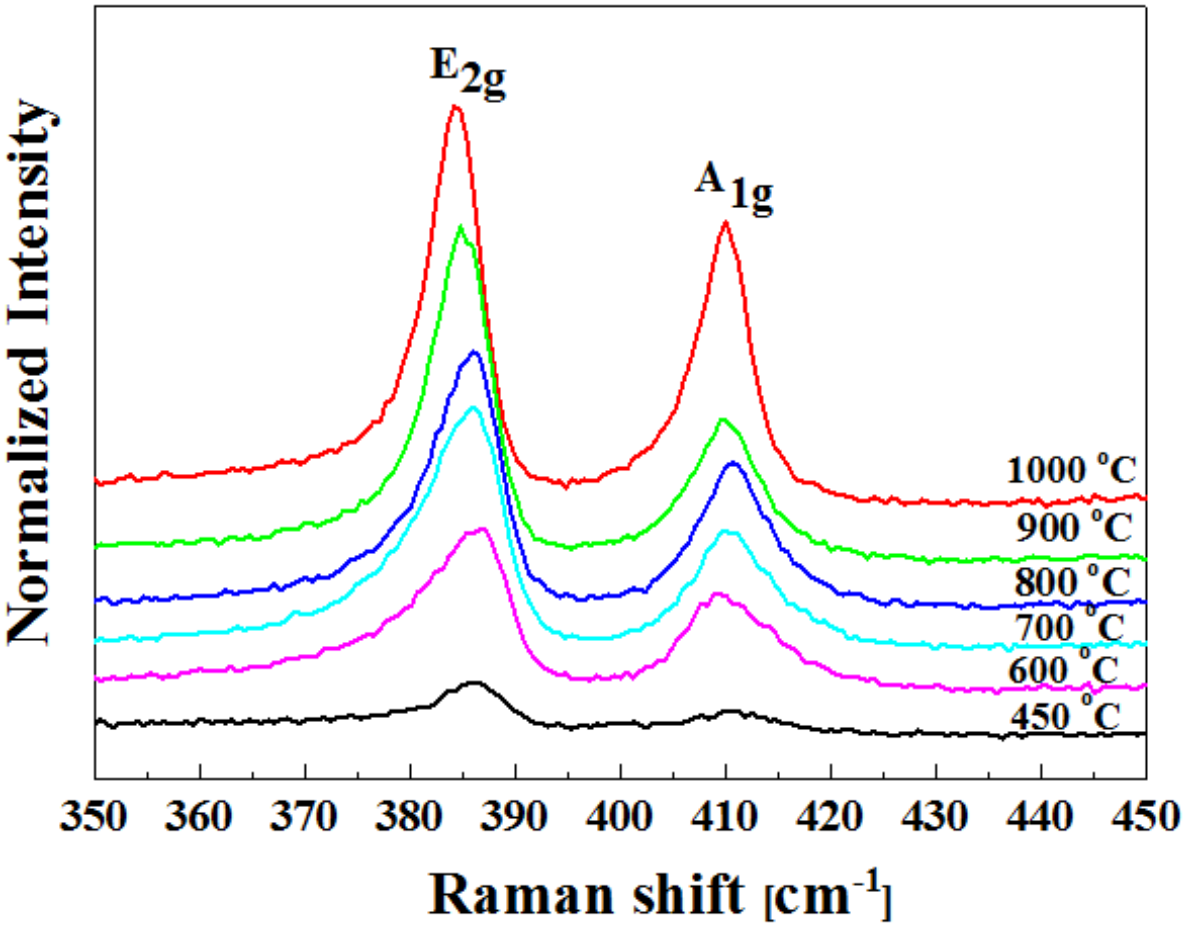

Figure 4-12. Raman spectra of MoS_2 films fabricated by solution process with different annealing temperature.

When the film was annealed at 800 °C, a longer continuously MoS_2 layered structure is apparent (figure 4-13(b)). The MoS_2 film annealed at 1000 ºC has a clear and long layered structure as shown in figure 4-13(c), which confirms the enhancement of the growth of MoS_2 at high annealing temperatures. It is also clear that MoS_2 film grown at 1000 ºC is thicker than this annealed at 600 ºC. These TEM observations clearly show that the growth of MoS_2 layered structure was enhanced at high annealing temperature, which is consistent with the results of XRD and Raman scattering measurements.

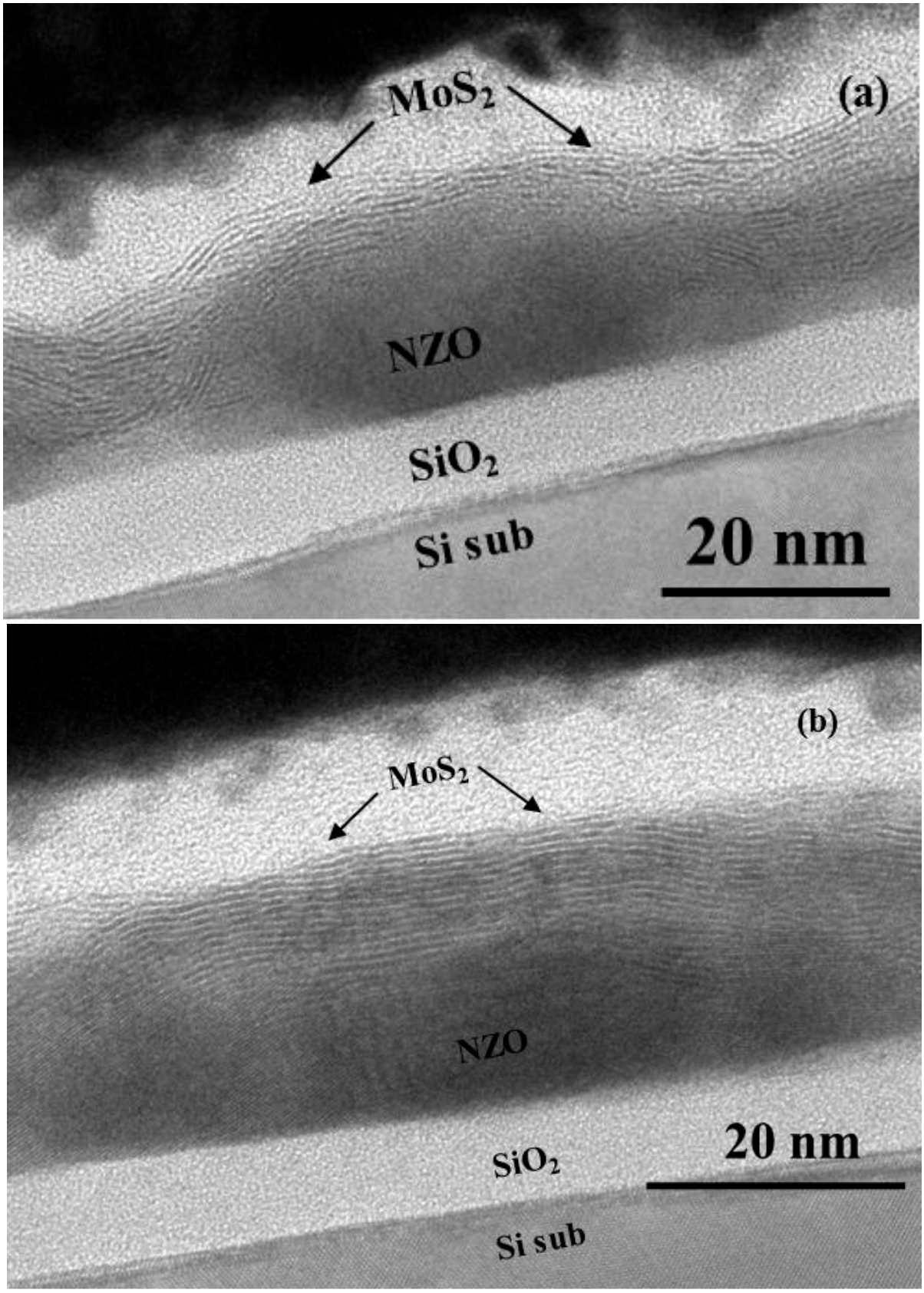
MoS2
(a)
NZO
SiO2
Si sub
20 nm
(b)
MoS2
NZO
SiO2
Si sub
20 nm

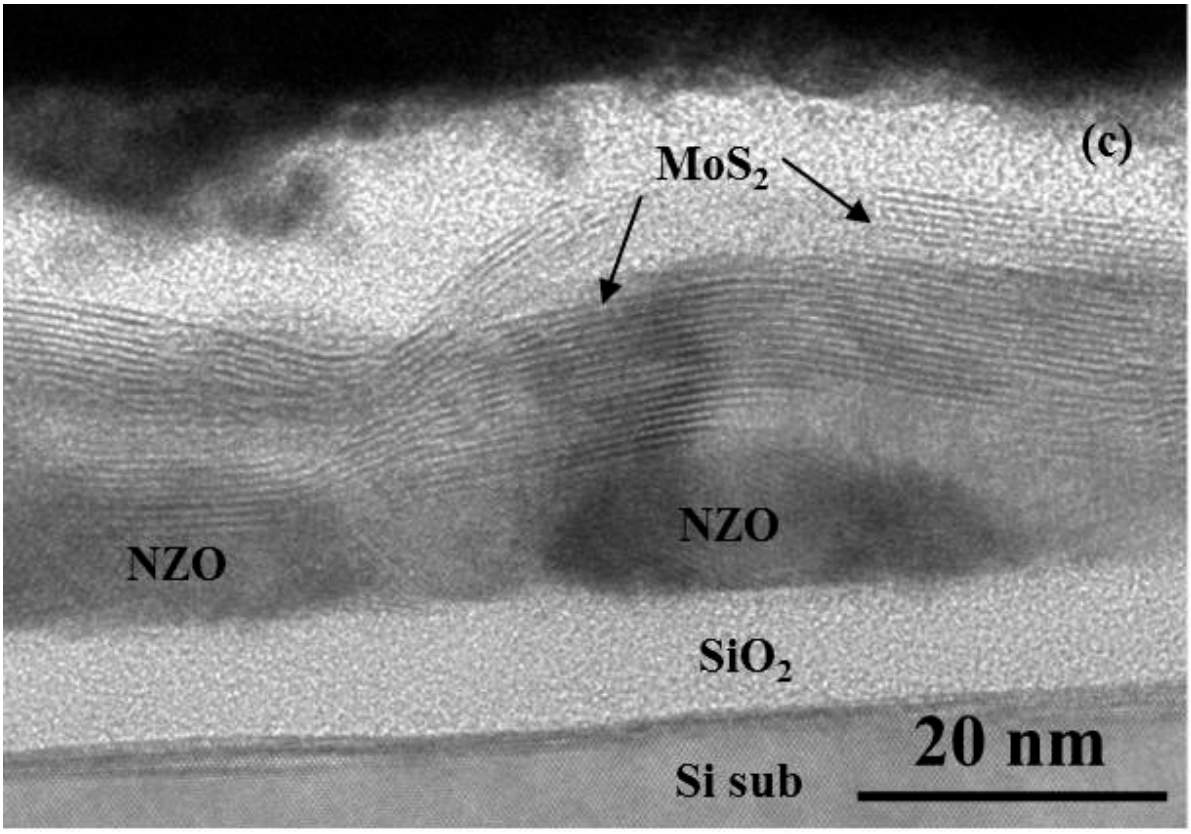

Figure 4-13. MoS_2 film annealed at (a) 600, (b) 800 and (c) 1000 ºC on the NZO.

MoS_2 normally shows n-type semiconductor, but it is reported that Nb is p-type dopant. Hence, to check the diffusion of Nb atom from NZO film to MoS_2, the EDS data was shown in figure 4-14 for Nb and Zr, respectively. Figure 4-14(a) shows the MoS_2 film was grown on NZO. It is hard to judge the diffusion of Nb by comparing the figures, but it is shown that the Nb atoms are located in the film where Zr is detected as shown in figure 4-14 (b) and (d). Hence, Nb diffusion is not so serious, even though the sample was annealed as high as 1000 ºC.

As seen in figure 4-15(c), the expectative grain size was under 100 nm, which is smaller than that of the MoS_2 fabricated CVD technique. One of the reasons for this is that the growth of MoS_2 in solution process takes place in the film during the annealing process after the film

coating, whereas in the CVD technique the growth takes place at the substrate surface heated at high temperature. Another reason is most likely the roughness of the NZO film. If the oxide film with small roughness was used, a larger grain size would be obtained. The growth of the MoS_2 on flat substrates is now under study and will be reported in future. However, from the point of view of device applications, it can be mentioned that films with small grain size produce TFTs with good uniformity in large area. Therefore, the MoS_2 film fabricated using solution process is still promising if the mobility is reasonably high.

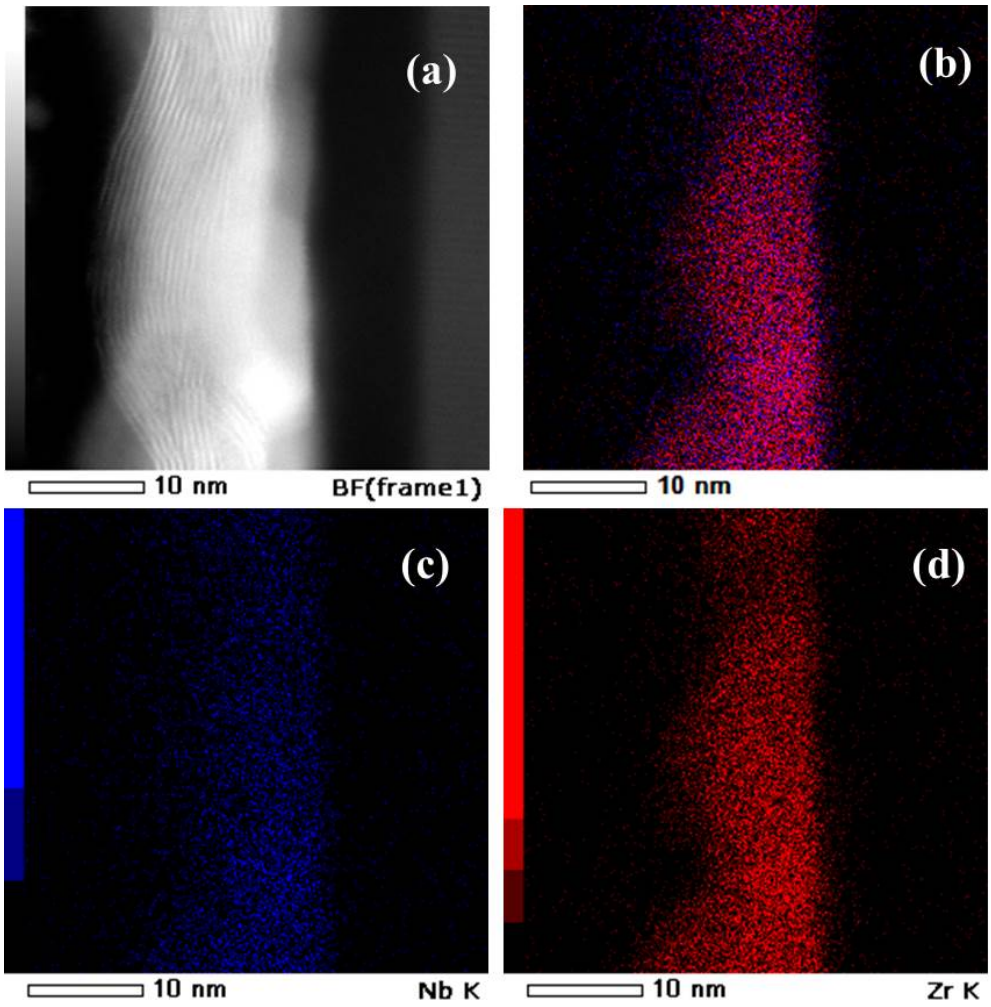

Figure 4-14. EDS profile of MoS_2 on NZO. (a) TEM image, (b) merged Nb and Zr distribution (c)Nb atoms and (d)Zr atoms distribution.

Since interesting physical properties are noticed in very thin MoS_2 layers, we next examined the growth of thin MoS_2 layers. To control the thickness of MoS_2, source solutions with concentrations of 0.05000, 0.02500, 0.01250 and 0.00625 mol/kg were prepared. These were spin-coated on NZO substrates just once and annealed at 1000 °C. Figure 4-15(a) shows the Raman spectra for the MoS_2 films fabricated by source solutions with various concentrations. Two Raman peaks, E_{2g} and A_{1g}, are observed in the Raman spectra for all films. Note that the peak position difference becomes smaller for the MoS_2 fabricated by the source solution with a lower concentration. The peak position difference, which is a good trace for the thickness estimation, is plotted in figure 4-15(b). The peak difference of the MoS_2 film fabricated by the 0.05 mol/kg solution corresponds to a thickness of over five layers. On the other hand, a thickness of three layers was estimated for the film grown by the 0.0125 mol/kg solution. When the source solution with a concentration of 0.00625 mol/kg was used, the thickness of the film is further decreased to two mono-layers, although the Raman peak intensity becomes small.

Finally, the Hall mobility of MoS_2 film grown on the NZO was measured using the Van der Pauw method. The Cr/AgAu metal was deposited at four edges of the sample to form the ohmic contacts. The solution processed MoS_2 film on high-k oxide film, fabricated with an annealing temperature of 1000 °C showed a sheet resistance of 400 ~ 600 ohm/sq with a Hall mobility of ~ 25 cm^2/Vs. This value is lower than that of the MoS_2 fabricated by CVD, which is 50~100 cm^2/Vs. However, considering the small grain size it is reasonably good. In addition, we would like to point out that the conventional transfer process degrades the carrier mobility even for the films exfoliated from a single crystal. Hence, although the electrical characterization is still in the preliminary stage, the Hall mobility of 25 cm^2/Vs can

be considered as a promising value for the MoS_2 films prepared by the chemical solution process.

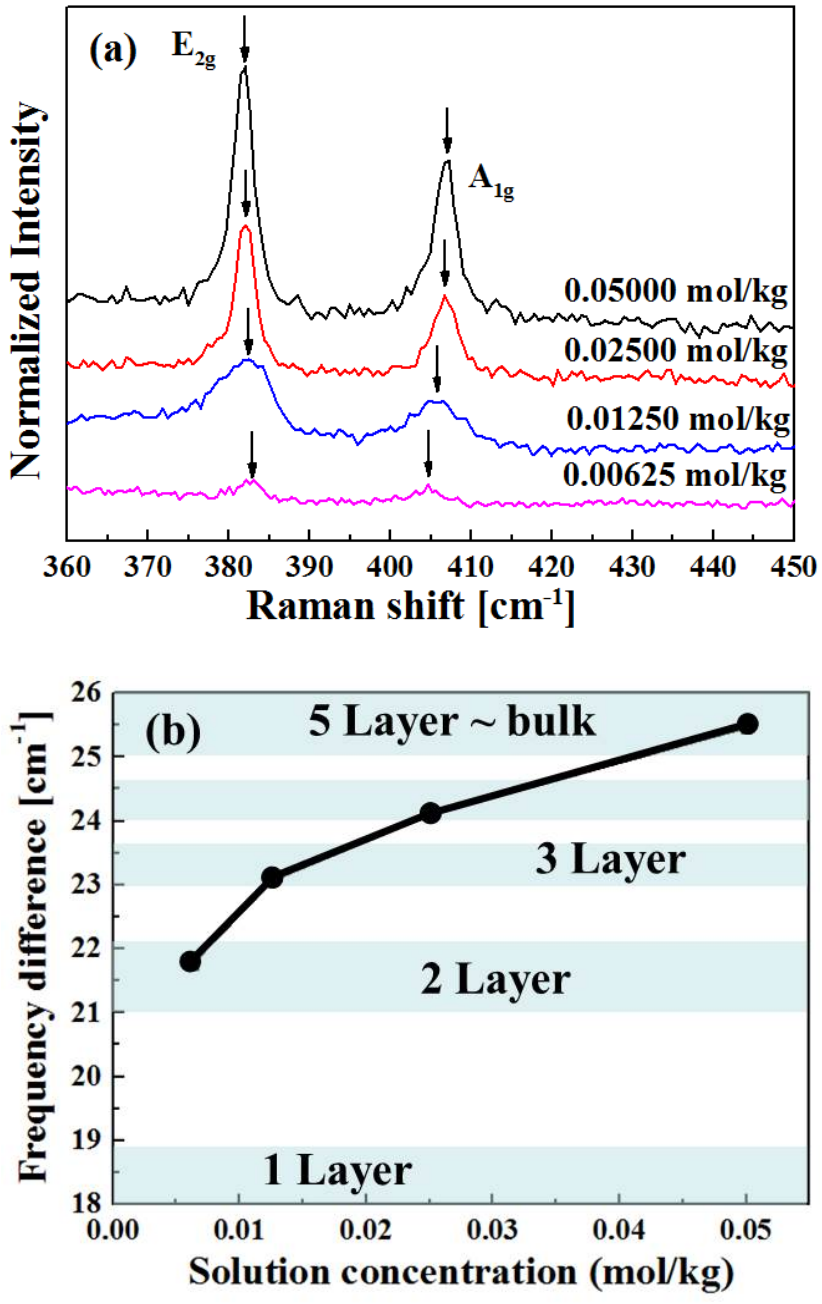

Figure 4-15. (a) Raman spectra of MoS_2 fabricated by source solutions with various concentrations. (b) Frequency difference between the peak of the E_{2g} and A_{1g} mode as a function of the concentration of the source solution.

4-4 Summary

MoS_2 films were successfully deposited by the chemical solution process on high-k oxide film. The oxide film which has relatively large γ- and small γ+ of surface energy, shows good coating property for an $(NH_4)_2MoS_4$ source solution dissolved in NMP. The two-step annealing process was introduced for solution synthesis of MoS_2. It is concluded that the H_2 introduction is needed initially to avoid oxidation and that proper sulfur atmosphere and high temperature annealing is also needed during second step to obtain high quality MoS_2 film. Using XRD and Raman scattering it is clear that high temperature annealing of 1000 °C enhanced the growth of MoS_2. The growth of the layered MoS_2 was clearly observed on the curved surface of high-k oxide film by TEM. In addition, it is also confirmed by TEM that high temperature annealing enhanced the growth of the MoS_2 layers. The thickness of MoS_2 could be controlled by concentration of the source solutions and the two layer MoS_2 film was obtained when a solution with a concentration of 0.00625 mol/kg was used. The measured Hall mobility for the MoS_2 film annealed at 1000 °C was approximately 25 cm^2/Vs.

References

[1]K. Novoselov, K. S. Geim, A. K. Morozov, “Electric field effect in atomically thin carbon films”, S. V. Jiang, D. Zhang, Y. Dubonos, S.V. Grigorieva, I. V. Firsove, Science, vol.305, pp.666, 2004.

[2]K. Novoselov, “Graphene : Mind the gap”, Nature Material, vol.6, pp.720, 2007.

[3]A. Splendiani, L. Sun, Y. Zhang, T. Li, J. Kim, C. Chim, G. Galli and F. Wang, “Emerging Photoluminescence in Monolayer MoS_2”, Nano letter, vol.10, pp.1271, 2010.

[4]K. Mak, C. Lee, J. Hone, J. Shan and T. Heinz, “Atomically Thin MoS_2: A New Direct-Gap Semiconductor”, Physics Review Letter, vol.105, pp.136805, 2010.

[5]N. Radisavlijevic, A. Radenovic, J. Brivio, B. Giacometti, A. Kis, “Single-layer MoS_2 transistors”, Nature nanotechnology, vol.6, pp.147, 2011.

[6]D. Xiao, G. B. Liu, W. Feng, X. Xu and W. Yao, “Coupled Spin and Valley Physics in Monolayers of MoS_2 and Other Group-VI Dichalcogenides”, Physics Review Letter, vol.108, pp.196802, 2012.

[7] Chun Wei Lee, Cheng-Hui Weng, Li WeiYuan Chen, Mary B. Chan-Park, Chuen-Horng Tsai, Keh-Chyang Leou, C. H. Patrick Poa, Junling Wang, Lain-Jong Li, “Toward High-Performance Solution-Processed Carbon Nanotube Network Transistors by Removing Nanotube Bundles”, Journal of Physics Chemical C, vol.112, pp.12089, 2008.

[8]N. Coleman, M. Lotya, A. O. Neill, S. Bergin, P. King, U. Khan, K. Young, A. Gaucher, S. De and R. Smith, “Two-Dimensional Nanosheets Produced by Liquid Exfoliation of Layered Materials”, Science, vol.331, pp.568, 2011.

[9] Z. Y. Zeng, Z. Y. Yin, X. Huang, H. Li, Q. Y. He, G. Lu, F. Boey and H. Zhang, “Single-Layer Semiconducting Nanosheets: High-Yield Preparation and Device Fabrication”, Angewandte Chemie, vol.50, pp.11093, 2011.

[10] Y. Yu, C. Li, Y. Liu, L. Su, Y. Zhang and L. Cao, “Controlled Scalable Synthesis of Uniform, High-Quality Monolayer and Few-layer MoS_2 Films”, Scientific Report 3, article number 1866, 2013.

[11] Y. Peng, Z. Meng, C. Zhong, J. Lu, W. Yu, Y. Jia and Y. Qian, “Hydrothermal Synthesis and Characterization of Single-Molecular-Layer MoS_2 and $MoSe_2$”, Chemical Letter, vol.8, pp.772, 2001.

[12] Q. Li, J. T. Newberg, J. C. Walter, H.C. Hemminger and R.M. Penner, “Polycrystalline Molybdenum Disulfide ($2H{-}MoS_2$) Nano- and Microribbons by Electrochemical/Chemical Synthesis”, Nano Letter, vol.4, pp.277, 2004.

[13] Y. C. Lim, W. Zhang, J. K. Huang, K. Liu, Y. H Lee, C. T Liang, C. W. Chu and L. J. Li, "Wafer-scale MoS_2 thin layers prepared by MoO_3 sulfurization", Nanoscale, vol.4, pp.6637, 2012.

[14] Y. Lee, J. Lee, H. Bark, I. K. Oh, G.H. Ryu, Z. Lee, H. Kim, J. H. Cho, J. H. Ahn and C. Lee, "Synthesis of wafer-scale uniform molybdenum disulfide films with control over the layer number using a gas phase sulfur precursor", Nanoscale, vol.6, pp.2821, 2014.

[15] K. S. Vobolselov, D. Jiang, F. Schedin, T. J. Booth, V. V. Khotkevich, S. V. Morozov and A. K. Geim. "Two-dimensional atomic crystals", Proceedings of the National Academy of Sciences of the United States of America, vol.102, pp.10451, 2005.

[16] J. H. Yang, Y. H. Gu, E. H. Lee, H. S. Lee, S. H. Park, M. H. Cho, Y. H. Kim and H. S. Kim, "Wafer-scale synthesis of thickness-controllable MoS_2 films via solution-processing using a dimethylformamide/n-butylamine/2-aminoethanol solvent system", Nanoscale, vol.7, pp.9311, 2015.

[17] J. Putz and M. A. Aegerter, "MoS_x Thin Films by Thermolysis of a Single-Source Precursor", Journal of Sol-Gel Science and Technology, vol.19, pp.821, 2000.

[18] Keng-Ku Liu, Wenjing Zhang, Yi-Hsien Lee, Yu-Chuan Lin, Mu-Tung Chang, Ching-Yuan Su, Chia-Seng Chang, Hai Li, Yumeng Shi, Hua Zhang, Chao-Sung Lai, Lain-Jong Li, "Growth of Large-Area and Highly Crystalline MoS_2 Thin Layers on Insulating Substrates", Nano Letters, vol.12, pp.1538, 2012.

[19] A. O'Neill, U. Khan, and J. N Coleman, "Preparation of High Concentration Dispersions of Exfoliated MoS_2 with Increased Flake Size", Chemistry of Materials, vol.24, pp.2414, 2012.

[20] C. Z. Zhao, M. Werner, S. Taylor, P. R. Chalker, A. C. Jones. Chun Zhao, "Dielectric Relaxation of La-Doped Zirconia Caused by Annealing Ambient", Nonoscale Research Letter, vol.6, pp.48, 2011.

[21] S. V. Ushakov, A. Navrotsky, Y. Yang, S. Stemmer, K. Kukli, M. Ritala, M. A. Leskela , P. Fejes, A. Demkov, C. Wang, B. Y. Nguyen, D. Triyoso and P. Tobin, "Crystallization in Hafnia- and Zirconia-based Systems", Physica Status Solidi (b), vol.241, pp.2268, 2004.

[22] J.N. Kim, K. Haga, E. Tokumitsu, "Investigation of Nb-Zr-O thin film using sol-gel coating", in 2016 asia-pacific workshop on fundamentals and applications of advanced semiconductor devices (AWAD2016), Hakodate, Japan, 2016, B3-3.

[23] H.W Wang, P Skeldon, G.E Thompson and G.C Wood, "Synthesis and characterization of molybdenum disulphide formed from ammonium tetrathiomolybdate", Journal of materials science, vol.32, pp.497, 1997.

[24] J. Putz and M. A. Aegerter, "Liquid Film Deposition of Chalcogenide Thin Films", Journal of Sol-Gel Science and Technology, vol.26, pp.807, 2003.

[25] P. G. De Gennes, “Wetting: statics and dynamics”, Reviews of Modern Physics, vol.57, pp.827, 1985.

[26] J. L. Brito, M. Ilija, P. Hernfindez, “Thermal and reductive decomposition of ammonium thiomolybdates”, Thermochemica Acta, vol.256, pp.325, 1995.

[27] David Tuschel, “Resonance Raman and Photoluminescence Spectroscopy and Imaging of Few-Layer MoS_2”, Spectroscopy, vol.30, pp.14, 2015.

[28] T. Ohasi, K. Suda, S. Ichihara, N. Sawamoto, S. Yamaguchi, K. Matsuura, K. Kakushima, N. Sugii, A, Nishiyama, Y. Kataoka, Kenji Natori, Kanzyo Tsutsui, H. Iwai, A. Ugura and Hitoshi Wakabayashi, “Multi-layered MoS_2 film formed by high-temperature sputtering for enhancement-mode nMOSFETs”, Japan Journal of Applied Physics, vol.54, pp.04DN08, 2015.

5. Characterization of TFTs using NZO as gate dielectric and MoS_2 as semiconductor

5-1 Introduction

Recently, the exfoliated single-layer (SL) MoS_2 have attracting attention owing to its notable electrical and optical properties. The bulk MoS_2 is usually n-type semiconductor with an indirect bandgap (~1.3 eV) and carrier mobility of the 50–200 cm^2/Vs at room temperature but when the number layer is down to single, it shows a direct bandgap of ~1.8 eV. The transistor using a MoS_2, shows high on/off current ratios (~10^8) and low sub threshold swing (74 mV/decade)[1-3]. The calculated intrinsic (optical phonon limited) carrier mobility at room temperature in single layer MoS_2 is about 410 cm^2/Vs. Actually, A. Nourbakhsh et al [20] reported on MoS_2 transistors using ALD grown 10 nm HfO_2 films as a back gate. M. S. Fuhrer et al showed the channel mobility of single layer MoS_2 transistor is 5 cm^2/Vs [4]. In this time, many researchers have focused on SL MoS_2 because of the direct band gap and high mobility expectation. This situation resembles with the initial situation of silicon and GaAs. Since GaAs shows the larger band gap (1.43 eV), higher electron mobility than Si, research on GaAs and related III-V compound semiconductors ws very active in 1980`s. Like this, many researches are now focused on single-layer MoS_2 and the multilayer MoS_2 have not been extensively studied for use in electronics. Recently, S. Kim et al., [5] reported the channel mobility over 100 cm^2/Vs with multilayer (ML) MoS_2 transistors in 2012. It shows the possibility of ML MoS_2 and becomes a milestone of research using ML MoS_2 for

electronics. As shown in chapter 4, the solution processed MoS_2 tend to be multilayer in our work.

Until now, the SiO_2 have been used for gate dielectric film because exfoliated MoS_2 film can be easily detected using optical microscope on a SiO_2 layer on silicon, due to optical interference. However, it restricted the device performance due to low gate dielectric constant. Therefore, in our work, we have fabricated the TFT which the ML MoS_2 is directly deposited on NZO (high-k) gate dielectric for the first time.

5-2 Fabrication procedure

Fabrication process flow for the thin film transistor using the Nb doped ZrO_2 and MoS_2 is shown in figure 5-1. First, the Nb 30% doped ZrO_2 (NZO-30) film as gate dielectric film was spin-coated on highly doped silicon substrate which was cleaned by acetone, isopropanol ethanol and deionized water. The NZO-30 film was annealed at 1000 °C for 5 min in air atmosphere to prevent undesired reaction with MoS_2 then, 0.05 mol/kg MoS_2 precursor solution was spin-coated on NZO-30 film to make metal insulator semiconductor (MIS) structure. This film was annealed by two step annealing process described in chapter 4.

The source and drain electrodes were formed by the lift-off technique. To make fine patterns, bi-layer photoresist (LOL 2000 and TSMR 8900 positive photoresist (PR)) process was applied. The LOL 2000 PR was spin-coated at 3000 rpm for 25 seconds on the sample then, it was dried at 180 °C for 3 min on a hot-plate. The TSMR 8900 was spin-coated on dried LOL 2000 at 4000 rpm for 25 seconds, and then, it also dried at 110 °C for 90 seconds on a hot plate. The bi-PR layers were exposed by ultraviolet (UV) through a Cr patterned glass mask at 27.5 mW for 8.4 seconds. The exposed PR was developed by NMD-W solution

for 1 min. The developed film was rinsed in water for 1 min. The patterned film was baked again at 80 °C for 30 seconds on hot-plate.

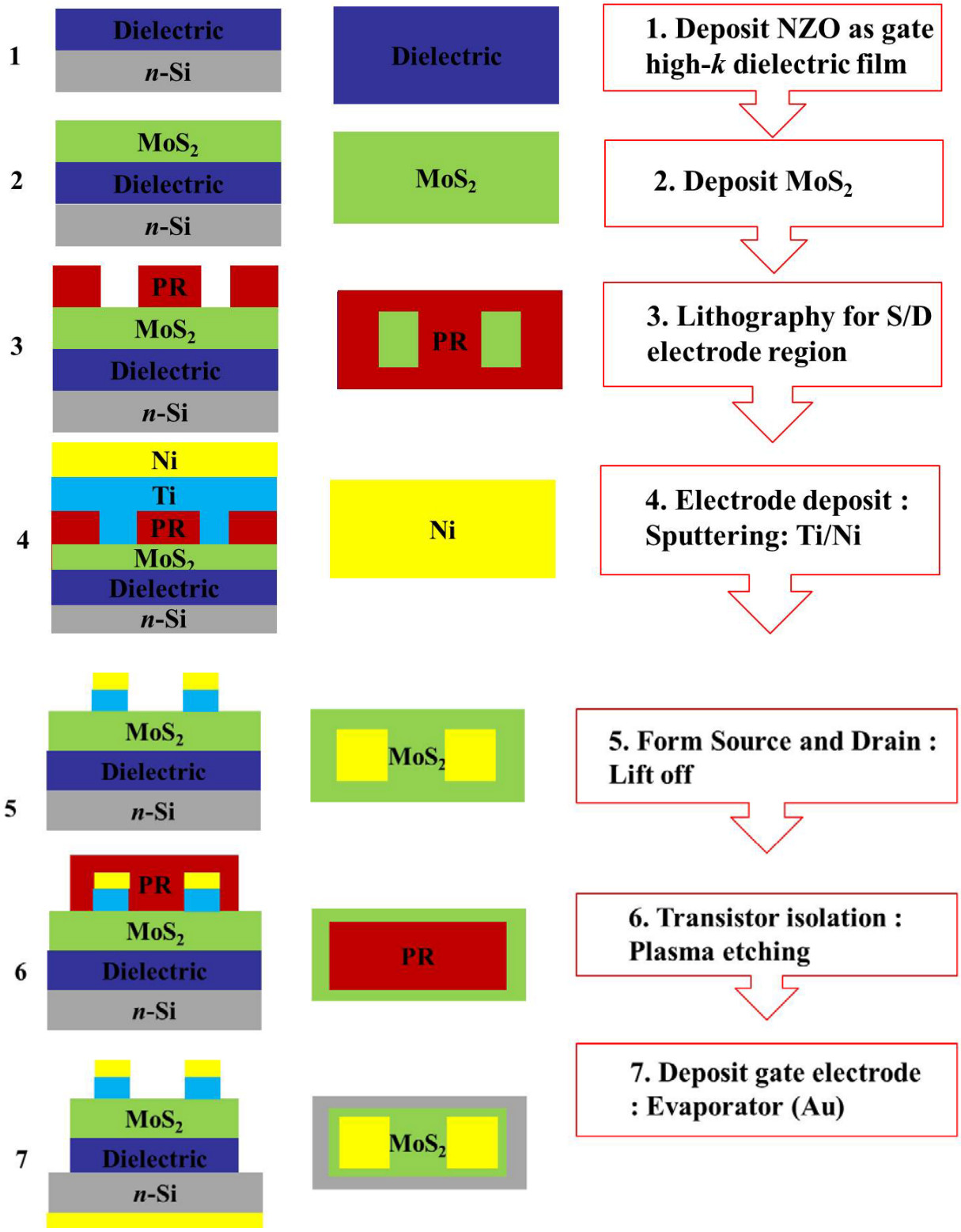

Figure 5-1. Process diagram for TFT with MoS_2 and NZO film.

Figure 5-2 shows band line-up of multi-layer MoS_2 and several kinds of metals. The multi-layer MoS_2 is an n-type semiconductor, so the Fermi level is located 0.2 eV under the conduction band. Fermi level of Ti is most close to the Fermi level of MoS_2, but Ti is easily oxidized. Hence, Ti/Ni double layer was used for ohmic contact to protect Ti against oxidation. These metals were deposited on MoS_2 by the RF sputtering. Ti was sputtered at 75 W for 8 min with Ar gas of 5 sccm, and Ni was sputtered at 75 W for 20 min with Ar gas of 3.8 sccm. To form the source and drain regions by the lift-off process, the 1165 solution was used to eliminate the bi-PR layer. The sputtered sample was inserted into the 1165 solution at 80 °C for 10 min.

To isolate the TFT, a PR pattern which covered source, drain and channel regions, was formed by the lithography method. The OMR-85 negative PR was spin-coated on the sample at 2000 rpm for 25 seconds. The coated film was exposed at 27.5 mW for 2.4 seconds. The exposed film was developed by the NMD-W developer for 1 min and then, it was rinsed by DI water. The developed film was dried at 110 °C for 1 min to make hard PR film to endure an etching process. For device isolation, unnecessary MoS_2/NZO regions were etched by the O_2 plasma etching with 75 W in O_2 atmosphere for 2 min. After the etching process, the sample was inserted in acetone to resolve the OMR-85 PR, and then rinsed in the DI water.

Finally, to form the back gate electrode, the gold was evaporated on bottom of the silicon substrate.

The gate voltage-drain current (V_G-I_D) and drain voltage-drain current (V_D-I_D) characteristics were measured by Agilent 4155C semiconductor parameter analyser and a probe system in air atmosphere.

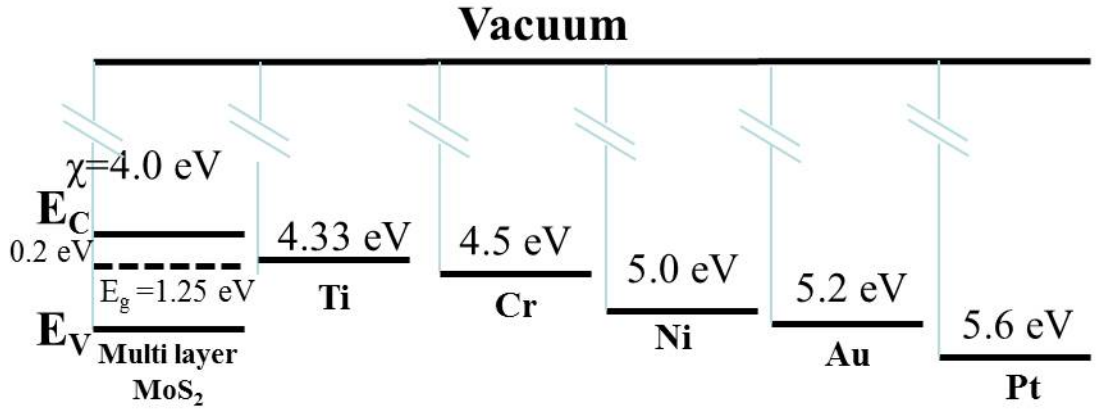

Figure 5-2. Energy band structure between multilayer MoS_2 semiconductor and Ti, Cr, Ni, Au and Pt metal.

5-3 Results and discussion

The thin film transistors using solution processed MoS_2 as semiconductor and Nb 30% doped ZrO_2 as gate insulator were fabricated with channel length of 10 μm and width 50 μm, respectively as shown in figure 5-3. The 0.05 mol/kg MoS_2 solution was used so the width of Raman peak in figure 5-3 was 26 cm^{-1} (over five layers).

The MoS_2 absorbs the H_2O through its edge site [6], which produces trapping states to reduce the carriers in MoS_2 [7]. Figure 5-4 shows the characteristic of gate-voltage (V_G) and drain current (I_D) for the transistor before vacuum and thermal treatment to eliminate the water in MoS_2. Transistor behavior is observed. However, the on/off ratio was $1.9x10^2$. Note that on drain current at a gate voltage of 7 V is low. In addition, a clockwise hysteresis is observed. To improve the device performance, I carried out the vacuum and thermal treatment. The sample was preserved at 150 °C in a vacuum, purged by a rotary pump, for

one day. As shown in figure 5-5, the electrical properties of the MoS_2 TFT can be improved by this treatment. The vacuum and thermal treated transistor showed a typical n-type transistor behavior. The on/off ratio was enhanced to $1.1x10^5$ due to higher on drain current at a gate voltage of 7 V.

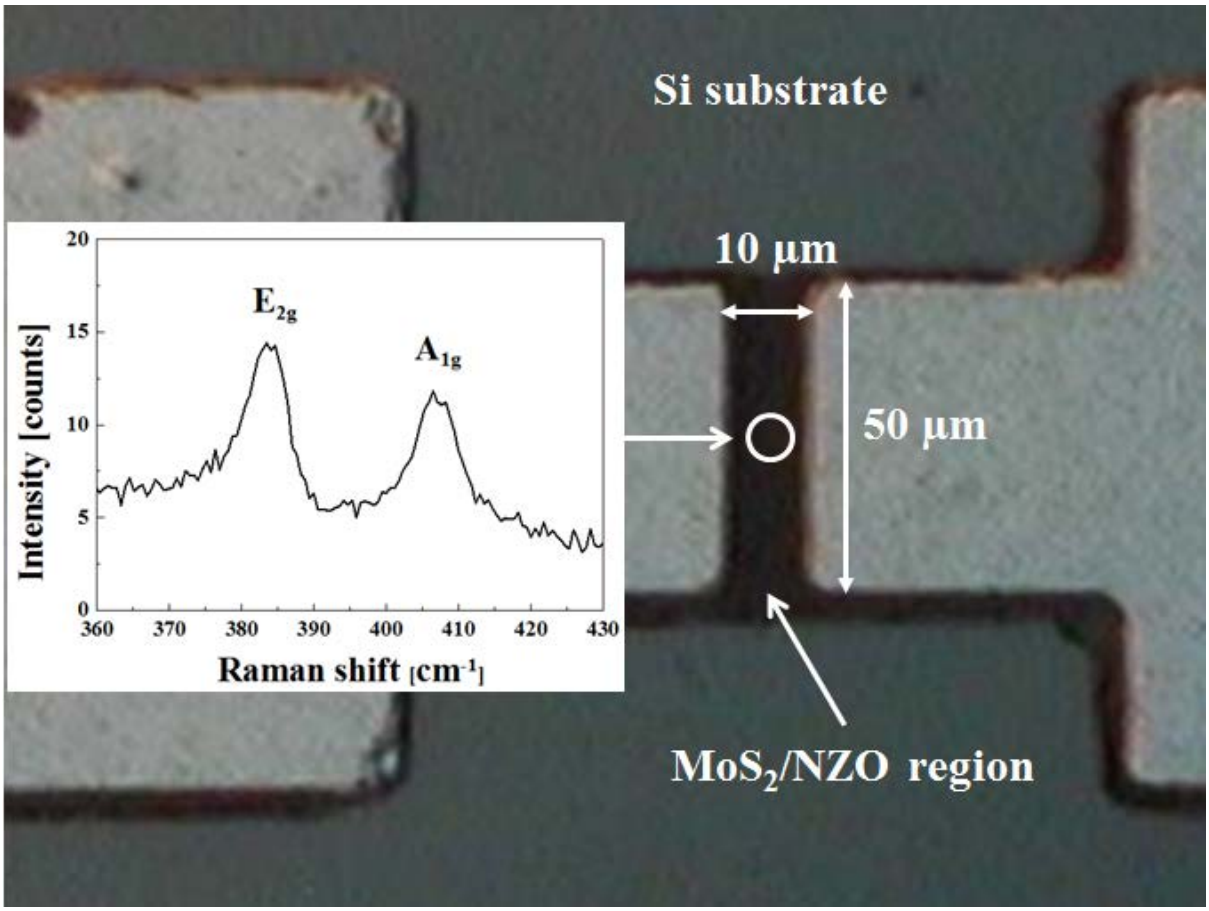

Figure 5-3. Plan view of metal pad for multilayer MoS_2 transistor and its Raman spectra.

The field effect mobility (μ_{linear}) can be derived from drain current ($I_{D,linear}$) in linear region from eq.5-1.

$$I_{D,linear} = \frac{W}{L}\mu_{linear}\left\{C_{ox}(V_G - V_D)V_D - \frac{V_D^2}{2}\right\} \qquad \text{(eq.5-1)}$$

where channel width (W) and length (L), capacitance of gate oxide (C_{ox}), gate-source voltage (V_G) and drain-source voltage (V_D).

When this equation was differentiated at both sides, it was changed to eq.5-2 to calculate field effect mobility.

$$\mu_{linear} = \frac{dI_D}{dV_G}\frac{L}{W}\frac{1}{C_{ox}}\frac{1}{V_D} \qquad \text{(eq.5-2)}$$

In my experiment, the calculated mobility at linear region was from 0.86 cm^2/Vs.

The mobility at saturation region ($\mu_{saturate}$) can be calculated from saturation drain current ($I_{D,saturate}$, eq.5-3). It is also transformed to eq.5-4 by differentiation. The mobility at saturation region was 0.22 cm^2/Vs with V_{th}=1.56V.

$$I_{D,saturate} = \frac{1}{2}\frac{W}{L}\mu_{saturate}C_{ox}(V_G - V_{th})^2 \qquad \text{(eq.5-3)}$$

$$\mu_{saturate} = \frac{dI_D}{dV_G}\frac{L}{W}\frac{1}{C_{ox}}\frac{1}{V_G - V_{th}} \qquad \text{(eq.5-4)}$$

The mobility of exfoliated MoS_2 film shows 500 cm^2/Vs [2] and the CVD one for monolayer shows about 12 cm^2/Vs at room temperature [8]. However, to fabricate TFTs, the MoS_2 film was transferred to another substrate in many reports, and after the transfer process, the channel mobility of the fabricated TFTs was not so high. This is probably because the degradation or damage induced during the transfer process. Moreover, TFTs with multilayer MoS_2 deposited by CVD, shows the mobility of 1.8 cm^2/Vs [9] because of grain boundaries, points defects and the interfacial states between the MoS_2 layer and insulator surface. The

solution processed MoS_2 film also shows relatively lower mobility (< 1 cm^2/Vs) because of same reasons abovementioned.

An interesting thing is that even though the exfoliated MoS_2 or high-quality CVD MoS_2 was used for device fabrication, the observed channel mobility of the TFTs was similar to that of the device with the MoS_2 film made by the solution process. In this work, MoS_2 was directly deposited on high-k gate insulator, without the transfer process and higher channel mobility is expected by improving the surface roughness of the high-k gate insulator.

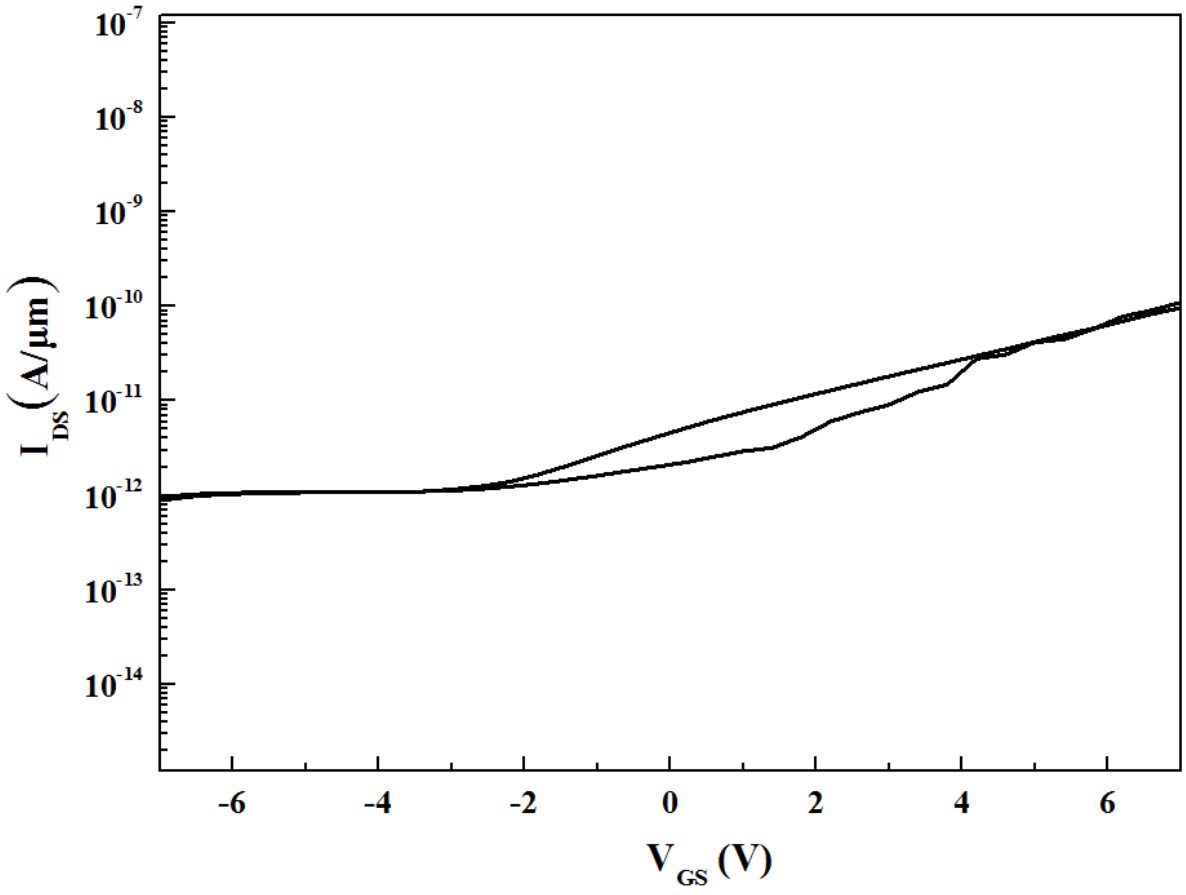

Figure 5-4. The characteristic of gate-voltage and drain current for the transistor before vacuum and thermal treatment.

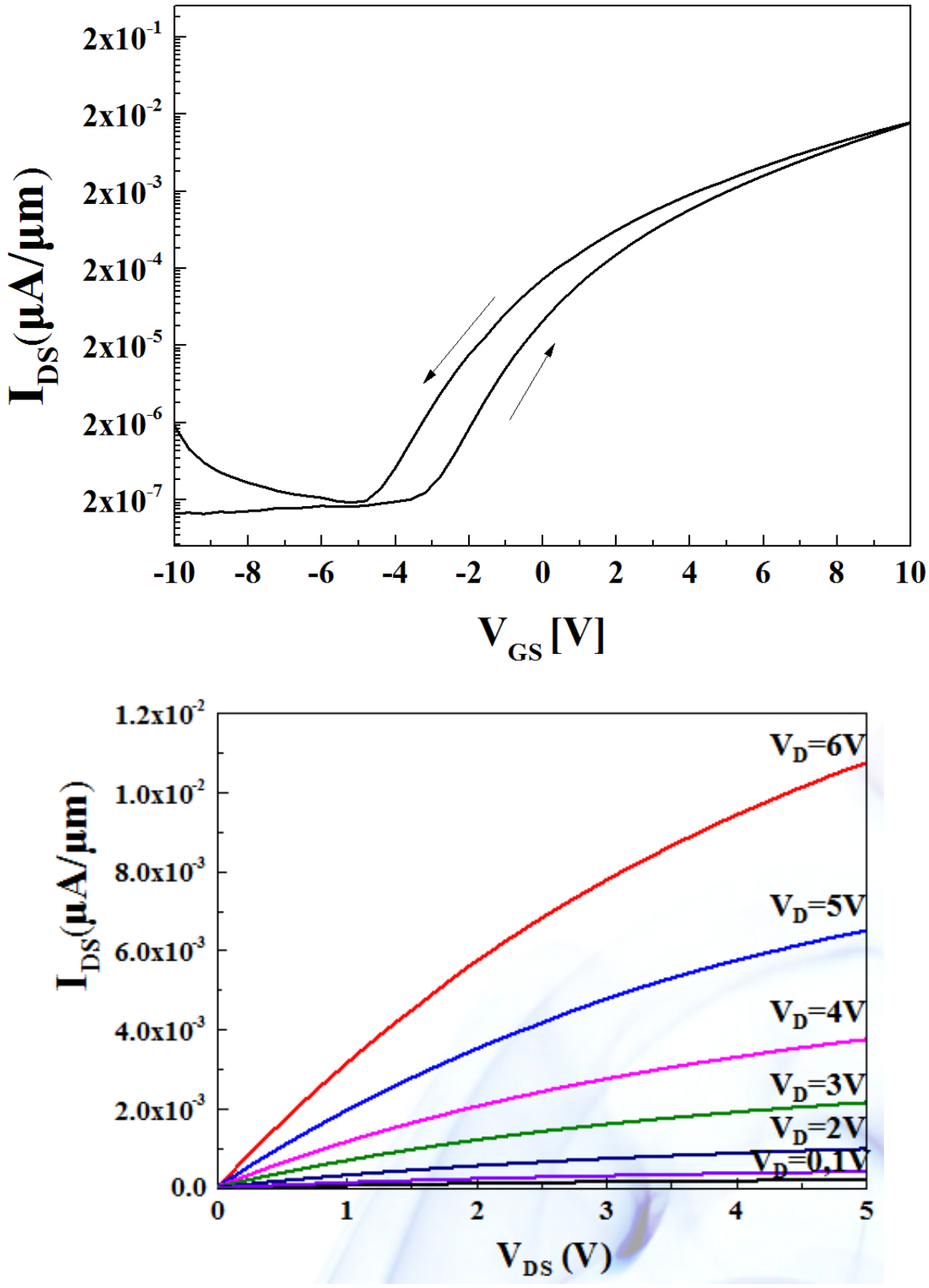

Figure 5-5. After vacuum and thermal treatment, the characteristic of (a)gate-voltage and drain current and (b) drain-voltage and drain current.

5-4 Summary

In this chapter, thin film transistors which used the solution processed MoS_2 as a semiconductor and Nb 30% doped ZrO_2 as a high-k gate dielectric film, were fabricated and characterized. The MoS_2 was deposited on NZO gate insulator directly to avoid the damage caused by the transfer process. When a solution density of 0.05 mol/kg for MoS_2 was used to fabricate thin channel layer, n-channel transistor operation was observed. However, the as-fabricated device showed low on current, resulting in low on/off ratio. To improve the device performance, the device was annealed in vacuum at 150 ºC for one day to eliminate the absorbed H_2O at MoS_2 grains before the measurements. After the treatment, the transistor showed normal transistor characteristics with an on/off ratio of $1.1x10^5$ and a field effect mobility of 0.86 cm^2/Vs. This value is almost the same as that reported for TFT with transferred or CVD multilayer MoS_2.

References

[1] B. Radisavljevic, A. Radenovic, J. Brivio, V. Giacometti, and A. Kis, "Single-layer MoS_2 transistors", Nature Nanotechnology, vol. 6, no. 3, pp. 147, 2011.

[2] S. Das, H.-Y. Chen, A. V. Penumatcha, and J. Appenzeller, "High performance multilayer MoS_2 transistors with scandium contacts", Nano Letter, vol.13, pp. 100, 2013.

[3] H. Liu and P. D. Ye, "MoS_2 dual-gate MOSFET with atomic-layer deposited Al_2O_3 as top-gate dielectric", IEEE Electron Device Letter, vol. 33, pp. 546, 2012.

[4] N. Radisavlijevic, A. Radenovic, J. Brivio, B. Giacometti, A. Kis, "Single-layer MoS_2 transistors", Nature nanotechnology, vol.6, pp.147, 2011.

[5] Sunkook Kim, Aniruddha Konar, Wan-Sik Hwang, Jong Hak Lee, Jiyoul Lee, JaehyunYang, Changhoon Jung, Hyoungsub Kim, Ji-Beom Yoo, Jae-Young Choi, Yong Wan Jin, Sang Yoon Lee, Debdeep Jena, Woong Choi and Kinam Kim, "High-mobility and low-power thin-film transistors based on multilayer MoS_2 crystals", Nature Communications, vol.3, article number 1101, 2012.

[6] Kulbir Kaur Ghuman, Shwetank Yadav, and Chandra Veer Singh, "Adsorption and Dissociation of H_2O on Monolayered MoS_2 Edges: Energetics and Mechanism from *ab* Initio Simulations", Journal of Physical Chemistry C, vol.119, pp.6518, 2015.

[7] Ming-Wei Lin, Ivan I Kravchenko, Jason Fowlkes, Xufan Li, Alexander A Puretzky, Christopher M Rouleau, David B Geohegan and Kai Xiao, "Thickness-dependent charge transport in few-layer MoS_2 field-effect transistors", Nanotechnology, vol.27, pp.165203, 2016.

[8] Hong, J. H.; Hu, Z. X.; Probert, M.; Li, K.; Lv, D. H.; Yang, X. N.; Gu, L.; Mao, N. N.; Feng, Q. L.; Xie, L. M., "Exploring Atomic Defects in Molybdenum Disulphide Monolayers", Nature Communication, vol.6, pp. 6293, 2015.

[9] Tae-Young Kim, Matin Amani, Geun Ho Ahn, Younggul Song, Ali Javey, Seungjun Chung and Takhee Lee, "Contacts Electrical Properties of Synthesized Large-Area MoS_2 Field-Effect Transistors Fabricated with Inkjet-Printed", American Chemical Society Nano, vol.10, pp.2819, 2016.

6. Conclusions

6-1. Summary and conclusions of this research

Unlike the recent researches for the MoS_2 which used exfoliation or CVD process on SiO_2 substrate or sapphire, this work has focused on the study of solution process based MoS_2 which was directly deposited on high-k oxide film for thin film transistors for the first time. It is shown that the solution processed MoS_2 could be deposited on large area substrate and even on the substrate with rough surface. Moreover, the thickness of MoS_2 was controlled by the solution concentration and the thin MoS_2 film up to two layers can be fabricated. Hereinafter, the summaries for each chapter will be given so that a brief overview for this study will be valid.

In chapter 1, as an introduction of this research, it is shown 2D materials are promising for next generation semiconductor devices. Although graphene is attracted much attention because of its high mobility, it is difficult to apply graphene to TFT applications since its bandgap is zero. On the other hand, since MoS_2 has appropriate bandgap (1.2 ~ 1.8 eV) and high mobility (~500cm^2/Vs), MoS_2 is one of the most promising 2D materials for future electronics. So far, to fabricate the MoS_2 thin film, the mechanical or chemical exfoliated method, and the CVD technique have been used usually and there is only a few researches about solution process for MoS_2. Moreover, in the most of previous researches, the MoS_2 film was deposited on SiO_2 and the MoS_2 has to be transferred to other substrate because the dielectric constant of SiO_2 is small. On the other hand, in this research, the MoS2 films were fabricated high-k gate dielectric films directly by the newly developed solution process. The

objective of this research is to develop chemical solution process for MoS_2 thin films and to apply the solution-derived MoS_2 to thin film transistors.

In chapter 2, experimental and analysis methods used in this study were explained. To characterize of NZO and MoS_2 film, the GI-XRD, Raman spectrometer, XPS, AFM, TEM, surface energy measurements and TG/DTA measurement were conducted.

In chapter 3, for the substrate of MoS_2 and the gate insulator for MoS_2 TFTs, the ZrO_2 system was selected because of high thermal stability. Although there are many kinds of dopants such as Y^{3+}, Ce^{3+} to stabilize the tetragonal of ZrO_2, Nb was used as a dopant in this work and the morphological and electrical properties of NZO film were investigated. It is concluded that the optimized composition and annealing condition of NZO is the following: Nb 30% doping density and 800 ^oC annealing temperature in air atmosphere. It is shown the Nb atoms did not diffuse into silicon substrate after the annealing. The Nb doping influences stabilization of the tetragonal phase of ZrO_2 as well as absorption of water and oxygen from the air. Especially, the Nb doped ZrO_2 showed larger dielectric constant (ε=40) than pure ZrO_2 (ε=20) annealed under the same condition. Therefore, Nb could be considered as an available dopant for ZrO_2.

In chapter 4, solution process for MoS_2 developed in this study is mentioned. NMP solvent and $(NH_4)_2MoS_4$ precursor was chosen because the solution made of NMP and $(NH_4)_2MoS_4$ shows the most stable and uniform film can be obtained by the spin-coating on NZO film. Although several materials such as HfO_2, BLT, PZT and so on, were examined As high-k oxide substrate, ZrO_2 system was selected because the other materials was changed to undesired state after high annealing temperature (1000 ºC) with sulfur atmosphere. In addition, relationship between coating property and surface energy of substrate was discussed.

The optimized process for the spin-coated MoS_2 films on NZO was investigated by XRD, XPS, Raman spectrometer. To obtain high quality MoS_2 film, a two-step annealing process was applied. The spin-coated MoS_2 film was annealed at 450 ºC in H_2/Ar (5/95) atmosphere then, the film was annealed again at 1000 ºC in Ar atmosphere with sulfur powder. The well-defined MoS_2 film was confirmed by TEM and Raman spectroscopy. Although Nb could be affected as p-type dopant for MoS_2, no significant diffusion of Nb from NZO film to MoS_2 film was observed. One of the interesting findings is that the MoS_2 grew following the curved plane of the rough NZO surface. The thickness of MoS_2 could be controlled by concentration of the source solutions and the two layer MoS_2 film was obtained when a solution with a concentration of 0.00625 mol/kg was used. The measured Hall mobility for the MoS_2 film annealed at 1000 °C was approximately 25 cm^2/Vs.

In chapter 5, MoS_2 channel TFTs using the NZO as a high-k gate dielectric have been fabricated and characterized. MoS_2 film was fabricated by the chemical solution process on the NZO gate insulator directly. It is shown that the TFT which was treated by vacuum and thermal annealing, showed a typical n-type semiconductor behaviour with an on/off ratio of $1.1x10^5$ with V_G=±7V and V_D=1V. The calculated mobility at linear region was from 0.86 cm^2/Vs and the mobility at saturation region was 0.16 cm^2/Vs with V_{th}=1.56 V.

6-2. Future Prospects of this study

In this study, the MoS_2 was deposited on high-k oxide film directly by the chemical solution process developed in this study. This work shows possibility that the solution processed MoS_2 could be applied to electronics applications. However, there are several points which have to be investigated.

First, it is interesting to find other high-k materials which endure the high temperature annealing process without serious reaction with sulfur. In addition, high-k materials fabricated by sputtering or ALD should be examined. In this study, the NZO film was deposited by the solution process. If the NZO film is deposited by the sputtering or ALD which shows flat surface, the roughness of NZO could be improved. Since it is thought that the grain size of MoS_2 strongly depends on the roughness of substrate, small roughness is helpful to obtain high-quality MoS_2 film with large grains.

Second point is to reduce the annealing temperature for MoS_2. In this study, the high temperature annealing process (1000 ºC) was used to arrange the structure of 2H MoS_2 and to supply the sulfur atoms to MoS_2. It would be nice if high-quality MoS2 film can be fabricated at lower temperature. If the annealing temperature is recued to 500 º C, MoS_2 channel TFTs can be fabricated on glass substrates, which improve the performance of flat-panel displays significantly. The laser annealing method, and photo-assisted decomposition could be possible techniques to reduce the annealing temperature.

Third one is doping. A big advantage of solution process is the easiness to add dopant. To enhance the mobility of MoS_2 and to control the conduction type, studies of doping in the solution process are required. If we can control the conduction type along with the carrier

concentration, various kinds of components can be realized, such as p-n diode, light emitting device, CMOS logic circuits and so on.

Announcement list

Paper

1.“Fabrication of MoS_2 thin films on oxide-dielectric-covered substrates by chemical solution process”, Joonam Kim, Koichi Higashimine, Ken-ichi Haga and Eisuke Tokumitsu, Physica status solidi (b), in published.

2.“Investigation of Nb-Zr-O thin film using sol-gel coating”, Joonam Kim, Ken-ichi Haga and Eisuke Tokumitsu, Journal of semiconductor technology and science, in published.

International conference

3.“Characterization of solution processed thin film MoS_2 on oxide dielectric”, Joonam Kim, Eisuke Tokumitsu, The 5^{th} International Symposium on Organic and Inorganic Electronic Materials and Related Nanotechnologies (EM-Nano 2015), June 16~19, Niigata, Japan, poster.

4.“Fabrication of MoS_2 thin films on oxide-dielectric-covered substrates by solution process”, Joonam Kim, Eisuke Tokumitsu, Compound Semiconductor Week 2016 (CSW2016),June 26~30, Toyama, Japan, poster

5.“Investigation of Nb-Zr-O thin film using sol-gel coating”, Joonam Kim, Ken-ichi Haga, Eisuke Tokumitsu, 2016 Asia-Pacific Workshop on Fundamentals and Applications of Advanced Semiconductor Devices (AWAD2016), July4~6, Hakodate, Japan, B3-3, Oral.

Domestic conference

6.“Characterization of niobium doped ZrO_2 for gate dielectric material”, Joonam Kim, Eisuke Tokumitsu, IISc-JAIST Joint workshop on Functional Inorganic and Organic Material, March 7, 2016, Nomi, Japan. poster.

7.“Characterization of sol-gel derived Nb doped ZrO_2 thin film”, Joonam Kim, Eisuke Tokumitsu , 第63回応用物理学会春季学術講演会, March 19~22, 2016, Tokyo, Japan, poster.

8.“Chemical solution processed MoS_2 on high-k oxide film”, Joonam Kim, Koichi Higashimine, Ken-ichi Haga and Eisuke Tokumitsu, 第77回応用物理学会秋季学術講演会, September 13~16, 2016, Niigata, Japan, E13p-A37-2, Oral.

9. “Investigation of solution processed MoS_2 on high-k oxide film”, Joonam Kim, Ken-ichi Haga and Eisuke Tokumitsu, 平成28年度応用物理学会北陸・信越支部学術講演会, December 10, 2016, Toyama, Japan, not decision yet , Oral.

10. “溶液プロセスによる MoS_2の作製と薄膜トランジスタ応用に関する研究”, 金宵男羽賀健一、徳光永輔, 第64回応用物理学会春季学術講演会, March 14~17, 2017, 横浜, 日本, Oral.

Acknowledgement

First of all, I would like to express my profound gratitude to Prof. Eisuke Tokumitsu for providing such an interesting theme and his abiding guidance and encouragement during the author`s doctor course. I want to express thank again for a long time.

The author would like to express special appreciation to Associated Prof. Mikio Koyano for providing advice about Raman measurement.

The author is grateful to Prof. Masahiko Tomitori for his kind direction and fruitful discussions during conducting a minor thesis.

The author would like to thank Prof. Tatsuya Shimoda for impressive consideration and providing experimental equipment.

The author would like to express appreciation to Prof. Hiroshi Mizuta for providing graphene substrate and screening doctor thesis.

The author is grateful to Prof. Keiji Ueno (Saitama University) for screening doctor thesis.

The author would like to thank assistant Prof. Ken-ichi Haga for support Tokumitsu laboratory and useful discussion about oxide materials.

The author would like to thank Dr Jinwang Li and Dr. Daisuke Hirose and Dr. Tomoki Ariga in Shimoda laboratory and Dr. Tatsuya Muragae (XPS) and Dr. Koichi Higashimine (TEM) and Akio Miyazato (Mass measurment) in Nanotechnology Center for their technical assistance in the experiment.

The author would like to express thank Ki Kang Kim (Dokkuk University in Korea) for providing BN substrate.

Finally, I would like to express my gratitude to my family and friends for their continuous love and support. Especially, I wish to express undying love to my wife.